TU Delft

Coupling approximation levels for modeling ice flow on paleo time scales

by

Eef (E.C.H.) van Dongen

to obtain the degree of Master of Science
at the Delft University of Technology,
to be defended publicly on Monday July 3, 2017 at 14:00.

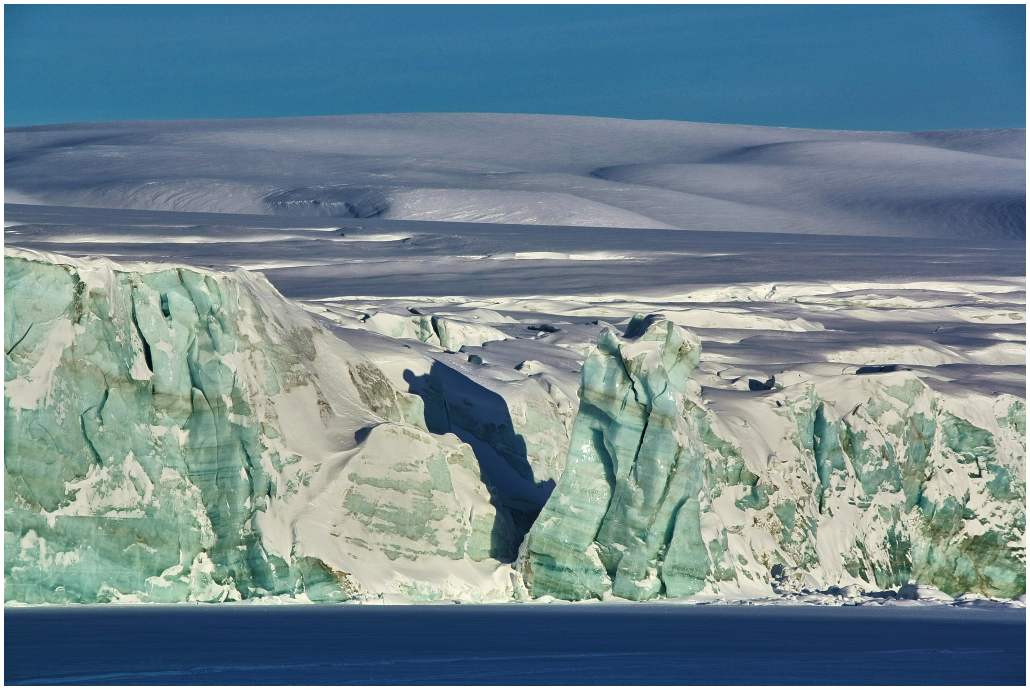

Student number:	4391578	
Programme:	MSc Applied Mathematics	
Faculty:	EEMCS	
Specialisation:	Computational Science and Engineering	
Thesis committee:	Dr. ir. M.B. Van Gijzen,	TU Delft, project supervisor
	Dr. N. Kirchner,	Stockholm University, daily supervisor
	Dr. R.S.W. Van de Wal	Utrecht University
	Prof. dr. ir. A.W. Heemink	TU Delft

An electronic version of this thesis is available at `http://repository.tudelft.nl/`.

Abstract

Ice flow, forced by gravity is governed by the Full Stokes (FS) equations, which are computationally intensive to solve due to their non-linearity. Therefore, it has been unavoidable to approximate the FS equations when modeling growth and collapse of an ice sheet-shelf system, which requires simulating many thousands of years. However, the most popular Shallow Ice Approximation (SIA) and Shallow Shelf Approximation (SSA) are only accurate in certain parts of an ice sheet, both excluding the grounding line where the ice starts floating. Using the Finite Element software Elmer/Ice, SIA and SSA are dynamically coupled to FS aiming to maintain high precision and reduce computation time. An existing coupling of SIA and FS, called ISCAL [Ahlkrona et al., 2013a], is investigated for robustness. It is shown that instabilities in the FS solution limit ISCAL's robustness.

A novel way of iteratively coupling SSA and FS has been implemented into the open source Finite Element software Elmer/Ice and applied to both 2D and 3D conceptual marine ice sheets. The SSA-FS coupling shows to be very accurate, for both diagnostic and prognostic runs (error in velocity respectively below 0.5% and 5%). Grounding line dynamics of the SSA-FS coupling are similar to the FS model under a periodical forcing in a simulation covering 3000 years. The current implementation does not yield speed up in 2D due to inefficient assembly of the matrices to be solved.

In 3D, the cpu time is reduced to two thirds of the cpu time of the FS model despite inefficient assembly. The total number of FS iterations in the SSA-FS coupling is comparable to the FS model, showing a large potential of reducing computation time since computation time of the SSA model is up to 3% of the FS model's computation time when applied to the same ice shelf ramp. In future research, the SSA-FS coupling can be combined with ISCAL, but this requires both efficient implementation of the SSA-FS coupling and improved stabilization methods for FS.

Samenvatting in Nederlands

De stroming van ijs onder invloed van zwaartekracht wordt beschreven door de Full Stokes (FS) vergelijkingen, die tijdrovend zijn om numeriek op te lossen door hun niet-lineariteit. Daarom is het onontkoombaar om de FS vergelijkingen te benaderen voor het modelleren van grote ijskappen op tijdschalen van duizenden jaren. De meest populaire benaderingen, Shallow Ice Approximation (SIA) en Shallow Shelf Approximation (SSA), zijn echter alleen nauwkeurig in bepaalde delen van een ijskap, geen van beiden in het gedeelte waar het ijs begint te drijven. In dit project worden SIA en SSA in de dynamisch gekoppeld aan FS door domein decompositie, erop gericht om hoge precisie te behouden en berekeningstijd te verlagen. Een bestaande koppeling van SIA en FS, genaamd ISCAL [Ahlkrona et al., 2013a], wordt onderzocht voor robuustheid. Het blijkt dat oscillaties in de FS-oplossing ISCAL's robuustheid limiteren.
Een nieuwe koppeling van SSA en FS is geïmplementeerd en toegepast op zowel 2D als 3D conceptuele mariene ijskappen met ijsplateaus. De SSA-FS koppeling blijkt zeer nauwkeurig te zijn, maar de huidige implementatie levert alleen in 3D tijdsbesparing op door inefficiënte implementatie. Het totale aantal FS iteraties in de SSA-FS-koppeling is echter vergelijkbaar met het FS-model, wat duidt op de mogelijkheid om berekeningstijd te verminderen. In toekomstig onderzoek kan de SSA-FS koppeling gecombineerd worden met ISCAL, maar dit vereist zowel efficiëntere implementatie van de SSA-FS koppeling en verbeterde stabilisatiemethodes voor FS.

Sammanfattning på svenska

Isens rörelse beskrivs av Full Stokes (FS) ekvationerna, som är beräkningsmässigt tunga att lösa genom sin icke-linjäritet. Därför har det varit oundvikligt att approximera FS ekvationerna för modellering av inlandsisar på geologiska tidsskalor av många tusentals år. De mest populära approximationerna Shallow Ice Approximation (SIA) och Shallow Shelf Approximation (SSA) är bara noggranna i vissa delar av inlandisarna, båda utgör en dålig approximation i regionen där isen börjar flyta. I detta projekt kopplas SIA och SSA till FS i finita element koden Elmer/Ice för att behålla hög precision och minska beräkningstiden. En befintlig koppling av SIA och FS, kallad ISCAL [Ahlkrona et al., 2013a], undersöks med avseende på stabilitet. Det visar sig att det finns instabiliteter i FS lösningen som begränsar ISCALs robusthet.
Ett nytt sätt att koppla SSA och FS har implementerats och applicerats till både 2D och 3D konceptuella marina inlandsisar. Kopplingen SSA-FS visar sig vara mycket noggrann, men den befintliga implementeringen har så pass ineffektiv assemblering av systemmatrisen att den inte sparar tid i 2D. Det totala antalet FS-iterationer i SSA-FS kopplingen är dock jämförbart med FS modellen, vilket visar en stor potential för att accelerera simuleringstiden för kopplingen. I framtiden kan SSA-FS kopplingen kombineras med ISCAL, men detta kräver både effektiv implementering av SSA-FS kopplingen och förbättrade stabiliseringsmetoder för FS.

Preface

This research project is part of a double degree, combining Applied Mathematics (AM) at TU Delft with Climate Physics (CP) at Utrecht University. Aside from the courses offered at my home universities, I took two courses in glaciology at The University Centre in Svalbard, where I encountered the complex nature of ice flow dynamics, which showed me the many challenges in glaciological modeling. Combining my two degrees in one project has been very valuable, since the mathematics courses have provided me with a solid background in solving problems relevant for climate physics. It prepared me for investigating numerical methods for modeling ice dynamics in more detail, keeping the relevance for glaciology in mind as an interpreter between mathematicians and geologists.

Duration of this project is one academic year (60ECTS), of which half of the time consists of joint work for AM and CP. Besides that, 12 ECTS are devoted solely to mathematics and 18 ECTS to CP. The interdisciplinary nature of the project is such that one could say that the whole project consists of joint work. However, in order to allow fair comparison to other degree projects at each respective program, a division according to the ECTS can be made. Testing of the ISCAL method, as described in Section 4.1 and 5.1 is part of CP. Development, implementation and the first conceptual test of the coupled SSA-FS model in both two and three dimensions, as described in Section 4.2, 5.3.1.1 and 5.3.3 are part of AM. Further testing of the SSA-FS coupling for both accuracy and efficiency, as described in Sections 5.3.1.2 - 5.3.2.2 is joint work. As such, the first research question (see Section 1.1) belongs to CP, the second to AM and the final question to both. Most of the Section 2 on ice sheet dynamics is joint, but the Marine Ice Sheet Instability (Section 2.3) is more relevant for CP, Section 3.1 and 3.2 provide the mathematical basis of solving SSA and FS using FEM.

The project is supervised by Nina Kirchner, professor of glaciology at Stockholm University, whom I want to thank for advice and support throughout the year. I really appreciate that I could always knock on your door or send an email to Svalbard, Tarfala, Gränna or wherever you were at that time. The project was in close collaboration with the Ice Sheet modeling group at the Department of Information Technology, Division of Scientific Computing of Uppsala University where results were discussed in weekly meetings, which I want to thank Per, Lina and Cheng Gong for. Also Cheng Gongs practical support with Elmer/Ice was very much appreciated. For the respective programs, the project supervisors are Martin van Gijzen (AM) and Roderik van de Wal (CP). Even though Stockholm is not around the corner, it felt like that with our regular Skype meetings which I want to thank you for. During two visits to the developers of Elmer(/Ice) at CSC-IT Espoo, Thomas Zwinger was the main advisor. Thanks to his hands-on guidance, the weeks in Finland were the most effective ones during the project. A poster presentation of the results took place at the FRISP 2017 conference. Besides that, the goal is to submit a paper on the SSA-FS coupling and its first applications to the journal Geoscientific Model Development.

Contents

1 Introduction

The world as we know it is home to two ice sheets, the Greenland Ice Sheet (GIS) and the Antarctic Ice Sheet (AIS). By definition, ice sheets cover at least 50 000 km^2 of land, smaller ice masses are called ice caps or glaciers. On a daily basis, ice sheets are influenced by temperature fluctuations in both atmosphere and ocean. However, on longer timescales, the gravity driven flow of ice becomes increasingly important as the ice spreads under its own weight. Flow transfers ice from high elevation regions where snowfall induces mass gain (*accumulation*), to regions of net mass loss at lower elevations, where ice is lost by melting and run-off (*ablation*) and ice bergs breaking off (*calving*, see Figure 1).

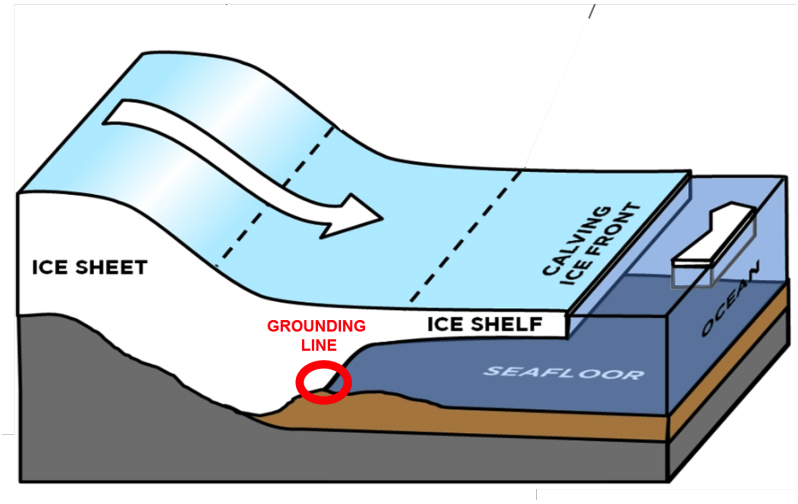

Figure 1: Sketch of a ice sheet-ice shelf system, adapted from Kirchner et al. [2011].

Ice sheets have a large potential to raise sea level. Observations of dramatic mass loss from both Greenland and Antarctica have increased attention for climate-ice sheet interactions. However, many of the observed mass losses are not direct consequences of surface melt by increased atmospheric temperatures but instead they are resulting from the dynamic flow of ice [Schoof and Hewitt, 2013]. Projections of sea level rise (SLR) are larger in the latest IPCC report [Stocker et al., 2013] than previously, mainly because of improved modeling of the contribution of dynamical mass loss from ice sheets to SLR. Changes in outflow of ice from both GIS and AIS combined are with *medium confidence* projected to contribute 0.03 to 0.20 m SLR by 2081-2100 [Stocker et al., 2013]. Confidence of such projections can increase by improved modeling of dynamical processes related to ice flow.

A large part of the West Antarctic Ice Sheet (WAIS) is based below sea level (marine-based). Sudden and irreversible ice loss from marine-based regions of the AIS in response to climate change is possible by a potential instability of the grounding line position, the location where the ice starts floating (see Figure 1). Current knowledge indicates that if

the collapse of marine-based parts of AIS is initiated, global mean SLR will be substantially larger than 0.20 m in the 21st century. In Stocker et al. [2013], it was not possible to make a quantitative assessment of this potential instability, which shows the necessity of improved modeling of ice sheet dynamics. This project therefore focuses on ice dynamics, described by a highly non-linear mathematical model, the so called Full Stokes (FS) equations. The FS equations are based on the Navier-Stokes equations adapted to the ice flow regime, coupled to a flow law which models ice viscosity.

Although the FS equations can be solved numerically to simulate GIS over one century [Seddik et al., 2012], this is not feasible yet for paleo simulations requiring time scales of hundreds of thousands years. Paleo simulations are necessary for validating ice sheet models against geological data from sediment records that allow to estimate past grounding lines. Confidence in projections of future SLR from WAIS will increase if dynamical grounding line processes in models are validated. For WAIS, grounding line variation since the Last Glacial Maximum (LGM, around 15 kyr ago) is best known. Approximations to the FS equations based on scaling analysis have been unavoidable in paleo simulations. However, it is known that the widely used Shallow Ice Approximation (SIA), is not applicable for the entire ice sheet and that there are substantial parts of the ice sheets where the scaling relations do not hold [Hutter, 1983]. Especially in regions of fast ice flow (*ice streams*) and the floating part of an ice sheet (*ice shelf*), SIA fails to model ice flow. For example on the AIS, an ice shelf the size of France is present (the Ross ice shelf) and many ice streams are observed, as shown in Figure 2. The Shallow Shelf Approximation (SSA) is commonly applied for fast flowing ice streams or ice shelves, sometimes coupled to the SIA in the slow flowing interior of the ice sheet. For example Pollard and DeConto [2009] modeled growth and collapse of the WAIS through the past five million years by combining SIA and SSA. Models combining SIA and SSA are called hybrid models, an overview of their capability of simulating the AIS is given in Bernales et al. [2017].

Besides ice streams and ice shelves, the position of the grounding line poses another challenge for ice sheet models. The results of many models with varying complexity from SIA to FS, have been compared in the Marine Ice Sheet Model Intercomparison Project (MISMIP) [Pattyn et al., 2012]. They found that even with the smallest mesh size used, the grounding line location calculated by the FS model still lies several tens of kilometres from the position found by the wide range of SSA models that participated in MISMIP. Pattyn et al. [2012] state that including all higher order corrections in the FS model, neglected by SSA models, explains the difference of the grounding line position, which indicates the necessity of solving the FS equations near the grounding line. However, the additional cost involved with solving the FS equations over the entire domain is immense, which calls for a combination of approximations in those regions where suitable and the FS model only where the approximations are inaccurate, in order to reduce computation time as much as possible.

A combination of FS and SIA has been implemented in the Ice Sheet Coupled Approximation Levels (ISCAL) method as presented in Ahlkrona et al. [2016]. The goal of this project is to extend the method by applying SSA on the ice shelves, aiming to develop a model that allows simulation of ice flow during the entire life cycle of an ice sheet (about 10.000 - 100.000 years) with high precision, such that it can be validated with geological data. The ISCAL method is implemented in the Finite Element software Elmer/Ice, where the coupling with SSA will be implemented as well. A more detailed description of the research questions and goals follows in the next section.

Coupling FS and SSA has been done before in Seroussi et al. [2012]. The method presented there is called the Tiling method, based on a blending zone where both models are solved as inspired by the Arlequin method [Dhia, 1998]. The blending zone consists of one layer of elements and a homogeneous boundary condition is imposed on either FS or SSA for all boundaries of the blending zone. Their result looks promising with respect to both accuracy and efficiency, but it is limited to diagnostic experiments only, without time evolution or dynamically evolving the domains to which certain approximation levels are applied, as is done in this project.

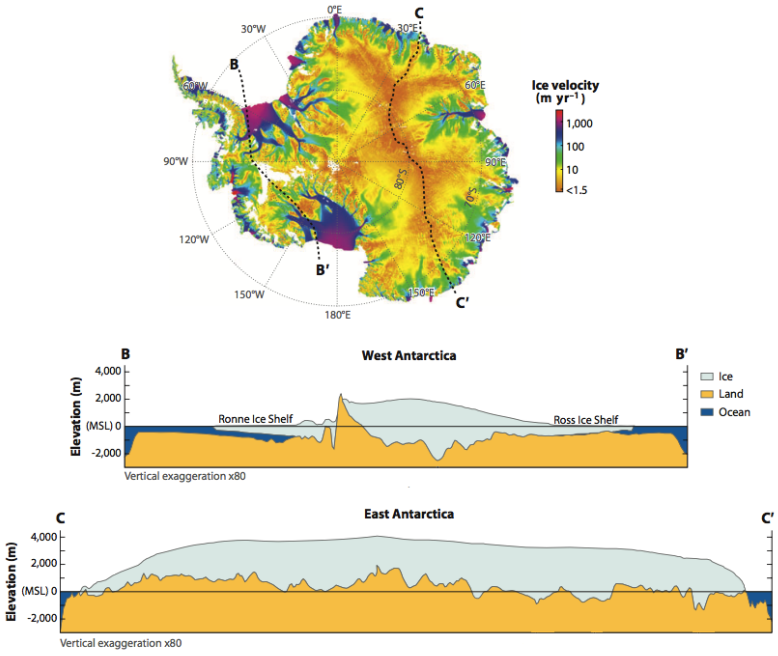

Figure 2: Antarctic surface ice velocities, adapted from Schoof and Hewitt [2013], derived from satellite radar interferometry in Rignot et al. [2011]. Bottom panels show basal topography including marine-based parts of West Antarctica, data from Lythe and Vaughan [2001].

1.1 Research questions and goals

The goal of this research assignment is to find out whether a dynamical coupling of the Shallow Ice Approximation (SIA), Shallow Shelf Approximation (SSA) and Full Stokes equations (FS) can maintain the accuracy of the FS equations while keeping computational cost manageable such that simulations on time scales of $\mathcal{O}(10^5)$ yr are possible. Such long time scales are necessary to validate the model in order to increase confidence on projections of potential instabilities on for example the WAIS. Since it is not feasible to solve the FS equations on $\mathcal{O}(10^5)$ time scales, approximations are unavoidable. The aim is to restrict the use of approximations to regions where these approximations are indeed valid. Since it is not possible to define such regions a priori, a dynamical coupling of the different solution methods is necessary. The research questions are:

1. Is the SIA-FS coupling in the ISCAL method as described in Ahlkrona et al. [2016] accurate for ice sheet modeling?
    - The robustness is assessed for longer time spans than published in Ahlkrona et al. [2016] (where ISCAL is applied up to 2.5 years).
2. In what way can the SSA and FS equations be coupled?
    - The solutions of the SSA and FS equations are compared for a floating ice shelf, in order to distinguish errors resulting from the difference of the two models and errors resulting from the coupling.
    - A coupled model for a predefined domain division of $\Omega_{SSA}, \Omega_{FS}$ is implemented and tested for the ice shelf.
    - Criteria for dynamically dividing $\Omega_{SSA}, \Omega_{FS}$ are suggested.
3. How accurate and efficient is the SSA - FS coupling for grounding line problems?
    - The SSA-FS coupling is applied to conceptual marine ice sheets cross-sections.
    - The suggested criteria for dividing $\Omega_{SSA}, \Omega_{FS}$ are evaluated.
    - Efficiency and accuracy is examined for both diagnostic and prognostic experiments.

As mentioned in the Preface, the first question belongs to the MSc CP, the second to MSc AM and the final question to both. Instead of implementing the coupling with SSA inside ISCAL, it was chosen to implement the coupling such that SSA can be coupled to any model solving for the velocity in the rest of the domain. Testing the coupling of SSA with FS instead of ISCAL is motivated by the application to grounding line problems, which all assume rapid sliding at the grounded part such that SIA is anyhow not applicable. Another reason for implementing the SSA-FS coupling such that it does not rely on a particular solver for the FS equations, is that the coupling is more flexible to changes in the FS solver than ISCAL (which is implemented by hard coding changes to Elmer/Ice's *FlowSolver*). Therefore, the coupling automatically works with the newest version of the

FS and SSA solvers in Elmer/Ice. This was also motivated by instabilities found in the FS solution when studying the first research question, which calls for improved stabilization for the FS solver.

It should be stressed that whenever 'accuracy of the coupled model' is mentioned, this refers to the accuracy of the coupled model with respect to the FS model. Investigating the accuracy of the FS model is outside of the scope of this project. Therefore, no convergence study of the FS model with respect to discretization in either time or space is done. Instead, the FS and coupled model are performed with equivalent settings, such that a comparison of the two can be done and the FS model is regarded as reference solution.

1.2 Thesis outline

First, the research questions are formulated in Section 1.1. An overview of the equations governing ice sheet dynamics and their approximations is given in Section 2, together with boundary conditions and a description of the physical marine ice sheet instability hypothesis, that motivates the focus on ice flow. Then the weak formulations of the FS and SSA equations are derived in Sections 3.1 and 3.2. The Finite Element software Elmer/Ice is described in Section 3.3, ISCAL in Section 4.1 and the method for coupling SSA and FS in Section 4.2.

A description of the experiments and their results follow in Section 5, with Section 5.1 focussing on the first research question regarding ISCAL's accuracy. Sections 5.2, 5.3.1.1 and 5.3.3 address coupling of SSA and FS, the second research question. Sections 5.3.1.2 - 5.3.2.2 regard the third question, assessing both accuracy and efficiency of the SSA - FS coupling. The main conclusions are given in Section 6 and suggestions for further research in the coupling of SIA, SSA and FS are given in Section 7.

2 Ice sheet dynamics

2.1 Governing equations

Ice is considered as being an *incompressible* fluid, such that mass conservation implies

$$\nabla \cdot \mathbf{u} = 0, \tag{1}$$

where $\mathbf{u} = (u_1, u_2, u_3)^T = (u, v, w)^T$ describes the velocity field in the ice with respect to a Cartesian coordinate system $(x_1, x_2, x_3)^T = (x, y, z)^T$. Conservation of linear momentum implies a balance between the driving force of gravity and the resisting forces caused by drag. The intensity of a force acting on a surface depends on the area which it is acting on, this is expressed by the *stress* (σ), defined as force over unit area. The amount of deformation that occurs resulting from the stress is defined as *strain*. Strain rates are given by spatial velocity gradients, since they present the relative motion of different parts of the ice, such that the components of the strain rate tensor $\mathbf{D}$ can be written as

$$D_{ij} = \frac{1}{2}\left(\frac{\partial u_i}{\partial x_j} + \frac{\partial u_j}{\partial x_i}\right) \text{ for } i, j \in \{1, 2, 3\} \tag{2}$$

hence

$$\mathbf{D}(\mathbf{u}) = \frac{1}{2}(\nabla \mathbf{u} + (\nabla \mathbf{u})^T). \tag{3}$$

Forces can either act perpendicular to a surface, inducing normal stress (σ_{ii}) or act parallel to a surface, inducing shear stress (σ_{ij}). The mean normal stress is known as the pressure ($p = \Sigma_i 1/3\sigma_{ii}$). Deviatoric stress ($\tau$) represents a deviation from the mean and therefore express the part of the stress σ that induces deformation. In tensor form these stresses relate to each other as

$$\sigma_{ij} = \tau_{ij} - p\delta_{ij}, \tag{4}$$

where δ_{ij} represents the Kronecker delta. The deformation resulting from applied stresses varies per material and the relation between stress and strain is called the *rheology* of a material. It is well known that the response to stresses depends on the orientation of crystals within the ice, such that a realistic but complex description of the rheology of ice would need to include anisotropic effects. However, on the large scale of an ice sheet, ice can be approximated to behave as an isotropic material. In that case, the resulting strain is equal for a certain applied stress, regardless of the direction in which the stress is applied. Moreover, we will assume here that ice behaves as a viscous material, hence the variable that measures the gradual deformation caused by deviatoric stresses is called the viscosity η:

$$\tau_{ij} = 2\eta D_{ij}. \tag{5}$$

Observations by Glen and Nye in the early 1950's suggest that the viscosity of ice depends on its temperature (T) and on the strain rate through its second invariant, also called

effective strain rate D,

$$\begin{aligned} D(\mathbf{u}) &= \sqrt{\frac{1}{2}D_{ij}D_{ij}} \\ &= \frac{1}{\sqrt{2}}\sqrt{\left(\frac{\partial u}{\partial x}\right)^2+\left(\frac{\partial v}{\partial y}\right)^2+\left(\frac{\partial w}{\partial z}\right)^2+} \\ &\quad \overline{\frac{1}{2}\left(\frac{\partial u}{\partial y}+\frac{\partial v}{\partial x}\right)^2+\frac{1}{2}\left(\frac{\partial u}{\partial z}+\frac{\partial w}{\partial x}\right)^2+\frac{1}{2}\left(\frac{\partial v}{\partial z}+\frac{\partial w}{\partial y}\right)^2}. \end{aligned} \tag{6}$$

The dependence of the viscosity on the effective strain rate can then be modeled by

$$\eta(\mathbf{u},T) = \mathcal{A}(T)^{-1/n} D(\mathbf{u})^{(1-n)/n}, \tag{7}$$

where Glen's exponent $n = 3$ is usually assumed. The fluidity parameter $\mathcal{A}$ increases exponentially with temperature as described by the Arrhenius relation [Paterson, 1994] for T [°C],

$$\mathcal{A}(T) = \begin{cases} 2 \cdot 3.985 \cdot 10^{-13} e^{\frac{-60\cdot 10^3}{8.314(273.15+T)}} \text{ for } T < -10°C, \\ 2 \cdot 1.916 \cdot 10^{-13} e^{\frac{-139\cdot 10^3}{8.314(273.15+T)}} \text{ for } -10 \leq T \leq 0°C, \\ 2 \cdot 1.916 \cdot 10^{-13} e^{\frac{-139\cdot 10^3}{8.314\cdot 273.15}} \text{ for } T > 0°C, \end{cases} \tag{8}$$

which shows that ice flow is strongly dependent on temperature. This calls for a thermodynamically coupled system of equations, where the effect of advection, conduction, and strain heating on the temperature distribution is included as well. However, this project focuses on the mechanical effects, therefore a uniform temperature will be assumed. The uniform temperature assumed varies for different experiments.
Newton's second law of motion describes fluid dynamics as

$$-\nabla p + \nabla \cdot \boldsymbol{\tau} + \rho \mathbf{g} = \frac{d\mathbf{u}}{dt} = \frac{\partial \mathbf{u}}{\partial t} + \mathbf{u} \cdot \nabla \mathbf{u}, \tag{9}$$

where $\frac{d\mathbf{u}}{dt}$ denotes the material derivative and ρ the density of ice. Since isothermal conditions are assumed, the ice density ρ is constant. This equation expresses conservation of linear momentum, the inertia forces caused by changes in velocity $\mathbf{u}$ are balanced by pressure gradients ∇p, stresses $\boldsymbol{\tau}$ and acceleration by gravity $\mathbf{g}$. Reynolds numbers for typical ice sheet flow are extremely low, on the order of 10^{-12}, such that this acceleration term can be neglected in the Navier-Stokes equations [Weis, 2001], [Hutter, 1982]. Therefore, the conservation of momentum under the action of gravity $\mathbf{g}$ can be described by

$$-\nabla p + \nabla \cdot \boldsymbol{\tau} + \rho \mathbf{g} = \mathbf{0}, \tag{10}$$

where $\boldsymbol{\tau}$ is the deviatoric stress tensor. Substitution of the stress tensor then yields

$$-\nabla p + \nabla \cdot \left(\eta(\mathbf{u})(\nabla \mathbf{u} + (\nabla \mathbf{u})^T)\right) + \rho \mathbf{g} = \mathbf{0}, \tag{11}$$

together with Glen's flow law (Eq. 7) and incompressibility (Eq. 1) these are called the Full Stokes (FS) equations. They are computationally demanding to solve, because the dependence of the viscosity on ice velocity in Glen's flow law introduces a non-linearity

even if the temperature is assumed constant. Therefore, many approximations to the FS equations have been derived in order to model ice sheet dynamics. Most approximations build on the characteristic of ice sheets that their horizontal scale is much larger than their vertical scale. This yields both the Shallow Ice Approximation (Sec. 2.1.2) and the Shallow Shelf Approximation, also called Shelfy Stream Approximation (Sec. 2.1.3).

2.1.1 Hydrostatic Approximation

In terms of the stress tensor $\boldsymbol{\sigma}$, the momentum balance as in Equation 10 can be written as

$$\nabla \cdot \boldsymbol{\sigma} = \rho \mathbf{g}. \tag{12}$$

The shear stresses σ_{xz}, σ_{yz} are small in all parts of an ice sheet compared to the vertical normal stress σ_{zz} [Greve and Blatter, 2009] and the horizontal gradients of σ_{xz}, σ_{yz} are even one order smaller. Hence, the vertical momentum balance can be simplified to

$$\frac{\partial \sigma_{zz}}{\partial z} = \rho g, \tag{13}$$

which is easily solved, assuming the upper surface at $z = z_s$ to be stress-free, to yield

$$\sigma_{zz}(z) = -\rho g(z_s - z). \tag{14}$$

Since the deviatoric stress is traceless [Greve and Blatter, 2009], using Equation 4, the pressure p can be rewritten as

$$p = p - \mathrm{tr}(\boldsymbol{\tau}) = \rho g(z_s - z) - \tau_{xx} - \tau_{yy}. \tag{15}$$

Now the horizontal components of the momentum balance can be simplified, using the stress-free surface boundary condition, to

$$\begin{aligned} 2\frac{\partial \tau_{xx}}{\partial x} + \frac{\partial \tau_{yy}}{\partial x} + \frac{\partial \sigma_{xy}}{\partial y} + \frac{\partial \sigma_{xz}}{\partial z} &= \rho g \frac{\partial z_s}{\partial x}, \\ 2\frac{\partial \tau_{yy}}{\partial y} + \frac{\partial \tau_{xx}}{\partial y} + \frac{\partial \sigma_{xy}}{\partial x} + \frac{\partial \sigma_{yz}}{\partial z} &= \rho g \frac{\partial z_s}{\partial y}. \end{aligned} \tag{16}$$

This set of equations is called the hydrostatic approximation and often forms the basis of SIA as well as SSA. However, both approximation levels have been derived in alternative ways as well. For instance in Jouvet [2016], the approximations are constructed from the weak form.

2.1.2 Shallow Ice Approximation

The Shallow Ice Approximation (SIA) assumes that ice sheets are shallow, hence their horizontal scale is much larger than their vertical extent. Indeed, the ratio between ice thickness and horizontal extent is of the order 10^{-3} for large ice sheets [Blatter et al., 2011], [Hutter, 1983].

This aspect ratio $\epsilon = \mathcal{O}(10^{-3})$ can be used to scale all variables in Equations 1, 3, 7 and 11 to dimensionless form in terms of ϵ. Several approximations to the FS equations

can be made by perturbation analysis [Courant and Hilbert, 1953]. The SIA follows from neglecting all variables with order one or higher and is therefore a zeroth order approximation. As explained in Ahlkrona et al. [2013a], what remains is that all resistance to the gravity driven flow is at the basal boundary of the ice; the only remaining deviatoric stresses are shear stresses acting on horizontal planes, τ_{xz} and τ_{yz}. Since the normal stress deviators τ_{ii} are negligible, the pressure is equal to any of the normal stresses,

$$p = -\sigma_{xx} = -\sigma_{yy} = -\sigma_{zz} = \rho g(z_s - z), \tag{17}$$

where the last equality follows from the hydrostatic approximation and therefore called the hydrostatic pressure distribution. The only remaining terms of Equation 16 are

$$\begin{aligned} \frac{\partial \sigma_{xz}}{\partial z} &= \rho g \frac{\partial z_s}{\partial x}, \\ \frac{\partial \sigma_{yz}}{\partial z} &= \rho g \frac{\partial z_s}{\partial y}. \end{aligned} \tag{18}$$

With the same scaling, the effective strain rate given by Equation 6, simplifies to

$$D = \sqrt{\sigma_{xz}^2 + \sigma_{yz}^2} = \rho g(z_s - z)|\nabla z_s|. \tag{19}$$

Now Equation 18 can be solved algebraically by vertical integration and solving for the stresses. Finally, the stresses can be used to calculate the velocity field directly from the geometry, using the simplified effective strain rate and Glen's flow law (Eq. 7), combined with incompressibility, such that:

$$u(z) = u_b - 2(\rho g)^3 \frac{\partial z_s}{\partial x} ||\nabla z_s||^2 \int_{z_b}^{z} \mathcal{A}(z_s - s)^3 \mathrm{d}s, \tag{20}$$

$$v(z) = v_b - 2(\rho g)^3 \frac{\partial z_s}{\partial y} ||\nabla z_s||^2 \int_{z_b}^{z} \mathcal{A}(z_s - s)^3 \mathrm{d}s, \tag{21}$$

$$w(z) = -\int_{z_b}^{z} \left(\frac{\partial u}{\partial x} + \frac{\partial v}{\partial y} \right) \mathrm{d}s, \tag{22}$$

where u_b, v_b are tangential basal sliding velocities, $||\cdot||$ the Euclidean vector norm, gravity constant $g = ||\mathbf{g}||$, z_s the ice sheet surface elevation and z_b the elevation of the ice base (see Figure 3). It is used here that the surface is stress-free and that the basal velocity $w_b = 0$, which follows from the contact with the rigid bedrock and neglecting basal melt.

This model is numerically cheap to solve and therefore the standard approach in glaciology for modeling ice sheets on paleo time scales. However, it is long known that this is inappropriate for many situations such as ice divides, ice streams and transition zones between grounded and floating ice. The problems occur due to the non-linear, singular nature of the viscosity. Because all normal stresses σ_{ii} and the horizontal plane shear stress σ_{xy} are neglected, the effective stress becomes zero wherever the vertical shear stresses are zero, hence at the entire ice surface. Ahlkrona et al. [2013a] showed that a boundary layer develops near the entire ice surface when there is a bumpy bed, due to the non-linear rheology of ice. There is no unique definition of the boundary layer, but when defining the border where τ_{xx} is 10% of its maximum value gives a boundary layer that reaches

about half the ice thickness for an aspect ratio of about 10^{-3}. It should be noted that the finding that the SIA-scalings do not hold in this boundary layer does not imply that the SIA is invalid, but the order of approximation can not be expected to satisfy the second order accuracy as classical theory suggests [Schoof and Hindmarsh, 2010]. A possibility to overcome this problem would be to include also higher orders of ϵ, but in Ahlkrona et al. [2013b] it has been shown that a higher order model still needs an artificial parameter to avoid singularities in the viscosity and results of these higher order model are very sensitive to this parameter. However, there is no straightforward way to determine this value and therefore instead a combination of FS and the zeroth order SIA might overcome these problems.

2.1.3 Shallow Shelf Approximation

The SIA is inappropriate in regions of rapid sliding since some of the ignored stress components can become large [Schoof and Hindmarsh, 2010]. Another region where SIA does not hold is for ice shelves, the parts of the ice sheet that are floating. Since floating ice does not experience basal drag, all resistance must come from longitudinal stresses or lateral drag at the margins. For these regions, a so-called membrane model has been developed [MacAyeal, 1989], [Morland, 1987]. It also builds on the hydrostatic approximation, but low basal friction in combination with dimension analysis based on the small aspect ratio and small surface slope show instead that vertical shearing is negligible and lateral shear stresses dominate ice shelf flow. The resulting approximation is also called the Shallow Shelf Approximation or Shelfy Stream Approximation (SSA). A schematic overview of an ice shelf and the related variable definitions are shown in Figure 3.

By depth integrating horizontal stretching and horizontal plane shearing terms in the

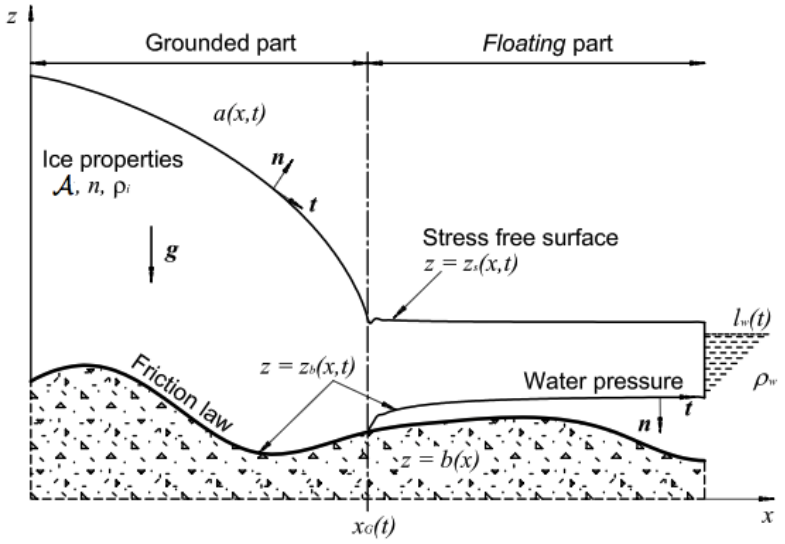

Figure 3: Schematic view of an ice shelf system and the related variables, adapted from Durand et al. [2009a].

FS equations 1 and 11 and applying Leibnitz rule for differentiation of integrals, the SSA

equations are given by

$$\frac{\partial}{\partial x}\left(4H\bar{\eta}\frac{\partial u}{\partial x}+2H\bar{\eta}\frac{\partial v}{\partial y}\right)+\frac{\partial}{\partial y}\left(H\bar{\eta}\frac{\partial u}{\partial y}+H\bar{\eta}\frac{\partial v}{\partial x}\right) = -\tau_x+\rho g H\frac{\partial z_s}{\partial x}, \quad (23)$$

$$\frac{\partial}{\partial y}\left(4H\bar{\eta}\frac{\partial v}{\partial y}+2H\bar{\eta}\frac{\partial u}{\partial x}\right)+\frac{\partial}{\partial x}\left(H\bar{\eta}\frac{\partial u}{\partial y}+H\bar{\eta}\frac{\partial v}{\partial x}\right) = -\tau_y+\rho g H\frac{\partial z_s}{\partial y}, \quad (24)$$

where $\bar{\eta}$ represents the vertically averaged viscosity, H the thickness of the ice sheet and τ_i the components of basal stress, depending on the boundary condition [MacAyeal, 1989][1]. In contrast to the SIA equations, the SSA equations are non-linear since they depend $\bar{\eta}$. Computational gain of coupling FS to SSA is however expected since the vertical velocity and pressure are decoupled from the horizontal velocities, such that the degrees of freedom of the non-linear system is 2N, compared to 4N for the FS equations (where N is the number of nodes).

In many applications, the horizontal velocity is of main interest and vertical velocity is not computed, for example since results are validated by comparison to observed horizontal surface velocity from satellite data. If desirable, the vertical velocity can be computed from the incompressibility condition after the iterative computation of the horizontal velocities has converged. Since the vertical derivatives of the horizontal velocities are zero, the incompressibility condition of Equation 1 can be integrated directly such that

$$w(z)=(z_s-z)\left(\frac{\partial u}{\partial x}+\frac{\partial v}{\partial y}\right)+w_s. \quad (25)$$

A boundary condition for the vertical velocity needs to be specified since it comes in as integration constant w_s in Equation 22. As an example, in Greve and Blatter [2009] it is assumed that the ratio of surface and basal mass balance is such that the vertical velocity vanishes at sea level $z=0$ which would yield $w(z)=-z\left(\frac{\partial u}{\partial x}+\frac{\partial v}{\partial y}\right)$. However, the integration constant can be calculated directly if both the surface and basal mass balance are known as will be explained in Section 3.2. Finally, the pressure follows from Equation 15.

Hybrid models have been developed that couple SIA and SSA across the grounding line, the point where the shelf starts floating as shown in Figure 3. However, Wilchinsky and Chugunov [2001] proved using matched asymptotics that the FS equations need to be solved in a boundary layer between the shelf and no-slip ice flow on a sheet. The transition from a fast flowing ice stream to an ice shelf on the other hand is easier since both can be approximated by the same SSA equations, but then the difficulty of matching is located in the shear margin where the ice stream meets regions where the ice is frozen to the bed. Again, it has been shown that the FS equations should be solved to fully capture the dynamics (Raymond [1996],Schoof [2004]).

By the Archimedes' principle, floating ice shelves do not have a direct effect on sea level

[1] Opposed to Greve and Blatter [2009], where vertically integrated viscosity is used and hence no term H is present.

rise when they melt. On the other hand, they may indirectly influence resisting forces governing the ice flow in the ice sheet, also called the 'buttressing effect' [Dupont and Alley, 2005] which importance will be addressed in more detail in Section 2.3. To include the buttressing effect, a complete ice sheet model requires modeling of the shelves as well.

2.2 Boundary Conditions

2.2.1 The ice surface

Neglecting atmospheric pressure, the ice surface at z_s is stress free and therefore behaves as a free boundary according to

$$\frac{\partial z_s}{\partial t} + u_s \frac{\partial z_s}{\partial x} + v_s \frac{\partial z_s}{\partial y} = w_s + a_s \tag{26}$$

where a_s is the rate of mass gain ($a_s > 0$, accumulation) or loss ($a_s < 0$, ablation) at the surface per unit area. On ice shelves, the ice base also acts as a free surface such that

$$\frac{\partial z_b}{\partial t} + u_b \frac{\partial z_b}{\partial x} + v_b \frac{\partial z_b}{\partial y} = w_b + a_b. \tag{27}$$

Since the bedrock is assumed to be rigid and impenetrable at elevation b, the so-called free surface Equations 26 and 27 are subject to $z_s(x, y, t) > z_b(x, y) \geq b(x, y, t)\ \forall x, y, t$. Instead of the free surface equations, the elevations z_s, z_b can also be replaced by the ice thickness $H(x, y, t) = z_s(x, y, t) - z_b(x, y, t)$. Substituting the ice flux defined as

$$q_x = \int_{z_b}^{z_s} u \, \mathrm{d}z, \quad q_y = \int_{z_b}^{z_s} v \, \mathrm{d}z, \tag{28}$$

yields the so-called thickness advection equation:

$$\frac{\partial H}{\partial t} + \frac{\partial q_x}{\partial x} + \frac{\partial q_y}{\partial y} = a_s + a_b. \tag{29}$$

Note that these are the first equations that involves a time dependency. Care needs to be taken when choosing a discretization scheme and time step Δt in order to find accurate and stable solutions. This will be discussed in more detail in Section 3.3.2. In this project, both free surface equations 26, 27 and the thickness advection equation 29 will be used. The advantage of the latter is that it is not necessary to know the vertical velocity, which will turn out to be important since the vertical velocity is more prone to numerical instabilities than the horizontal velocities. However, in order to derive the adjusted surface elevations from the thickness advection equations, either the basal elevation z_b needs to be fixed (from contact with the bedrock) or the surface elevations need to satisfy the floatation criterion. This criterion can be derived from Archimedes' principle and yields

$$z_s = z_{sea} + \left(1 - \frac{\rho}{\rho_w}\right) H, \quad z_b = z_{sea} - \frac{\rho}{\rho_w} H. \tag{30}$$

Here, it is assumed that the sea level $z_{sea} = 0$ m. Most marine ice sheet models apply the floatation criterion directly when the ice starts floating. However, Durand et al. [2009a] showed that modeling the surface evolution by the free surface equations, applying

a hydrostatic pressure at the sea-ice interface, gives a steady state ice shelf that does not comply with the floatation condition but shows a small depression downstream of the grounding line, followed by small surface oscillations. However, this feature is only observed in the model results close to the grounding line, their steady state ice shelf is at floatation approximately 5 km downstream of the grounding line. Such a surface pattern has also been observed in the field [Anandakrishnan et al., 2007]. Despite the violation of the floatation criterion being very local, applying the floatation criterion may influence the grounding line dynamics. Since the thickness advection equation can only be used to model surface evolution when the shelf is floating, the region around the grounding line should therefore be modeled by the free surface equations [Durand et al., 2009a].

2.2.2 Grounded ice

Where the ice is grounded (in contact with the bedrock) the interaction of ice with the bedrock needs to be parametrized. To start with, the most simple boundary condition at the bed is assumed, namely a no slip condition, where the ice is frozen to the bed:

$$\mathbf{u}_b = 0. \tag{31}$$

However, for a non flat bed it is not realistic to assume the ice never slides over the bed. Therefore, another possibility is to assume a sliding law $f(\mathbf{u}, N)$, that relates the basal velocity $\mathbf{u}_b$ and effective pressure N (depending on the possible presence of water at the ice base) to the basal shear stress as

$$(\mathbf{t}_i \cdot \boldsymbol{\sigma} \cdot \mathbf{n})_b = f(\mathbf{u}, N)\mathbf{u} \cdot \mathbf{t}_i, \quad i = 1, 2 \tag{32}$$

$$(\mathbf{u} \cdot \mathbf{n})_b + a_b = 0, \tag{33}$$

where $\mathbf{t}_i$ are the vectors spanning the plane tangential to the bed, $\mathbf{n}$ is the normal to the bed and a_b denotes basal melt and refreezing. Ideally, N would be calculated from a sub-glacial hydrology model but that is beyond the scope of this project. Instead, basal melt or refreezing at the bed will be neglected ($a_b = 0$). As can be seen from Equation 20, the SIA solution requires the sliding law to be invertible in order to calculate the bottom velocities u_b, v_b. Therefore, all sliding laws that will be assumed in this project are invertible. The most basic sliding law assumes a linear relation,

$$f(\mathbf{u}, N) = -\beta. \tag{34}$$

The sliding coefficient $\beta \geq 0$ determines the amount of friction, where β is low, the friction between the bed and ice is low, hence the ice will slide. If observed surface velocities are available, β is often determined by inverse modeling. In that way, regions where ice streams (fast flowing ice) are present will be *defined* to have low β such that the model is able to reproduce the high observed velocities [Schäfer et al., 2013]. Another way to simulate fast sliding areas in regions of high-mountain topography is to impose a relation between the basal elevation and the sliding coefficient, as was done in Kirchner et al. [2016].

The second sliding law that does not require modeling of the effective pressure is a Weertman type sliding law [Weertman, 1957]:

$$f(\mathbf{u}, N) \quad = \quad -\beta_m u_b^{m-1}, \tag{35}$$

where u_b is the magnitude of the sliding velocity. In theory, for ice sliding when in touch with an undulating bed the exponent $m = 1/n$ where n is the exponent in Glen's law [Lliboutry, 1968].

Budd's sliding law is a modification to the Weertman type sliding law, suggested by laboratory experiments [Budd et al., 1979] and simulations of Antarctica [Budd et al., 1984]. Besides the power law dependence on the velocity, it also depends on the height above buoyance z_* such that

$$f(\mathbf{u}, N) \quad = \quad -\beta_m u_b^{m-1} z_*^q, \tag{36}$$

where z_* would ideally be calculated from N, but here it is assumed to follow from a hydrostatic balance as

$$z_* = \begin{cases} H & \text{if } z_b \geq z_{sl}, \\ H + z_b \frac{\rho_w}{\rho} & \text{if } z_b < z_{sl}. \end{cases} \tag{37}$$

Since z_b is assumed negative, this implies that z_* equals zero as soon as Archimedes' principle (Eq. 30) is satisfied. The assumption of a hydrostatic balance can be regarded as a sub-glacial hydrology system entirely connected to the ocean. All of the above stated sliding laws will be assumed in several experiments, as described for each experiment separately in Section 5.

2.2.3 The grounding line and shelf

The ice is allowed to move away from the bed and start floating, such that the grounding line can move over time. Cohesive forces that may need to be overcome before the ice can detach from the bed are neglected here. Instead, as soon as the seawater pressure p_w at the ice base z_b is larger than the normal stress exerted by the ice at the bed $\sigma_{nn}|_b$, the ice is assumed to float. Hence, the boundary condition for bedrock (Section 2.2.2) is assumed if

$$z_b(x, y, t) = b(x, y) \text{ and } -\sigma_{nn}|_b > p_w(z_b, t) \tag{38}$$

and a boundary condition for contact with the sea is applied wherever

$$\begin{aligned} z_b(x, y, t) &> b(x, y), \\ \text{or } z_b(x, y, t) = b(x, y) \text{ and } -\sigma_{nn}|_b &\leq p_w(z_b, t). \end{aligned} \tag{39}$$

For a detailed description of the implementation of the contact problem at the grounding line, see Durand et al. [2009a]. Where the ice base meets the seawater, the tangential friction is neglected ($f(\mathbf{u}, N) \equiv 0$ in Equation 32) and the hydrostatic seawater pressure varies with z as

$$p_w(z, t) = \rho_w g(l_w(t) - z) \text{ if } z < l_w(t), \;\; p_w(z, t) = 0 \text{ otherwise}, \tag{40}$$

where l_w is the sea level and ρ_w the sea water density. This condition applies to the calving front as well. Calving will not be modeled explicitly, but instead the modeling domain is assumed to be fixed and any flow on the shelf out of the domain is interpreted as mass loss by calving.

2.3 Marine ice sheet instability

The potential instability of marine-based parts of an ice sheet, as mentioned in the introduction, is called the marine ice sheet instability (MISI). This section explains the theory behind MISI, which motivated the focus of the Marine Ice Sheet Model Intercomparison Project (MISMIP) on grounding line dynamics. Afterwards, the experiments of MISMIP are introduced and published MISMIP results using Elmer/Ice are discussed.

Marine ice sheets (MISs) with a bedrock below sea level sloping downwards towards the ice sheet's centre (retrograde) have since long been argued to be unstable and prone to rapid disintegration. In short, the MISI hypothesis relies on the assumption that ice discharge through the grounding line increases with the local ice thickness. Suppose then that a MIS has its grounding line located on an retrograde sloping bed. A small grounding line retreat will lead to an increase in ice thickness at the grounding line and hence increased ice discharge. This forms a positive feedback: the increase in ice discharge would lead to more dynamic mass loss in the ice sheet and hence further grounding line retreat, giving an increase in ice discharge and so on. This feedback may stop if the grounding line reaches a region of reversed bed slope, which with likewise reasoning has a negative feedback with ice discharge and is thus stable to small perturbations.

However, the assumption that ice discharge through the grounding line increases with local ice thickness has been debated. The first quantitative study of this (in)stability [Weertman, 1974] under very simplified conditions found that a retrograde slope always makes a marine ice sheet unstable. Thomas and Bentley [1978] concluded similarly and raised awareness of the idea of a MISI by showing its relevance for the AIS. Contrastingly, Hindmarsh [1993] argued that in case the grounded ice experiences high basal drag, the sheet and shelf dynamics are not coupled, such that ice discharge and grounding line thickness are not as strongly coupled either. This arguing leads to the possibility of a retrograde sloping MIS that can show a "neutral equilibrium", such that a perturbation to the grounding line position can result in a new, distinct steady state close to the original one before applying the perturbation. Continuing on this problem, Schoof [2007] investigates MISI with a boundary layer theory for the grounding line zone, which allows to calculate ice flux across the grounding line by integrating a local ice flow problem. Using this theory, no such neutral equilibria exist on retrograde bed slopes.

The contrasting results show that solving the grounding line problem numerically is more difficult than anticipated. Several studies show a strong dependency of the calculated

grounding line position to grid resolution, for both hybrid [Vieli and Payne, 2005], [Gladstone et al., 2012] and later FS models [Gagliardini et al., 2016]. To find out whether these inconsistent findings originate from the differences in experiment set up amongst these studies, or by differences in the models applied, MISMIP was organized.

The main questions aimed to be answered by MISMIP are whether steady states are distinct and whether bed slope controls their stability, but it also questions to what extent high grid resolution is necessary to obtain reliable results. In order to allow as many models as possible to participate and to find out how well they agree with one another, all experiments are based on an idealised two dimensional ice sheet geometry, considering an ice sheet along a flow-line, without lateral variations [Pattyn et al., 2012]. By the combination of theoretical studies [Schoof, 2007] and joint effort by the numerical glaciology community [Pattyn et al., 2012], now there is a general understanding that such flow-line MISs with rapid sliding on a retrograde slope as in MISMIP are indeed subject to MISI.

In the more general three dimensional case however, dependence of (in)stability on bedrock slope may be different. Ice shelves provide a resistance force by buttressing and thereby can stabilise the grounding line position of a three dimensional MIS on retrograde slope. Gudmundsson et al. [2012] confirmed this theory by showing (using a model called Úa based on SSA and Elmer/Ice) specific numerical examples of model geometries that sections of stable grounding line positions can be located on retrograde slopes. Again, the numerical glaciology community joined efforts to investigate grounding line dynamics in three dimensions in the ice2sea MISMIP3d intercomparison [Pattyn et al., 2013]. MISMIP3d is based on MISMIP, using a similar experimental set-up with a bedrock that does not vary in y to allow comparison with the flow-line case. However, the intercomparison aims to validate the capability of modeling grounding line migration in general, not to investigate the MISI. This explains why the experiments do not include retrograde bed slopes. Pattyn et al. [2013] concluded that numerical errors associated with modeling grounding line motion can be reduced significantly below the errors related to other uncertainties such as bedrock properties and future scenarios for basal melt underneath the shelves.

The history of grounding line positions can be estimated by analysis of subglacial landforms and sediments. In Cofaigh et al. [2008], geological data for a limited region of WAIS is analyzed, showing a rapid grounding line retreat over an overdeepened trough from its furthest position during the LGM about 14 kyr ago. However, they find stable grounding lines of centuries or longer on retrograde slopes are recorded in sediment cores. Both observational and modeling studies on the stability of the WAIS were reviewed in Joughin and Alley [2011], where it is concluded that confident projections of the fate of the ice sheet and the rate of any possible collapse, requires (amongst others) well-validated physical models.

2.3.1 Previous MISMIP-like experiments using Elmer/Ice

MISMIP compared models of varying complexity on an idealized two dimensional ice sheet geometry, focussing on their capability of computing grounding line dynamics. A detailed description of the experiments is given at `http://homepages.ulb.ac.be/~fpattyn/mismip/` and the results of all participating models are summarized in Pattyn et al. [2012]. The only FS model that participated in the intercomparison project is Elmer/Ice, the model applied in this study. To focus on the grounding line dynamics, several assumptions are made for the original MISMIP experiments, the ice is assumed to be:

- an isotropic material, obeying Glen's flow law (Eq. 7),
- isothermal; no melting/refreezing at base ($a_b = 0$ m yr^{-1}),
- sliding according to a Weertman type sliding law as in Equation 35,
- the bed is rigid (no glacial isostatic rebound) and impenetrable.

The original implementation and results of MISMIP in Elmer/Ice are discussed in Durand et al. [2009a]. Durand et al. [2009b] discusses the influence of the grid size close to the grounding line using a convergence study. It is well known that the discontinuity of the boundary condition at the ice base, where friction from sliding is suddenly neglected as soon as the ice starts to float, is numerically hard to solve. The impact of mesh resolution on both two and three dimensional MISMIP-like experiments is discussed further in Gagliardini et al. [2016]. There, the friction law is adapted such that it is not discontinuous at the grounding line but instead decreases continuously, over a transition distance, to zero at the grounding line. They find that the continuous friction law does not reduce sensitivity to the mesh resolution and that the results are very sensitive to the way the friction is interpolated over the transition zone. The remaining resolution dependence for such fine meshes motivates the use of sub-grid parametrisations of the position of, or flux over, the grounding line as has been done in Pattyn et al. [2006], Pollard and DeConto [2009], Gladstone et al. [2010] and Feldmann et al. [2014]. However, none of these parametrisations was done in Elmer/Ice and implementation of the grounding line dynamics is outside the scope of this project.

Gladstone et al. [2017] on the other hand finds that a continuous friction law does reduce the sensitivity to the mesh resolution. Assuming Budd's sliding law (Eq. 36), applying the adapted sliding to a MISMIP-like experiment[2], they show reduced influence of mesh resolution near the grounding line compared to the original Weertman sliding law (Eq. 35) which is discontinuous at the grounding line. This finding appears to contradict the results of Durand et al. [2009b] and Gagliardini et al. [2016] which did not show any improvement by adapting the sliding law to be continuous. However, the transition zone over which the sliding law is adapted in Durand et al. [2009b] and Gagliardini et al. [2016] is much smaller, typically of the same order of magnitude as the element size, whereas the length

[2]Also two-dimensional but a slightly different bedrock elevation and accumulation, see Section 5.3.1.3

of the transition zone reaches up to several hundred kilometres in Gladstone et al. [2017].

Since the model intercomparison studies MISMIP(3d) use Weertman's sliding law, a similar experiment is performed here as well. Because convergence of the FS model in Elmer/Ice is not subject of the current study, the mesh resolution around the grounding line will be based on the convergence study by Durand et al. [2009a]. However, a spatial range of 2 km persisted in which their modeled ice sheet reached a steady grounding line position after perturbation, even with the finest mesh they used. They state that the observed neutral equilibrium is a numerical artefact. Therefore, the alternative sliding law as proposed in Gladstone et al. [2017], which does not show high resolution dependence, is considered here as well, in order to allow for experiments on a longer time scale. Physical justification to use of Budd's sliding law would be stronger if the effective pressure N is modeled by a sub-glacial hydrology, instead of assuming hydrostatic equilibrium. However, this would in turn increase computation time counteracting the computational gain from the coarser mesh. The aim of the grounding line experiments in this project is to validate the capability of a new SSA-FS coupling to model grounding line migration in general, not to investigate the MISI. Therefore, it will not be discussed which sliding law has strongest physical justification for investigating the MISI.

3 Numerical Methods

Both the FS and SSA equations will be solved using the Finite Element Method (FEM) with Elmer/Ice. In the following sections, the general solution method by deriving the weak formulation is discussed, first for FS and then for SSA. Section 3.3 treats their implementation in Elmer/Ice in more detail. The ISCAL method is discussed in Section 4.1, followed by the SSA-FS coupling in Section 4.2.

3.1 Full Stokes equations

Recall that the final system of equations to be solved for velocity and pressure consists of Equations 1, 6, 7 and 11. The dependence of viscosity on velocity in Equation 7 introduces a non-linearity. The equations need to be solved iteratively by assuming that a certain $\mathbf{u}_k$ is given, from which the viscosity η_k can be computed. With this viscosity a new approximation $\mathbf{u}_{k+1}, p_{k+1}$ can be solved from the linearized system of equations. This method is called *Picard iteration*. The linearized system of equations then becomes:

$$\begin{aligned} 0 &= \nabla \cdot \mathbf{u}_{k+1} \\ \mathbf{0} &= -\nabla p_{k+1} + \nabla \cdot \left(\eta_k(\nabla \mathbf{u}_{k+1} + (\nabla \mathbf{u}_{k+1})^T)\right) + \rho \mathbf{g}. \end{aligned}$$

This linearized system will be solved using the Finite Element Method (FEM), since it is well-suited to solve problems that are defined on complex geometries as is the case for ice sheets. Denoting the domain by Ω and its boundary by $\partial\Omega$, the weak formulation follows from multiplying the equations by test functions $\mathbf{v} \in H_0^1(\Omega)^3, q \in L^2(\Omega)$ and integrating over the entire domain such that

$$\int_\Omega q \nabla \cdot \mathbf{u}_{k+1} d\Omega = 0 \tag{41}$$

$$\int_\Omega \mathbf{v} \cdot \left(\nabla p_{k+1} - \nabla \cdot \left(\eta_k(\nabla \mathbf{u}_{k+1} + (\nabla \mathbf{u}_{k+1})^T)\right)\right) d\Omega = \int_\Omega \mathbf{v} \cdot \rho \mathbf{g} d\Omega. \tag{42}$$

Applying Gauß' theorem and integration by parts of Equation 42, denoting the component-wise scalar product by $\mathbf{x} : \mathbf{y}$, gives

$$\begin{aligned} &\int_\Omega \mathbf{v} \cdot \left(\nabla p_{k+1} - \nabla \cdot \left(\eta_k(\nabla \mathbf{u}_{k+1} + (\nabla \mathbf{u}_{k+1})^T)\right)\right) d\Omega = \\ &- \int_\Omega p_{k+1} \nabla \cdot \mathbf{v} d\Omega + \int_{\partial\Omega} p_{k+1} \mathbf{n} \cdot \mathbf{v} d\Omega + \int_\Omega \left(\eta_k(\nabla \mathbf{u}_{k+1} + (\nabla \mathbf{u}_{k+1})^T)\right) : \nabla \mathbf{v} d\Omega \\ &- \int_{\partial\Omega} \left(\left(\eta_k(\nabla \mathbf{u}_{k+1} + (\nabla \mathbf{u}_{k+1})^T)\right) \cdot \mathbf{n}\right) \cdot \mathbf{v} d\Omega. \end{aligned} \tag{43}$$

Note that the stress free surface assumption and no-slip condition imply that the boundary integrals are zero (natural boundary conditions). For more complex sliding conditions, which are essential and give nonzero boundary integrals, well-posedness for the Stokes problem was proven in Jouvet and Rappaz [2012]. Defining $\mathbf{V} := \{\mathbf{v} \in H_0^1(\Omega)^3 : \mathbf{v}_b = 0\}$, the weak formulation then follows from Equation 41 and 42 by substituting Equation 43. It can be formulated (dropping the linearization subscripts $k, k+1$ for abbreviation) as

follows:

$$\begin{aligned} \text{Find} \quad & \mathbf{u} \in \mathbf{V} \text{ and } p \in L^2(\Omega) \text{ such that} \\ -\int_\Omega p\nabla\cdot\mathbf{v}d\Omega \quad + \quad & \int_\Omega \left(\eta(\nabla\mathbf{u}+(\nabla\mathbf{u})^T)\right):\nabla\mathbf{v}d\Omega = \int_\Omega \rho\mathbf{g}\cdot\mathbf{v}d\Omega,\ \forall\mathbf{v}\in\mathbf{V} \qquad (44) \\ \int_\Omega q\nabla\cdot\mathbf{u}d\Omega \quad = \quad & 0,\ \forall q\in L^2(\Omega). \qquad (45) \end{aligned}$$

The weak formulation given by Equations 44 and 45 can be discretized by finite elements, determining $\mathbf{u}_h, p_h$ in the finite dimensional subspaces $\mathbf{V}_h$ of $\mathbf{V}$ and $\mathbf{Q}_h$ of $L^2(\Omega)$. The discretized Galerkin equations can then be written as a linear system, by approximating $\mathbf{u}_h, p_h, \mathbf{v}_h$ and q_h with basis functions:

$$\mathbf{u}_h = \sum_{j=1}^{n_u} u_j\phi_j, p_h = \sum_{k=1}^{n_p} p_k\psi_k. \qquad (46)$$

The system of equations can then be written in matrix form, denoting the boundary integrals by $\mathbf{f}_h$,

$$\begin{pmatrix} A & B^T \\ B & 0 \end{pmatrix}\begin{pmatrix} \mathbf{u}_h \\ p_h \end{pmatrix} = \begin{pmatrix} \mathbf{f}_h \\ 0 \end{pmatrix}, \qquad (47)$$

where in fact the so-called stiffness matrix given in the left hand side depends on the viscosity η and hence on the velocity $\mathbf{u}$ itself as well. The entries of the matrices are given by

$$A_{ij} = \int_\Omega \eta\left(\nabla\phi_i + (\nabla\phi_i)^T\right):\nabla\phi_j d\Omega, \qquad (48)$$

$$B_{kj} = -\int_\Omega \psi_k\nabla\cdot\phi_j d\Omega, \qquad (49)$$

$$\mathbf{f}_{h,i} = \int_\Omega \rho\mathbf{g}\cdot\phi_i d\Omega. \qquad (50)$$

In practice, the coefficients of the stiffness matrix in Equation 47 are computed by summing over the local element matrices A_{ij}^E:

$$A_{ij} = \sum_E A_{ij}^E, \quad A_{ij}^E = \int_E \eta\left(\nabla\phi_i + (\nabla\phi_i)^T\right):\nabla\phi_j d\Omega. \qquad (51)$$

There is a fixed reference element $\hat{E}$ and integrals over the elements are evaluated through a mapping $f_E : \hat{E} \to E$, depending on the determinant of the Jacobian matrix $|J_E|$ of f_E, such that

$$A_{ij}^E = \int_{\hat{E}} \eta\left(\nabla\phi_i + (\nabla\phi_i)^T\right):\nabla\phi_j|J_E|d\hat{\Omega}. \qquad (52)$$

The integral over the reference element is numerically approximated by Gauss-quadrature:

$$A_{ij}^E = \sum_{k=1}^{N} \eta\left(\nabla\phi_i(\xi_k) + (\nabla\phi_i(\xi_k))^T\right):\nabla\phi_j(\xi_k)w_k|J_E(\xi_k)|. \qquad (53)$$

Assembling the matrix B and vector $\mathbf{f}_h$ is done in the same way and omitted here.

The weak formulation (Eq. 44 and 45) is equivalent to a *saddle-point* problem, which implies that instabilities may occur if the inf-sup condition is not satisfied [Arnold et al.,

1984]. In order to satisfy the inf-sup condition, the spaces $\mathbf{V}_h, \mathbf{Q}_h$ need to be chosen with care. Bercovier and Pironneau [1979] proved that using piecewise quadratic velocities and piecewise linear pressures guarantees convergence. The specific handling of the inf-sup condition in Elmer/Ice is discussed further in Section 3.3.

3.2 Shallow Shelf Approximation

Since the SSA includes spatial derivatives in the velocities, as opposed to SIA which only contains derivatives in surface slope, it is not as straightforward to solve. Therefore, the SSA equations (23,24) will be solved for the flow velocity using FEM as well. Since the equations for SSA do not depend on z, they can be solved for one dimension less than the FS equations which makes them computationally less demanding. A hydrostatic equilibrium is assumed, such that the pressure can be solved directly from $\partial p/\partial z = -\rho g$ and the boundary condition $p = 0$ on the ice surface.

Since boundary conditions differ for the grounded and floating part of the domain, they are denoted separately by Ω_g, Ω_f respectively. Writing $(x, y) = (x_1, x_2), (u, v) = (u_1, u_2)$, the weak form of both shallow shelf equations can be written as

$$\begin{aligned} \text{For} \quad i = 1,2 \quad & \text{find } u_i \in H_0^1(\Omega)^1 \text{ such that} \\ \int_\Omega \quad & \left(\frac{\partial}{\partial x_i} \left(4H\bar{\eta} \frac{\partial u_i}{\partial x_i} + 2H\bar{\eta} \frac{\partial u_j}{\partial x_j} \right) + \frac{\partial}{\partial x_j} \left(H\bar{\eta} \frac{\partial u_i}{\partial x_j} + H\bar{\eta} \frac{\partial u_j}{\partial x_i} \right) \right) \phi d\Omega = \\ \int_\Omega \quad & \rho g \frac{\partial z_s}{\partial x_i} \phi d\Omega - \int_{\Omega_g} \tau_i \phi d\Omega, \forall \phi \in H_0^1(\Omega)^1. \end{aligned} \tag{54}$$

Since the final goal is to couple the SSA solution to the FS solution, conditions for coupling need to be considered. It is clear that coupling is only possible if the FS pressure is almost hydrostatic and vertical gradients of u_{FS}, v_{FS} are negligible. It is questionable whether ice streams exhibit the vertically uniform behaviour as modeled with SSA. Such an ice stream would need to be very wide in order not to be affected by stresses in the shear margin where the ice stream meets surrounding slow moving ice. At first, the SSA will therefore only be applied at the ice shelves. Therefore, from now on it will be assumed that the whole domain Ω_{SSA} where SSA is applied is part of an ice shelf. This implies $\tau_b = 0$ and the floatation criterion by Archimedes' principle allows the surface elevation z_s to be written in terms of the thickness H as in Equation 30. Introducing $\varrho = \rho(1 - \rho/\rho_w)$, the floatation criterion gives $\varrho g H \frac{\partial H}{\partial x_i} = \frac{\partial}{\partial x_i} \left(\frac{\varrho}{2} g H^2 \right)$. Defining

$$M = \bar{\eta} H \begin{pmatrix} 4\frac{\partial u}{\partial x} + 2\frac{\partial v}{\partial y} & \frac{\partial u}{\partial y} + \frac{\partial v}{\partial x} \\ \frac{\partial u}{\partial y} + \frac{\partial v}{\partial x} & 2\frac{\partial u}{\partial x} + 4\frac{\partial v}{\partial y} \end{pmatrix} = \begin{pmatrix} M_{11} & M_{12} \\ M_{21} & M_{22} \end{pmatrix}, \tag{55}$$

the weak form of the SSA equations for the shelf can be reformulated as

$$\begin{aligned} \text{for} \quad i = 1,2 \quad & \text{find } u_i \in H_0^1(\Omega)^1 \text{ such that} \\ & \int_\Omega \left(\frac{\partial M_{ij}}{\partial x_j} - \frac{\partial}{\partial x_j} \left(\frac{\varrho}{2} g H^2 \right) \right) \phi d\Omega = 0, \forall \phi \in H_0^1(\Omega)^1, \end{aligned} \tag{56}$$

using Einsteins summation convention[3] and the symmetry of M. Applying the two-dimensional version of the divergence theorem and integration by parts gives

$$\int_\Omega \left(\frac{\partial M_{ij}}{\partial x_j} - \frac{\partial}{\partial x_j} \left(\frac{\varrho}{2} g H^2 \right) \right) \phi d\Omega =$$
$$\int_{\partial\Omega} \left(M_{ij} - \frac{\varrho}{2} g H^2 \right) \phi n_j d\Omega - \int_\Omega \left(M_{ij} - \frac{\varrho}{2} g H^2 \right) \frac{\partial \phi}{\partial x_j} d\Omega. \tag{57}$$

Therefore, the integral in the weak form can be written in terms of first order derivatives (noting that M includes derivatives) as

$$\int_\Omega \left(M_{ij} - \frac{\varrho}{2} g H^2 \right) \frac{\partial \phi}{\partial x_j} d\Omega = \int_{\partial\Omega} \left(M_{ij} - \frac{\varrho}{2} g H^2 \right) \phi n_j d\Omega. \tag{58}$$

The boundary condition at the calving front is natural, such that the boundary integral becomes zero there. The boundary condition at the grounding line (or in this case at the position where it is coupled to the FS solution) is essential and needs to be included.

Like the FS equations, the SSA equations are in fact non-linear since M depends on the viscosity which in turn is coupled to the flow velocity through the effective strain rate D (Eq. 6). However, it is sufficient to only know the horizontal SSA velocities in order to approximate the vertically integrated effective strain rate[4] since $\frac{\partial u}{\partial z}, \frac{\partial v}{\partial z} = 0$, such that

$$\overline{D(\mathbf{u})} \approx \frac{1}{\sqrt{2}} \sqrt{ \left(\frac{\partial u}{\partial x} \right)^2 + \left(\frac{\partial v}{\partial y} \right)^2 + \left(\frac{\partial w}{\partial z} \right)^2 + \frac{1}{2} \left(\frac{\partial u}{\partial y} + \frac{\partial v}{\partial x} \right)^2 } \tag{59}$$

where $\frac{\partial w}{\partial z} = -\frac{\partial u}{\partial x} - \frac{\partial v}{\partial y}$ is derived from the incompressibility condition and $\partial w/\partial x, \partial w/\partial y$ are neglected, which is justified by the same dimensional analysis that leads to the SSA equations [Greve and Blatter, 2009].

Once u, v are calculated, w, p can be calculated respectively from incompressibility and hydrostatic pressure (Eq. 22, 17). The incompressibility only yields $\frac{\partial w}{\partial z}$, however the integration constant can be computed from the floatation condition for hydrostatic equilibrium, thickness Equation 29 and the kinematic boundary condition at the base given by Equation 27. Floatation yields

$$z_s = (1 - \rho/\rho_w) H = z_b + H \Rightarrow \frac{\partial z_b}{\partial x} = -\frac{\rho}{\rho_w} \frac{\partial H}{\partial x}, \tag{60}$$

such that

$$\frac{\partial z_b}{\partial x} u + \frac{\partial z_b}{\partial y} v = -\frac{\rho}{\rho_w} \left(\frac{\partial H}{\partial x} u + \frac{\partial H}{\partial y} v \right) \tag{61}$$

and by Equation 29, using that $q_x = Hu$ for the SSA solution, denoting $\nabla_h \mathbf{u} = \frac{\partial u}{\partial x} + \frac{\partial v}{\partial y}$,

$$\frac{\partial H}{\partial x} u + \frac{\partial H}{\partial y} v = a_s + a_b - \frac{\partial H}{\partial t} - H \nabla_h \mathbf{u}. \tag{62}$$

[3] $\frac{\partial M_{ij}}{\partial x_j} = \frac{\partial M_{11}}{\partial x_1} + \frac{\partial M_{12}}{\partial x_2}$

[4] Isothermality gives $\overline{A(T)} = A$, such that it does not need to be recomputed under the current assumptions.

The boundary condition for w at the base can then be written as

$$\begin{aligned} w_b &= a_b - \left(\frac{\partial z_b}{\partial x}u + \frac{\partial z_b}{\partial y}v\right) - \frac{\partial z_b}{\partial t} \\ &= a_b + \frac{\rho}{\rho_w}\left(\frac{\partial H}{\partial x}u + \frac{\partial H}{\partial y}v\right) - \frac{\partial z_b}{\partial t} \\ &= a_b + \frac{\rho}{\rho_w}\left(a_s + a_b - \frac{\partial H}{\partial t} - H\nabla_h \mathbf{u}\right) + \frac{\rho}{\rho_w}\frac{\partial H}{\partial t} \\ &= a_b + \frac{\rho}{\rho_w}\left(a_s + a_b - H\nabla_h \mathbf{u}\right). \end{aligned} \tag{63}$$

Finally, substituting the basal vertical velocity into Equation 25 yields, once more applying the floatation criterion,

$$\begin{aligned} w(z) &= (z - z_b)\nabla_h \mathbf{u} + a_b + \frac{\rho}{\rho_w}\left(a_s + a_b - H\nabla_h \mathbf{u}\right) \\ &= z\nabla_h \mathbf{u} + a_b + \frac{\rho}{\rho_w}\left(a_s + a_b - 2H\nabla_h \mathbf{u}\right). \end{aligned} \tag{64}$$

3.3 Elmer/Ice

The Finite Element Method (FEM) solving the FS and SSA equations will be carried out using the community ice sheet model Elmer/Ice. Elmer/Ice is the glaciological extension of Elmer, the open source Finite Element software developed by CSC-IT[5]. Elmer/Ice was not originally designed as an ice sheet model (the first applications were restricted to glaciers [Le Meur et al., 2004]) but has by now been applied to the entire Greenland Ice Sheet [Gillet-Chaulet et al., 2012]. In 2013, Elmer/Ice was the only three dimensional FS model that solved the contact problem at the grounding line [Favier et al., 2012]. Many of the simplifying assumptions made in this project are not necessary for modeling ice sheet dynamics in Elmer/Ice. For example the temperature distribution in an ice sheet can be modeled, but also two anisotropic rheology laws are implemented [Gagliardini et al., 2013]. This shows the strength of Elmer/Ice, it is an important model for the glaciological community and therefore many will benefit from improvements within Elmer/Ice.

The most commonly used solver in Elmer for solving the FS equations is the FlowSolver[6]. The ISCAL method is also coded based on the FlowSolver, such that the FS part of the domain is solved by the FlowSolver. Systems of non-linear equations can be solved in Elmer using Newton or Picard iteration. In this project, only Picard iteration will be applied. When a convergence tolerance of Picard iteration is mentioned, this will always refer to the normalized difference between two subsequent Picard iterations. The singular nature of the viscosity η for small stresses at the surface does not introduce singularities in the field variables when solving the FS equations, since normal stresses are not neglected and will develop resulting in a non-zero effective strain rate D at the surface (Eq. 6). However, the simple power law for rheology as in Glen's law in Equation 7 has a singularity if the

[5] See `http://www.csc.fi/elmer/`

[6] See `https://github.com/ElmerCSC/elmerfem/blob/devel/fem/src/modules/FlowSolve.F90`

effective strain rate $D = 0$, since commonly $n > 1$ is assumed, which causes numerical difficulties for low strain rates. This is avoided in Elmer/Ice by introducing an extra parameter called the *critical shear rate* $\dot{\gamma}_0$ which is set as a lower bound to the strain rate $\dot{\gamma} = 2D$. Care needs to be taken in choosing the value of the critical shear rate. A too high value leads to too soft ice at low shear rates, a too low value can have consequences on the numerical stability. A commonly used value is $\dot{\gamma}_0 = 10^{-10}$, which will be applied here as well.

Employing a higher order element for velocity than for pressure leads to a stable solution of the FS equations (shown by Isaac et al. [2015] and Ainsworth and Coggins [2000]). Having quadratic elements for velocity and linear for pressure (called P2P1 from now on) is implemented in Elmer [Råback et al., 2016a], but most meshes used for glaciological models are extruded from footprint of one dimension less, which due to technical issues does not allow for P2P1 stabilization as currently implemented in Elmer. Stabilization to avoid spurious oscillations is instead done by the Galerkin Least-Squares (GLS) method [Franca and Frey, 1992] or by using the MINI element (also called residual free bubbles method, [Arnold et al., 1984]). Both methods are explained in the next paragraph. More details on the Elmer software can be found in Råback et al. [2016a].

3.3.1 Stabilization

The GLS stabilization method adds extra terms to the discretized weak form of the Stokes equations, which vanish for the true solution [Hughes and Franca, 1987]. The terms added to the stiffness matrix are proportional to a parameter called the stabilization parameter

$$\tau_{GLS} = \frac{m_K h_k^2}{8\eta}, \tag{65}$$

where $m_K = 1/3$ for linear interpolations and h_K is a locally varying element measure. Besides that, the viscosity η is also spatially varying and the dependence of the stabilization parameter on viscosity introduces an additional coupling between pressure and velocity. In Elmer/Ice, h_K is taken to be the minimum edge length which can be problematic with the flat elements usually employed in ice sheet modeling. As an example, in a hundred year long simulation of Greenland, horizontal edge size varied from 40km to refinements of 1km and the vertical direction was divided in 16 layers [Gillet-Chaulet et al., 2012], hence the vertical element size is up to 200m for a maximum ice thickness of about 3000m. This means that the aspect ratio of elements can easily get up to 1/200, affecting both accuracy and stability. This is a known limiting factor of accuracy in the FS solution for ice sheets with Elmer/Ice. For example Seddik et al. [2012] (also modeling Greenland) state that the vertical resolution could not be increased since the aspect ratio of the elements lead to numerical instabilities. More experiments regarding stabilization in Elmer/Ice are done by Helanow and Ahlkrona [2017], where results are compared to another FS model using the FEM software FEniCS. They find that effectiveness of the stabilization method highly depends on h_K, but the most suitable definition of h_K is problem dependent. In particular the vertical velocity is prone to instabilities, which will affect the stability of the surface

evolution if modeled by the free surface Equations 26 and 27.

Another possible stabilization technique follows from applying MINI elements, including internal degrees of freedom in each element in the velocity space, so called bubble shape functions to which the method owes its alternative name 'residual free bubbles method' [Arnold et al., 1984]. The added internal degrees of freedom increase the size of the linear system to be solved in each non-linear iteration of the FlowSolver. The ISMIP-HOM (Ice Sheet Model Intercomparison Project - Higher-Order ice sheet Model) benchmark tests have been performed using both the GLS and residual free bubbles method for stabilization [Gagliardini and Zwinger, 2008]. Although the size of the linear system to be solved when using GLS is half the size of the linear system for the residual free bubbles method, it may not be more efficient since Gagliardini and Zwinger [2008] showed that the number of elements needs to be increased in order to maintain an accurate solution by the GLS method. In this project, the GLS method is applied in the experiments using ISCAL, in accordance to Ahlkrona et al. [2016] and the residual free bubbles method is applied to the MISMIP-like experiments as was done in Pattyn et al. [2012] and Gladstone et al. [2017]. Note that the SSA equations are solved over the horizontal only (see Equation 24 and 23), such that no elements with high aspect ratio need to be employed. Therefore, solving SSA is expected to be more stable.

3.3.2 Time evolution

The evolution of ice thickness is described by Equations 26, 27 and 29. The time step Δt for time integration needs to be chosen with care to for accuracy and stability. Several one-step schemes have been analyzed for stability in Hindmarsh [2001]. By Fourier analysis of the linearized equations, restrictions on Δt are derived of the form $\Delta t \leq C\Delta x^2$, where Δx comes from the spatial discretization. In Elmer/Ice, first order time derivatives may be discretized by two different methods: the Crank-Nicolson method or the Backward Differences Formulae (BDF) of several orders. First order BDF, better known as Backward Euler, is applied here. This method in itself is implicit and thus stable. However, it is only applied to the time dependent equations after the velocities have been computed and as explained in Cheng et al. [2017], the coupled system of the FS equations and the surface evolution is therefore not fully implicit. A fully implicit method that is unconditionally stable would allow larger Δt, but this would require several iterations of solving the non-linear FS equations and subsequently updating the geometry during each time step. Since this would increase the computation time per time step, instead the described semi implicit method is chosen. In Cheng et al. [2017], an adaptive time stepping method is introduced in Elmer/Ice which lets Δt vary over the total simulation by estimating the error from the time discretisation, such that there is no need to guess a stable time discretization for the whole interval. However, in order to allow comparison of computation time of the coupled and FS models, values for Δt will be constant throughout each experiment here.

4 Coupled models

4.1 ISCAL: Coupling FS and SIA

Modeling of ice sheets over paleo time spans requires approximating the FS equations since these are too expensive to compute even on supercomputers. Even though the often used SIA is valid for a large interior part of ice sheets, it is not possible to *a priori* define this region. This shows the need for a model which combines SIA where possible, but solves the FS equations where necessary. Therefore a new method is proposed in Ahlkrona et al. [2016], which dynamically couples the FS equations with the SIA. In short it works as follows. First, the SIA equations are solved directly starting from initial conditions on the ice sheet geometry for the first time step t_0 in the whole domain Ω. The gradients in Equation 20 are computed using implemented solvers of Elmer/Ice. Since all meshes will be constructed such that the nodes are aligned in the vertical direction, the integrals in Equation 20 can be computed using the trapezoidal rule.

The error in the resulting velocities $\mathbf{u}_{SIA}(t_0)$ and pressure $p_{SIA}(t_0)$ calculated by the SIA model are estimated by comparing them with the FS solution which is calculated by once solving the full non-linear system[7] $A_{FS}(u_{FS}^{n-1})\mathbf{u}_{FS}^{n} = \mathbf{b}$. The total domain Ω is then divided into two subdomains Ω_{FS} and Ω_{SIA}. A node is defined to belong to Ω_{FS} if the estimated error in the SIA solution $||\mathbf{u}_{FS} - \mathbf{u}_{SIA}||$ is larger than a certain user defined absolute *and* relative error. On the interface of the domains, $\mathbf{u}_{SIA}^{\Omega_{SIA}} = (u, v, w, p)_{SIA}^{\Omega_{SIA}}$ is applied as a Dirichlet boundary condition to the FS domain. It should be noted that Ladyzhenskaya and Silverman [1969] proved that no explicit boundary conditions for the pressure should be given for incompressible flow, hence this may cause problems in the ISCAL method.

The one-way coupling of using SIA as boundary condition to the FS domain is reasonable because the SIA does not contain (neither horizontal nor vertical) spatial derivatives of the velocities, which implies that there will not be any interaction with the FS velocity. By numerically solving the thickness Equation 29, the ice surface is updated every time step, thus also the region where the scaling relations fundamental to SIA hold, will change over time. For this reason, the FS and SIA domain are redetermined after a user defined number of time steps m. This requires a new estimation of the error of $\mathbf{u}_{SIA}$. In order to do so, a reference solution $\mathbf{u}_{REF}$ is obtained by solving the linear system $A(\mathbf{u}_{ISCAL})\mathbf{u}_{REF} = \mathbf{b}$ for the entire domain, after finding the ISCAL solution by combining SIA and FS, but before updating the ice surface using the thickness equation. Then the SIA error is again approximated by

$$\mathbf{u}_{FS} - \mathbf{u}_{SIA} \approx \mathbf{u}_{REF} - \mathbf{u}_{SIA}, \tag{66}$$

[7] Setting "`SIA node = Real -1.0`" in the Materials section of the solver input file, uses $A_{FS}(u_{SIA})$ instead, calculating the viscosity from $\mathbf{u}_{SIA}$ and hence reducing the computation time in the first time step but also increasing the risk of inaccurate error estimation.

which has been shown in Ahlkrona et al. [2016] to be an accurate estimate only if FS and ISCAL are not very far apart. This shows that the parameter m needs to be chosen with care. An option to increase both accuracy and efficiency of the ISCAL method is to make also the determination of the parameter m dynamical, depending on the amount of change in the solution $\mathbf{u}_{ISCAL}$ between two time steps. Based on the new error estimation in Eq. 66, the domain is divided into $\Omega_{FS}, \Omega_{SSA}$ for the next m time steps.

As noted in Ahlkrona et al. [2016], assembling the stiffness matrix of the FS equations dominates the CPU-time required for the simulations, even though the portion of time needed for solving the FS equations increases with problem size. Since the matrix that needs to be assembled in ISCAL is smaller ($\Omega_{FS} \subset \Omega$) less CPU-time is needed even though solving the linearized FS equations themselves do not dominate CPU-time.

4.2 Coupling FS and SSA

In developing a coupling between FS and SSA, it is instructive compare to the nature of the SSA equations to the SIA equations such that also possible coupling methods can be compared. Since lateral shear is neglected by SIA, its solution for the stresses and horizontal velocities only depend on the *local ice geometry* (see Equation 20). This allows for solving SIA only for a part of the domain, without the need of knowing the velocity in the rest of the domain. In contrast, for the SSA equations the velocities are coupled in the horizontal plane. Therefore, in a possible splitting of the domain $\Omega := \Omega_{FS} \cup \Omega_{SSA}$, the FS and SSA velocities are more closely interlinked and it is impossible to first solve for only one system of equations and use this as input for the other approximation level. Instead, the velocities need to be solved simultaneously, ideally in one system that combines the stiffness matrices A_{FS} and A_{SSA}. Although the coupling of the two matrices is, in theory, only a matter of bookkeeping and connecting the nodes at the coupling interface, this coupled matrix may unfortunately be hard to solve since the currently used algebraic preconditioners (ILU) are inappropriate for such a special matrix structure where one part describes four degrees of freedom and the other part two. Therefore, implementing the coupling by a combined matrix would require implementation of problem specific preconditioners which is an unnecessary time consuming exercise if a looser degree of coupling is also found to be sufficiently accurate and robust, compared to the error already made by applying a lower order approximation level. Thus, an iterative coupling in form of domain decomposition is implemented here, where the FS and SSA equations are solved iteratively for every time step. A schematic overview of the iterative coupling is given in Figure 5 and the individual steps are discussed in more detail below.

The main difference between the FS and SSA equations is that in SSA, the horizontal velocities do not vary along the vertical axis. Therefore, in order to make a coupling possible, the solution of the FS equations near the coupling interface also needs to be homogeneous along the vertical. Let $(x_c, y_c) = \mathbf{x}_c$ denote the line or surface of coupling (one

dimension lower than the model domain). This coupling interface is initially defined at a user defined minimum distance from the grounding line (d_{GL}, see *initialize* in Figure 5). This distance should be chosen such that indeed $\frac{\partial u_{FS}}{\partial z}, \frac{\partial v_{FS}}{\partial z}(\mathbf{x}_c) < \epsilon$ for a chosen tolerance ϵ. Both FS and SSA equations are solved already using FEM in Elmer/Ice, such that only the coupling itself remains to be implemented.

The flow velocity of ice shelves is greatly influenced by the inflow velocity, in some conceptual 2D cases an analytical solution can even be calculated for the velocity in the entire shelf if the inflow velocity is given [Greve and Blatter, 2009]. The necessity of knowing the inflow velocity for solving SSA suggests that an iterative combination of the two approximation levels should start with solving the FS equations for Ω_{FS}, such that an approximate inflow velocity u_{FS}, v_{FS} can be applied as a Dirichlet boundary condition at $\mathbf{x}_c$ to the SSA equations. A boundary condition will be necessary at $\mathbf{x}_c$ for Ω_{FS} as well. Since the shelf itself continues beyond the coupling location, the first iteration of the coupled model assumes that the force acting on the FS domain at the coupling interface is similar to the cryostatic pressure (Eq. 17). This will overestimate the force however, since the ice shelf is actually moving with the flow, it is not a static block of ice buttressing the flow. Therefore, the force has to be adjusted based on the ice flow as calculated for the SSA domain. This will be done by calculating the *contact force* denoted by $\mathbf{f}_{SSA}$. For an exact solution of $Ax = b$, its residual $f = Ax - b$ should be zero. However, if we regard A as being the stiffness matrix which has not undergone the setting of Dirichlet boundary conditions yet, the residual is equal to the contact force induced by prescribing a value for this variable [Durand et al., 2009a]. In case of the SSA equations (Eq. 23 and 24), which are vertically integrated over the shelf, this contact force is the vertically integrated force which needs to be scaled by the thickness H. In two dimensions the contact force f_{SSA} has one degree of freedom (just as u_{SSA}). In essence, the coupling in three dimensions is equivalent to the two dimensional version, except the contact force consists of two components. Besides that, the force $\mathbf{f}_{SSA}$ needs to be weighted for the horizontal scale of the coupling interface as well[8], such that the total boundary condition applied to Ω_{FS} at the coupling interface comprises of a normal pressure being the cryostatic pressure p_{cryo} and two components in respectively the x, y direction being $\frac{f_i}{wH}$. The use of contact forces instead of explicitly calculating the stress is advantageous since it is extremely cheap to find the contact force if the original stiffness matrix A is stored.

To summarize, the FS and SSA velocities are computed separately within an iteration of the coupled model, with the following boundary conditions at the coupling interface. For FS, an external pressure

$$\boldsymbol{\sigma} \cdot \vec{n}|_{FS}(\mathbf{x}_c, z) = \rho g(z - z_s) + \frac{\mathbf{f}_{SSA}(\mathbf{x}_c)}{wH} \tag{67}$$

[8]In case of a coupling interface $\mathbf{x}_c$ aligned with the y axis, for a grid that is equidistant along y, $w = \Delta y$ for internal nodes and $w = \Delta y/2$ for nodes where the coupling interface intersects the lateral boundaries.

is applied. For SSA, a Dirichlet inflow boundary condition

$$u_{SSA}(\mathbf{x}_c) = u_{FS}(\mathbf{x}_c, z_b), \quad v_{SSA}(\mathbf{x}_c) = v_{FS}(\mathbf{x}_c, z_b) \tag{68}$$

provides the coupling to the FS solution. In the boundary conditions at the coupling interface, $\mathbf{f}_{SSA}$ and $\mathbf{u}_{FS}$ are updated until the relative change in $\mathbf{u}_{FS}$ and $\mathbf{u}_{SSA}$ are below a convergence tolerance ϵ_c. Solving $\mathbf{u}_{FS}$ and $\mathbf{u}_{SSA}$ with their respective boundary conditions are numbered step 1 and 2 in Figure 5.

The number of coupled iterations is influenced by the initial condition for $\mathbf{u}_{FS}, \mathbf{u}_{SSA}$ and $\mathbf{f}_{SSA}$. At $t = 0$, all are initially zero, but at later time steps, initial velocities and contact forces are taken from the previous time step. Besides the iteration for coupling FS and SSA, the solutions $\mathbf{u}_{FS}$ and $\mathbf{u}_{SSA}$ itself are calculated iteratively since they follow from a non-linear system of equations. The convergence tolerance for the non-linear equations is denoted by ϵ_{NL}. Note that it is assumed here that the linearized systems are solved directly. In case the linear system is solved iteratively, its convergence tolerance should be smaller than all other tolerances used ($\epsilon_L \leq \epsilon_{NL}, \epsilon_c$). The maximum number of non-linear iterations can be tuned for efficiency, since it may increase convergence speed to update the contact force $\mathbf{f}_{SSA}$ more frequently, before the Picard iteration for the non-linearity in $\mathbf{u}_{FS}$ and/or $\mathbf{u}_{SSA}$ has reached the converge tolerance ϵ_{NL}. In that case, the number of coupled iterations will be larger in order to meet convergence up to ϵ_c, but the total number of FS iterations (which is mainly determining computation time) over all coupled iterations together may be lower. This will be investigated in Section 5.3.2.

Once the coupling of $\mathbf{u}_{FS}$ and (u_{SSA}, v_{SSA}) has converged, the vertical SSA velocity can be calculated from the incompressibility condition. Together with the hydrostatic pressure in Ω_{SSA}, the FS and SSA solutions can be glued to find the coupled solution $\mathbf{u}_c = (\mathbf{u}_{FS}, \mathbf{u}_{SSA})$ (Step 3 in Figure 5).

4.2.1 Surface evolution of the coupled model

Although a theoretical boundary condition for the vertical SSA velocity was derived (Eq. 64), this w_{SSA} is not based on the same assumptions as w_{FS}. The surface accumulation is not taken into account when solving for w_{FS}, but instead the bulk velocity is first calculated for the current geometry assuming a buoyancy force exerted by the ocean water on the ice shelf base and subsequently the surface accumulation is used by the Free Surface solvers to adjust the surface elevation. The Neumann boundary condition provided by this buoyancy force only defines the gradients of the vertical velocity, but since the vertical FS velocity is known to be zero where in contact with the rigid bedrock on the grounded part, the vertical FS velocity can also be derived for the shelf through the horizontal gradients. The SSA model on the contrary neglects all horizontal gradients of the vertical velocity, hence it is impossible to define the actual value of the SSA vertical velocity from a Neumann boundary condition. However, to solve the thickness advection equation, it

is not necessary to know the vertical velocity in order to find the surface evolution since it is anyhow assumed that the entire SSA domain Ω_{SSA} satisfies the floatation criterion. Therefore, the surface evolution (Step 4 in Figure 5) will be calculated differently in the two domains, using the two free surface equations (26 and 27) for Ω_{FS} and the thickness advection equation (29) for Ω_{SSA}, shown in Figure 4. This implies that at the coupling interface x_c, the surface elevations need to satisfy the floatation criterion (Eq. 30) in order to guarantee a continuous geometry. Therefore, the domain Ω_{SSA} needs to evolve in time as the geometry changes, which will be discussed in the next section. The coupling of the two different methods for surface evolution in the FS and SSA domain is tested by the prognostic experiments in Section 5.3.2.

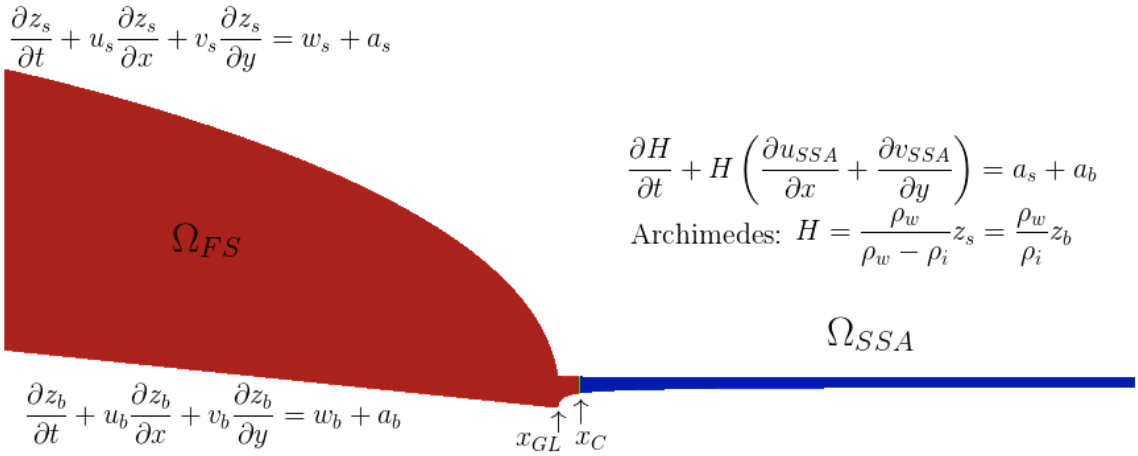

Figure 4: Overview of the equations involved in the surface evolution for the coupled model in three dimensions, where $(u, v, w)_s, (u, v, w)_b$ are respectively surface and basal FS velocities. The upper and lower surface elevation are denoted z_s, z_b, accumulation a_s, a_b and ice thickness H.

4.2.2 Redefinition of Ω_{SSA}

Three methods for redefining Ω_{SSA} are proposed here. The most straightforward way of defining Ω_{SSA} is by setting a minimum distance to the grounding line position, such that Ω_{SSA} is updated every time the grounding line moves. Another possibility, on top of the initial definition of Ω by geometry only, is to update the domain decomposition every m time steps according to an estimation of the validity of SSA. After calculating the viscosity for the coupled velocity $\mathbf{u}_c$, the FS stiffness matrix A_{FS} can be assembled for the entire domain based on this coupled viscosity. Note that even though the actual value of the vertical velocity on the shelf may not be well defined in accordance to the vertical FS velocity, the flow regime on the shelf is such that all components of the viscosity except for $\frac{\partial u}{\partial x}$ and $\frac{\partial w}{\partial z}$ are negligible (in order for SSA to be valid), such that the viscosity can still be calculated. However, since the value of the vertical velocity on the shelf is not consistent with the vertical velocity in Ω_{FS}, the residual $A_{FS}(\mathbf{u}_c)\mathbf{u}_c - \mathbf{b}$ is not a valid measure of the

error. Nevertheless, the assembly of A_{FS} is dominating the solution time in Elmer/Ice[9], so solving for a reference solution u_{ref} such that $A_{FS}(\mathbf{u}_c)\mathbf{u}_{ref} = \mathbf{b}$ is not significantly increasing computation time compared to evaluating the residual only. Similar to ISCAL, a second possible definition of Ω_{SSA} is to require that $\mathbf{u}_{ref}$ has a certain maximum relative or absolute difference with respect to the coupled solution $\mathbf{u}_c$. Then, a point $\mathbf{x}$ belongs to Ω_{SSA} if it holds that

$$E_a := ||\mathbf{u}_{ref} - \mathbf{u}_c|| \leq \epsilon_a \text{ or } E_r := ||\mathbf{u}_{ref} - \mathbf{u}_c||/||\mathbf{u}_{ref}|| \leq \epsilon_r. \tag{69}$$

A third possible definition of the domain Ω_{SSA} is to require that the relative vertical variations of the horizontal velocities, are below a certain coupling tolerance ϵ_{SSA},

$$e := \left(\left| \frac{\partial u_{ref}}{\partial z} \frac{1}{u_{ref}} \right|, \left| \frac{\partial v_{ref}}{\partial z} \frac{1}{v_{ref}} \right| \right) \leq \epsilon_{SSA}. \tag{70}$$

These three different criteria; grounding line distance, error with respect to a reference solution and vertical gradients of the reference solution, will be assessed in the two dimensional diagnostic experiments (Section 5.3.1). Then, the most suitable criterion for defining Ω_{SSA} is applied in the transient simulations.

After redefinition of the domains (Step 5 in Figure 5), other Elmer/Ice solvers can be executed before continuing to the next time step. The flow chart in Figure 5 only shows one time step, but when continuing with the next time step the iterative coupling is performed likewise except for re-using the velocities and contact force calculated in the previous time step as initial guess to accelerate convergence of the iterations.

[9] As stated by Ahlkrona et al. [2016], however experiments here will show that for three dimensional problems solution time may be dominating when solving the linearized system directly.

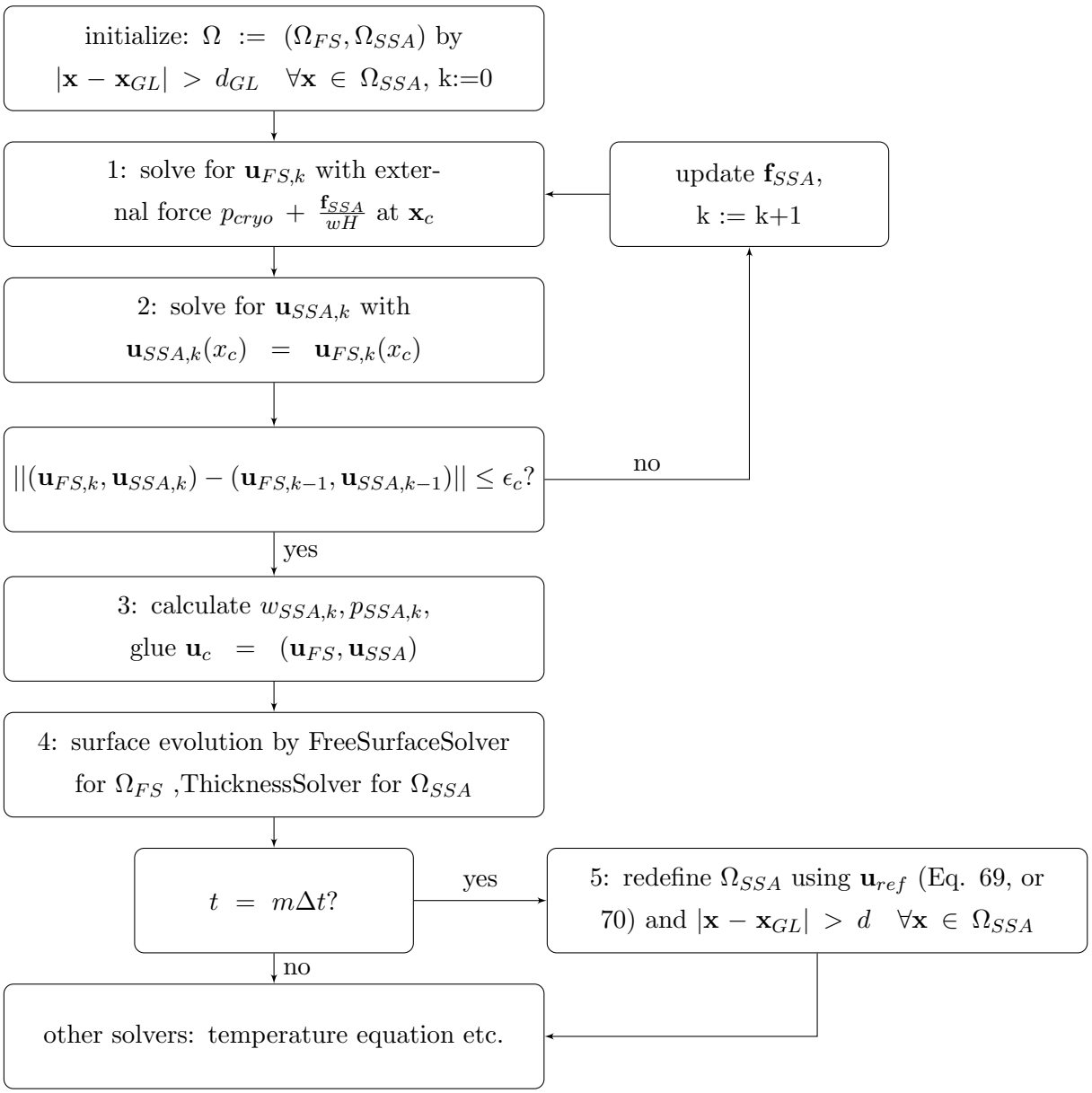

Figure 5: Flowchart of SSA coupling, showing the iterative coupling for $\mathbf{u}_c$ and definition of Ω_{SSA} within one time step, with redefinition of Ω_{SSA} every m timesteps. Note that the SSA weights $w = 1$ in the two dimensional case. Variables $\mathbf{u}_{FS}, \mathbf{u}_{SSA}, \mathbf{f}_{SSA}$ in initialize are taken from the previous time step, at $t = 0$ all are initially zero. Also $\Omega := (\Omega_{FS}, \Omega_{SSA})$ comes from the previous time step, with the extra constraint that $|\mathbf{x} - \mathbf{x}_{GL}| > d_{GL} \ \forall \mathbf{x} \in \Omega_{SSA}$ in case the grounding line migrated.

.

5 Experiments and results

In order to ensure that the model results can be validated, the coupled approximation levels should be applied to geometries for which the FS model in Elmer/Ice itself has performed successfully such that it can serve as a reference. Therefore, ISCAL is applied to geometries similar to the ones in Ahlkrona et al. [2016] and the coupling of SSA and FS is restricted to the experiments as described in [Greve and Blatter, 2009], Pattyn et al. [2012] and Gladstone et al. [2017]. Stabilization in these experiments is done as in the original experiments, hence applying the GLS method to the experiments with ISCAL and the residual free bubbles method to both marine ice sheet experiments. Note that the vertical scale is exaggerated 100 times in all figures that show model domains.

Experiments and results for two conceptual three dimensional geometries, called the Vialov and the Bueler profile, in order to assess ISCAL's accuracy for the first research question are described in Section 5.1. Speed up by using ISCAL instead of FS has been shown in Ahlkrona et al. [2016], therefore ISCAL will only be tested for robustness here and not for efficiency.

Thereafter, the ice flow computed by the FS and SSA models in Elmer/Ice are compared in Section 5.2 for a simplified two dimensional cross-section of an ice shelf in order to investigate the possibility of coupling the two models. The coupled model is applied to the same simplified ice shelf, in both two and three dimensions (Section 5.3.1.1 and 5.3.3) in order to answer the second research question.

The third research question is investigated by means of two conceptual marine ice sheets cross-sections, similar to the ones in Pattyn et al. [2012] and Gladstone et al. [2017], modeled with the SSA - FS coupling in Sections 5.3.1.2 - 5.3.2.2. The criteria for defining Ω_{SSA} as suggested in Section 4.2.2 are examined for both marine ice sheets in the diagnostic runs (only solving for the velocity field of the initial geometry without surface evolution). Efficiency of the coupling of FS and SSA will be addressed for the transient runs by comparing computation time of the coupled model with respect to different tolerances for convergence of the iterations in the model (Figure 5).

5.1 ISCAL: Coupling FS and SIA

This section describes experiments with ISCAL, in order to assess its robustness on longer time spans. In all experiments, the standard approach to construct a three dimensional mesh is to first create a two dimensional footprint mesh using triangles or quadrilaterals and then extrude this along the vertical axis into a three dimensional mesh such that the SIA solution, which requires integration over the vertical, can be computed efficiently. The mesh consists of twenty layers in the vertical unless stated otherwise. The ice surface evolves with Equation 26 over time and the mesh therefore shifts in the vertical. The

experiments show some of the difficulties of both solving the FS equations in Elmer/Ice in general and more specifically in ISCAL.

5.1.1 Vialov profile

The 3D circular ice sheet as defined in the EISMINT benchmark experiment (Figure 6) has been simulated in Ahlkrona et al. [2016]. As a starting point and first check of the method, this experiment is reproduced here. In this set up, the bed is assumed to be flat, the initial height h [m] follows the Vialov profile and accumulation rate a [m yr^{-1}] is given by:

$$h(x, y, t = 0) = h_0(1 - (\sqrt{x^2 + y^2}/L)^{(n+1)/n})^{n/(2n+2)}, \quad (71)$$

$$a(x, y) = \min[0.5, 10^{-5}(450 \cdot 10^3 - \sqrt{x^2 + y^2})], \quad (72)$$

where $n = 3, h_0 = 3575.1$ m, $L = 750$ km.

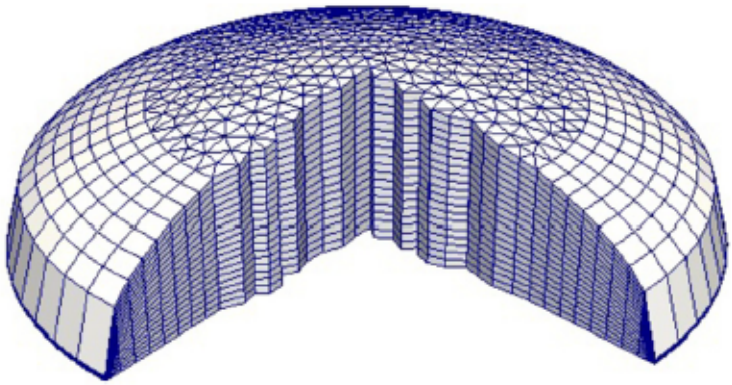

Figure 6: The mesh from extruding a 2D footprint which is unstructured in the center and structured at the margins, as in Ahlkrona et al. [2016].

A derivation of the Vialov profile as steady state of an ice sheet under the SIA can be found in Greve and Blatter [2009]. However, the height profile is derived to match a constant accumulation rate of 0.3 m yr^{-1}, and inducing a theoretical volume flux of $2.25 \cdot 10^5$ m^2 yr^{-1} at the margin, which can be interpreted as the calving rate into a surrounding ocean. Since a different accumulation pattern is assumed here, there is a mismatch between the velocity profile induced by the shape of the ice sheet and the accumulation rates which makes that the ice sheet is not close to steady state. The accumulation rate applied here (Eq. 72) mimics observed accumulation patterns with a positive accumulation rate (0.5 m yr^{-1}) in the center, radially decreasing to a negative accumulation (-3 m yr^{-1} hence ablation) at a radius of 750 km from the center. This follows the original EISMINT benchmark experiment [Huybrechts and Payne, 1996], for which the analytical result of a steady state ice sheet configuration has a radius of 579.814 km, instead of 750 km as the initial geometry assumed here.

In line with Ahlkrona et al. [2016], the velocity field and height profile are calculated

after 2.5 years using time steps of a month and redividing the SIA and FS domains every ten time steps. This is done on the coarsest mesh with 17 860 nodes, as used in Ahlkrona et al. [2016] (Figure 6). As far as it is possible to conclude from the figures in Ahlkrona et al. [2016], the results found here (Figure 7 - 9) are similar and also the proportion of the domain Ω_{FS} is. It should be noted that the figures in Ahlkrona et al. [2016] showing differences between the complete FS model and ISCAL are only shown for the finer mesh with 96520 nodes (compared to 17860 here).

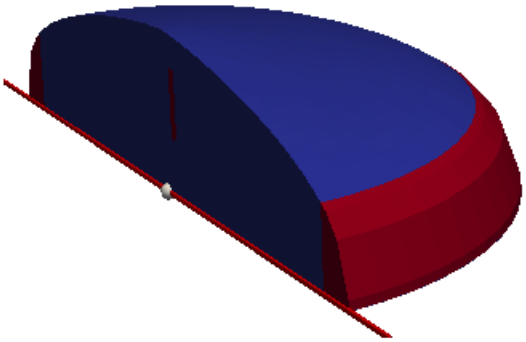

Figure 7: The division of computation domains (FS red, SIA blue), for a mesh with 17860 nodes, after 30 months.

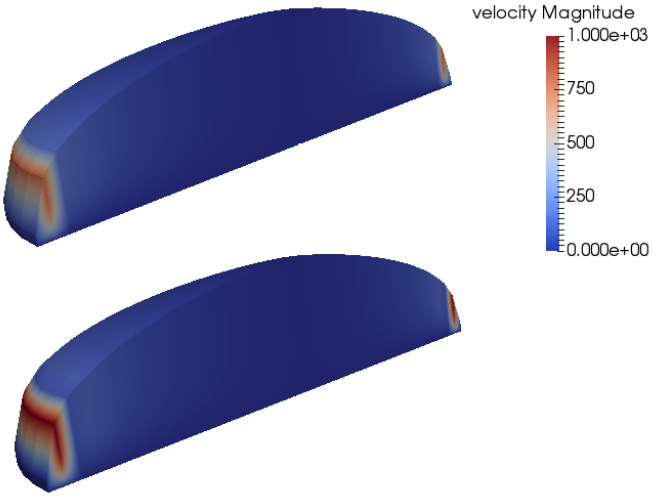

Figure 8: The velocity [m yr^{-1}] computed by ISCAL (upper) and SIA (lower), for a mesh with 17860 nodes, after 30 months. The modeled velocity with SIA around the margin is indeed too high, as expected from the infinite surface slope.

The mesh as used in Ahlkrona et al. [2016] aligns with the boundary of the ice sheet, the thickness of the lateral margin being fixed to a minimum of 100 m. Outflow is allowed through this thin lateral margin, which can be regarded as a calving flux, since Elmer/Ice cannot deal with a changing domain in the horizontal so the domain cannot grow with the ice flow at the margin. Letting the boundary domain coincide with the ice sheet's margin

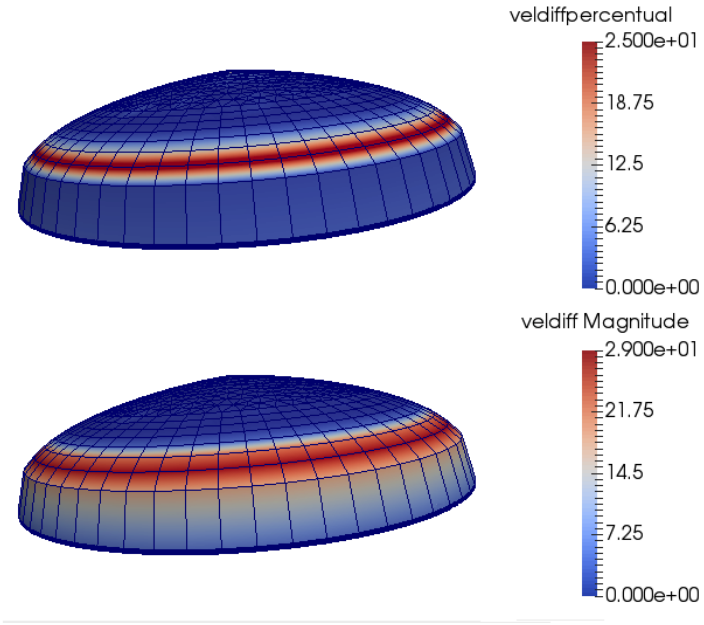

Figure 9: The relative and absolute velocity [m yr^{-1}] difference between FS and ISCAL, for a mesh with 17860 nodes, after 30 months.

is different from the usual approach in Elmer/Ice, where the model domain is larger than the ice sheet, with a small layer of ice in the part of the model domain that is in reality ice free, such that the ice sheet is allowed to grow by evolving the height of this initially ice free layer. Letting the mesh align with the ice sheet's boundary instead fixes the lateral boundaries. It turned out that the choice of the model domain, equal to the ice extent or including an 'ice free' layer around the margin, highly influences the computed velocities (Figure 10). Enlarging the model domain, covering the ice free layer with a negligible thin layer of ice ($H = 100$ m), makes that the velocities are much lower (about a third). Since the bottom velocities are assumed to be zero, the artificial thin layer of ice does not allow for ice leaving the model domain. This conflicts the underlying assumption for which the Vialov profile was derived, namely a flux comparable to calving at the margin. Because of the mismatch in accumulation, an alternative ice sheet profile should be looked for that is physically more realistic.

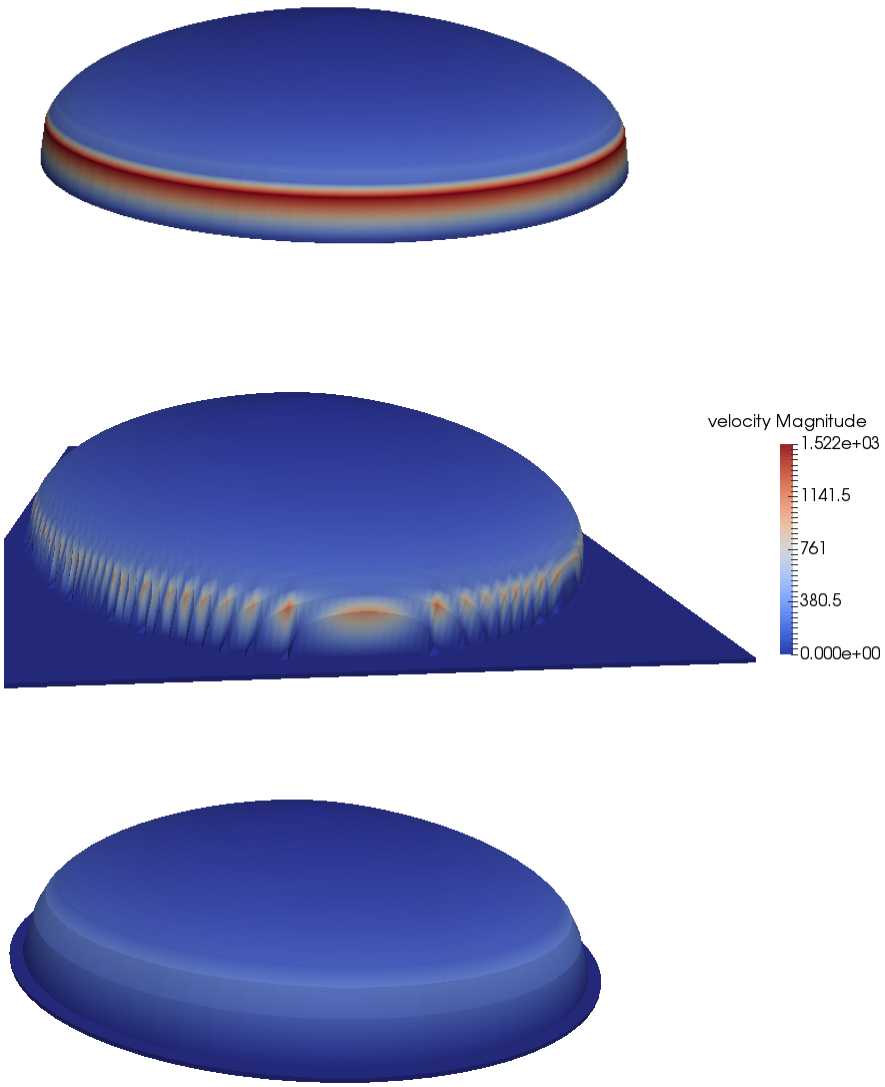

Figure 10: Velocities calculated from the initial Vialov profile (Eq. 71), plotted on the same scale for velocity [m yr^{-1}], showing influence of the mesh. Upper is the original mesh, middle is a structured mesh as applied in Cheng et al. [2017] and lower is like the original mesh but with a larger radius (800km), such that the ice sheet is surrounded by a thin 'ice free' layer.

5.1.2 Bueler profile

As an alternative for the Vialov profile, another analytical solution to the surface height under SIA has been derived in Greve and Blatter [2009], assuming accumulation rates that are positive in the center and ablation at the margin. Besides that, it assumes zero ice flux at both the ice divide and the margins. However, it should be noted that even though the mass balance integrates to zero for a two dimensional cross section, permitting a steady state, the mass balance is negative over the full surface of a three dimensional circular ice sheet. Another unrealistic feature is the steep increase towards the ice divide of the accumulation rate. The initial height profile, called the Bueler profile, and the corresponding mass balance that allows for a steady state in two dimensions are given by

$$\begin{aligned}
h_0 &= 3575.1, L = 750\text{km}, \varepsilon = 100\text{m}, \\
T1 &= h_0/(n-1)^{n/(2n+2)}, \\
T2(R) &= (n+1)\frac{R}{L} - n\left(\frac{R}{L}\right)^{(n+1)/n} + \\
&\quad n\left(1-\frac{R}{L}\right)^{(n+1)/n} - 1, \\
H(R) &= T1 \cdot T2(R)^{n/(2n+2)} + \varepsilon, \\
a(R) &= \frac{\alpha}{L}\left[\left(\frac{R}{L}\right)^{1/n} + \left(1-\frac{R}{L}\right)^{1/n} - 1\right]^{n-1} \\
&\times \left[\left(\frac{R}{L}\right)^{(1-n)/n} + \left(1-\frac{R}{L}\right)^{(1-n)/n} - 1\right].
\end{aligned}$$

For one time step, ISCAL performs as expected. Absolute differences in the velocity produced by FS and ISCAL are indeed bounded by the tolerances and smaller than for the Vialov profile as can be seen in Figure 11. However, oscillations appeared in the vertical velocity, that made the FS solution unstable over longer time simulations. This phenomenon was discovered because the region Ω_{FS} grew over time, hence the error estimation that defines the domain decomposition found differences between the SIA and reference FS solution that exceeded the tolerances, such that applying SIA was not allowed. However, these differences with the reference solution are not caused by the SIA solution being inaccurate, but it differed because it did not show the same oscillations as the FS solution. In hind sight, the simulation of the Vialov profile also showed oscillations in the vertical velocity. This effect is hidden when only looking at the magnitude of the velocity $||\mathbf{u}|| = \sqrt{u^2+v^2+w^2}$, since the vertical velocities are an order of magnitude lower than the horizontal velocities. Extending the simulation time to fifty years made this phenomenon clear since the oscillations appeared in the horizontal velocities as well over time.

Also if the FS solution is computed over the entire domain, the oscillations in the vertical velocity are already present at the first time step (see Figure 13) and do not disappear after a surface relaxation of 20 years where the accumulation profile is defined such that it exactly matches the velocity profile ($a_s(x,y) = -w(x,y,z_s)$) in order to reach a steady

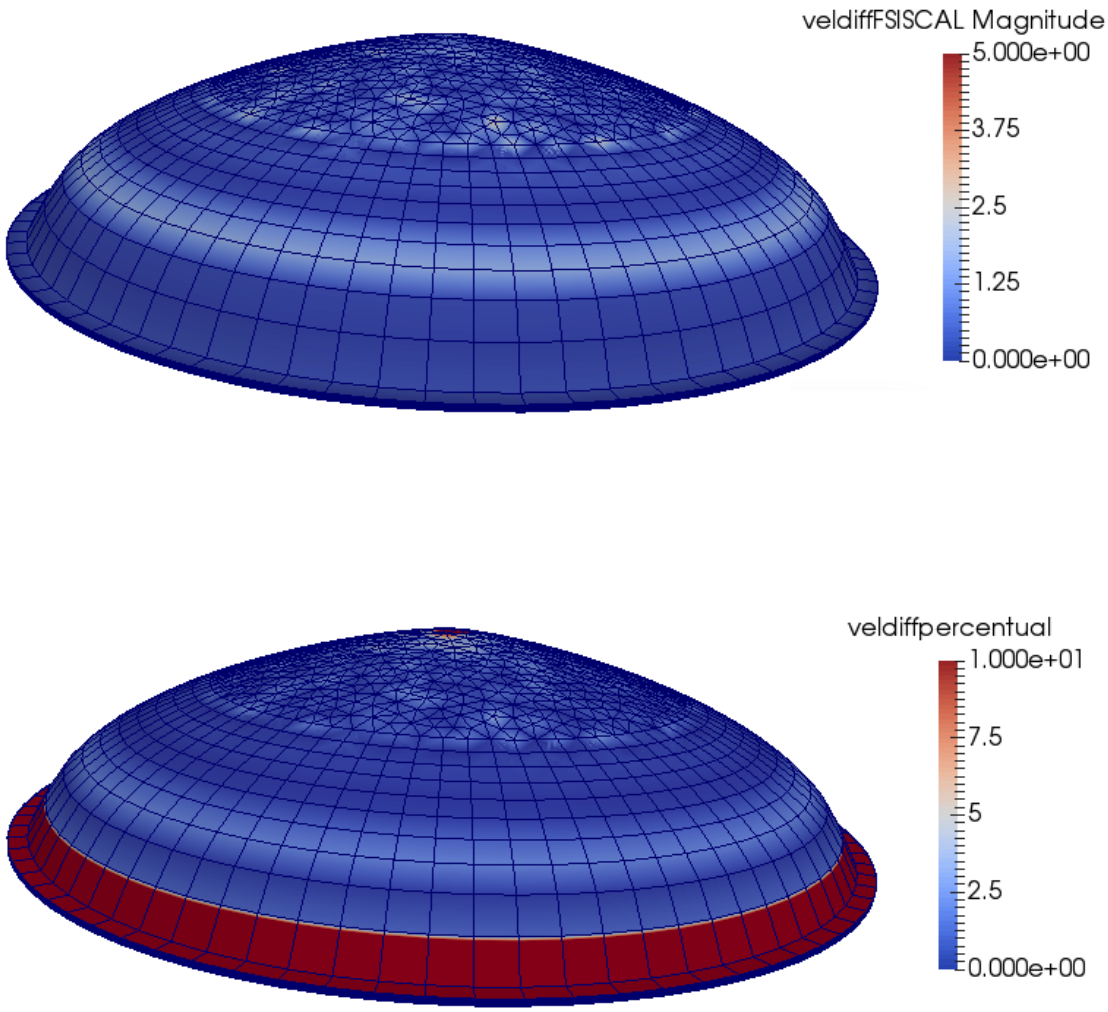

Figure 11: The absolute [m yr^{-1}] and relative [%] velocity difference between FS and ISCAL.

state (T. Zwinger, personal communication, January 2017)[10]. This rules out the possibility of a mismatch of the accumulation and velocity profile to cause the oscillations. Another possible source of the oscillations is the artificial thin layer of ice that surrounds the ice sheet. This layer enables the ice sheet to advance beyond its initial margin without adapting the mesh. However, no publications so far show the influence of this layer on the solution to the FS equations around the ice sheet margin.

A possible solution to the instabilities would be to use P2P1 stabilization (as suggested by Ainsworth and Coggins [2000]). However, currently Elmer/Ice is not capable of using P2P1 elements on extruded meshes. Because three dimensional simulations need to be run in parallel, it is unavoidable to employ mesh extrusion since it ensures that all vertical columns have to be in one partition. However, changing to P2P1 stabilization may not be sufficient, since most research on the stability of FEM relies on the assumption that the elements in the mesh have similar size in all spatial directions. Therefore it may also be

[10]The specific simulation carried out by T. Zwinger was stabilized using the residual free bubbles method on a finer mesh, with a 2D footprint consisting of 5645 nodes, extruded to ten vertical layers.

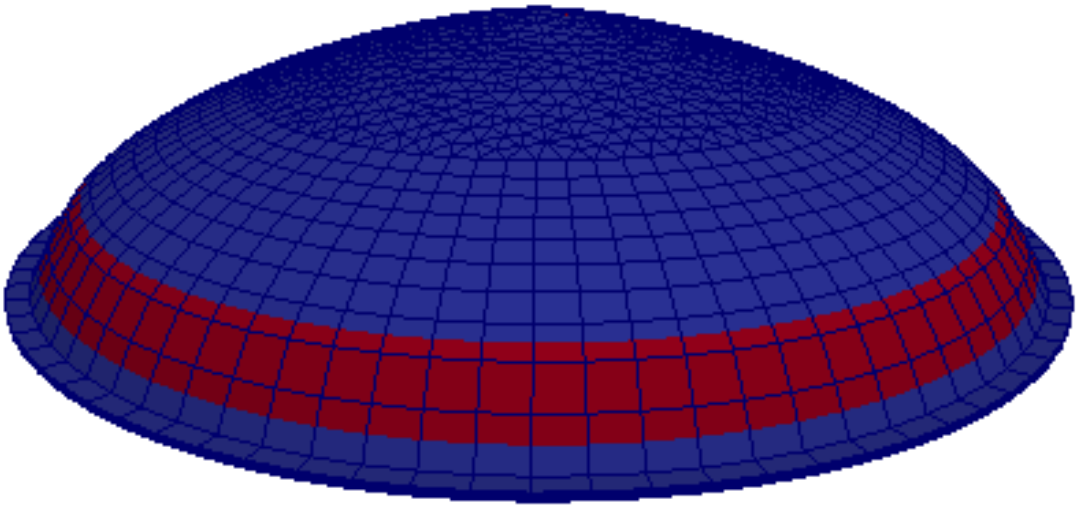

Figure 12: The division of computation domains (FS red, SIA blue).

necessary to increase horizontal resolution, decrease vertical resolution or both, in order to ensure stability. Anisotropic stabilization techniques, for example as presented in Blasco [2008] and Isaac et al. [2015], may overcome stability issues due to high aspect ratios and are therefore suggested to be investigated in further research.

Since it is not the goal of this project to improve the FEM approximation to the FS equations, no further experiments for these geometries will be done. On the other hand, surrounding an ice sheet with shelves around the margin instead of an artificial layer of ice may improve stability. This still enables the ice sheet to grow by an advance of the grounding line. Therefore, subsequent experiments focus on coupling the FS equations to the SSA equations, that will allow more efficient modeling of large ice shelves.

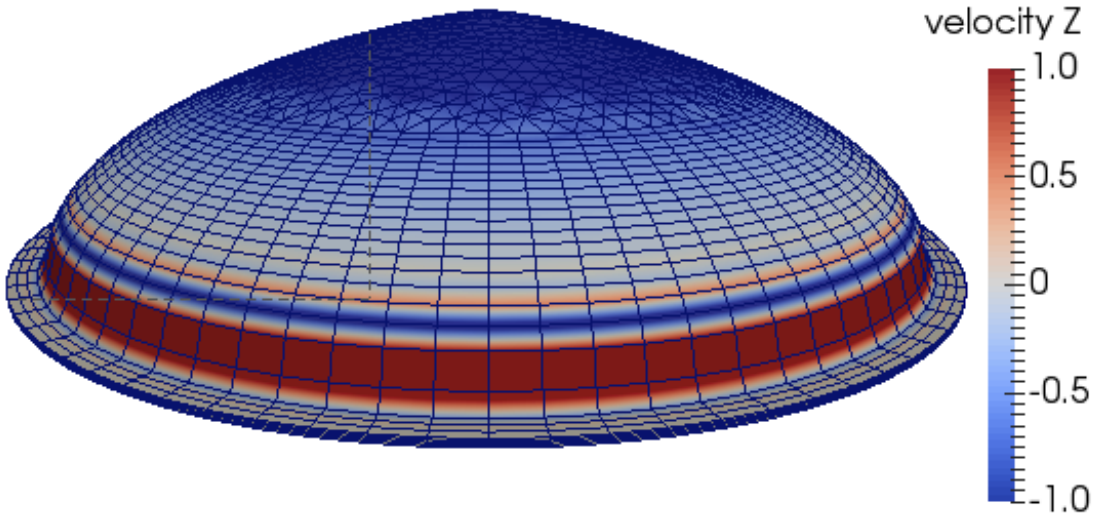

Figure 13: The vertical velocity in the FS solution after one time step.

5.2 Comparison of FS and SSA

In order to find out whether SSA and FS can be coupled, it needs to be verified that the solutions to the two different models correspond sufficiently for a coupling to be feasible. Therefore, a heavily simplified test case is chosen for which the analytical solution to the SSA equations exist in two dimensions, as derived in [Greve and Blatter, 2009]. The ice shelf is 200 km long and an inflow velocity of 100 m yr^{-1} is prescribed at the left boundary, identical over the vertical. The right boundary is assumed to be a calving front, hence the hydrostatic pressure as exerted by the sea water is applied there. The shelf thickness is linearly decreasing from 400m at the inflow boundary to 200m at the calving front. The floatation criterion yields initial values of z_b and z_s from the thickness. The SSA model is expected to be a good approximation of the FS model here, since it satisfies all assumptions to the SSA: small surface slope and aspect ratio and no basal drag. The flow solution for this ice shelf of linearly decreasing thickness, called an ice shelf ramp, is compared for the FS and SSA models as implemented in Elmer/Ice, in both two and three dimensions.

None of the iterative solvers for linear systems in Elmer/Ice converges for problems including a grounding line, therefore all linearized systems are from now on solved directly using umfpack[11], also for the ice shelf only case such that computation times give an indication of what to expect in grounding line problems. Umfpack uses the Unsymmetric MultiFrontal method which in practice may be the most efficient method for solving two dimensional problems as long as enough memory is available, but in three dimensions this may fail [Råback et al., 2016b]. The non-linear systems are solved iteratively using Picard up to a tolerance of 10^{-4} unless specified otherwise.

5.2.1 Two dimensional ice shelf ramp

The domain is discretized by a structured mesh, equidistant nodes on the horizontal axis, extruded along the vertical to quadrilaterals. All constants used and mesh characteristics are specified in Table 1. The resulting horizontal velocity when solving the FS equations for the linearly decreasing ice thickness is shown in Figure 14. The SSA velocity is indeed equal to the analytical solution of the SSA equations given in Greve and Blatter [2009]. The absolute difference between u_{SSA}, u_{FS} turned out to be visible only at the calving front (Figure 15), where the hydrostatic pressure changes over the vertical, inducing a change in u_{FS} over the vertical as well. However, even at the calving front, the relative difference stays below 0.02% of the velocity. Since the vertical velocity is determined by the (gradient of) the horizontal velocity through incompressibility it is of no surprise that the difference between w_{FS} and w_{SSA} also has a maximum close to the calving front. The maximum difference in the vertical component is below 0.12 m yr^{-1}, as shown in Figure 16. Also the relative difference between p_{FS} and the cryostatic pressure stays below 0.03% and thus, the SSA is accurate enough for enabling a coupling FS and SSA

[11] Umfpack home page `http://www.cise.ufl.edu/research/sparse/umfpack/`.

on ice shelves. Computing the SSA solution took only 3% of the time necessary for the FS solution (respectively 0.28 and 8.72 cpu s).

Figure 14: The horizontal velocity in the FS solution for the ice shelf ramp.

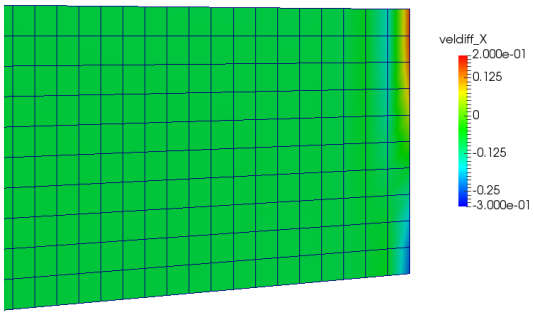

Figure 15: The absolute difference between uncoupled u_{FS}, u_{SSA} [m yr^{-1}].

Figure 16: The absolute difference between uncoupled w_{FS}, w_{SSA} [m yr^{-1}].

Parameter	Symbol	Value	Unit
Glen's exponent	n	3	
Ice density	ρ	900	kg m^{-3}
Sea water density	ρ_w	1000	kg m^{-3}
Gravitational acceleration	g	9.81	m s^{-2}
Fluidity parameter	$\mathcal{A}$	10^{-16}	Pa^{-3} yr^{-1}
Number elements	N_z	10	
	N_x	120	
Max aspect ratio		100	

Table 1: Numerical values of the constants used in ice shelf ramp experiment, inspired by ISMIP-HOM benchmark Pattyn et al. [2008]. Since the shelf is afloat, there is no sliding at the base.

5.2.2 Three dimensional ice shelf ramp

This case is provided by extruding the two dimensional ice shelf ramp, as described in Section 5.3.1.1, along the y-axis. Since the SSA Solver in Elmer/Ice does not allow for locally varying slip coefficients, buttressing cannot be simulated by applying a high slip coefficient in the y direction along the lateral boundaries as is most commonly done (eg. Pattyn et al. [2013]). Instead, buttressing will be simulated by assuming $v = 0$ m yr^{-1}on both lateral boundaries at $y = 0$ and 20 km. All other boundary conditions remain identical to the two dimensional case. The number of elements along the y axis, $N_y = 10$ such that the maximum element aspect ratio remains 100. First the solutions of the FS and SSA model in Elmer/Ice will be compared before applying the coupled model.

The limited width of the domain (20km) in combination with the boundary condition $v = 0$ m yr^{-1} at both lateral sides give a negligible flow in the y direction ($v_{FS} < 10^{-8}$ m yr^{-1}). The main direction of flow is along the x-axis, with the FS model giving velocities up to 6438 m yr^{-1} (see Figure 17). Note that the buttressing slows the ice flow down, since the two dimensional ice shelf ramp showed velocities up to 6552 m yr^{-1}. The SSA model produces higher flow velocities, up to 6532 m yr^{-1} at the calving front, hence the affect of the buttressing at the lateral boundaries appears to be weaker in the SSA model. Despite the differences in the models, the relative difference in u does not exceed 1.5%, as shown in Figure 18. Since the difference between the FS and SSA model are larger in three dimensions, the coupled model is also expected to be less close to the FS solution.

The vertical velocity on the other hand ranges from -27 to 6 m yr^{-1} (negative defined as downward flow). Since the vertical shelf velocity is mainly determined by $\frac{\partial u}{\partial x}$, the vertical velocities are also similar, but again it is not possible to specify a boundary condition for w at the base without taking accumulation into consideration. The vertical velocity

at the base z_b computed by the FS model ranges from 0.1 to 5.8 m yr^{-1}, whereas $w_b = 0$ m yr^{-1} is assumed for the SSA model. The minimum vertical velocity on the other hand is very similar, -27.3 m yr^{-1} for SSA compared to -27.0 m yr^{-1} for FS. Resulting vertical velocities are shown in Figure 19 and the difference in Figure 20. For the coupled case, only the accuracy of u will be examined since this is the velocity component that will determine the surface evolution in future experiments.

On the contrary to the two dimensional ice shelf ramp experiment and the experiments in Ahlkrona et al. [2016], solution time outweighs assembly time by about a factor four in the FS model. The assembly time is 31 cpu s and solution time 117 cpu s averaged over the 27 non-linear FS iterations. The total time of the SSA model is only 0.8% of the FS model (32 cpu s compared to 4005 cpu s).

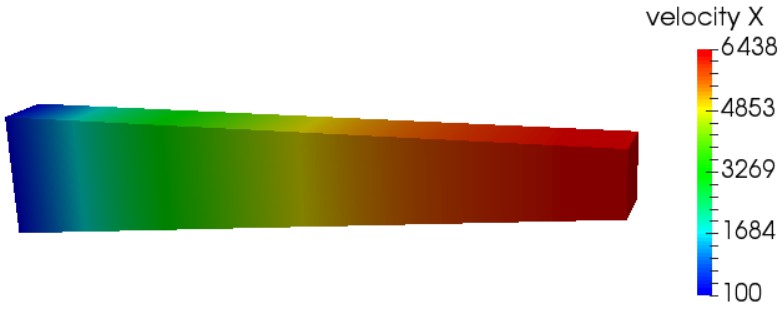

Figure 17: Horizontal velocity u [m yr^{-1}] from FS model solved for the three dimensional ice shelf ramp.

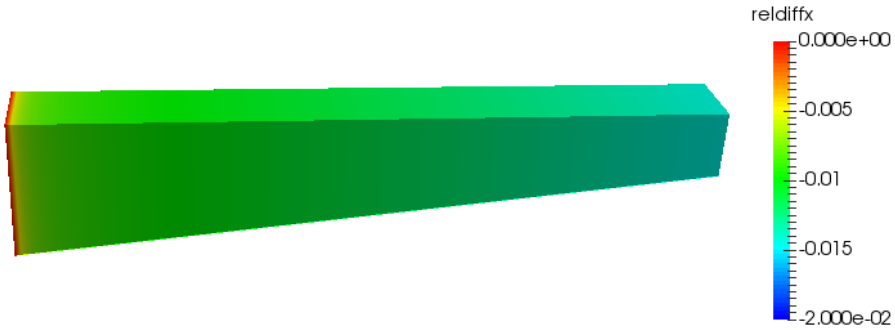

Figure 18: Relative difference in horizontal velocity $(u_{FS} - u_{SSA})/u_{FS}$ for the three dimensional ice shelf ramp.

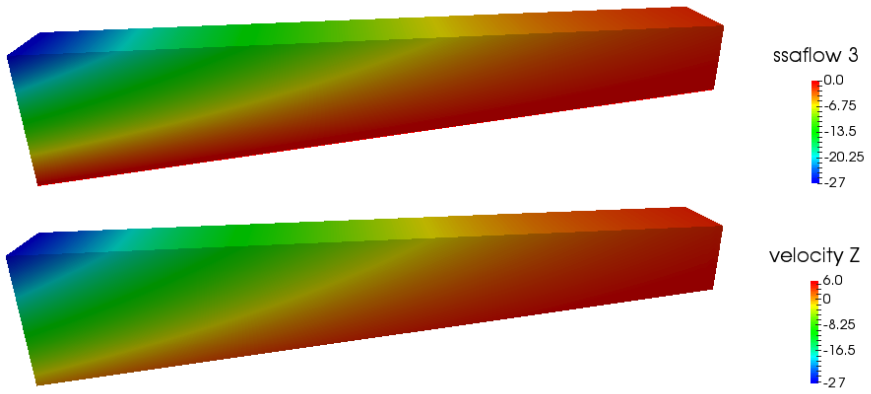

Figure 19: Vertical velocity w [m yr^{-1}] from SSA model (upper) FS model (lower) solved for the three dimensional ice shelf ramp.

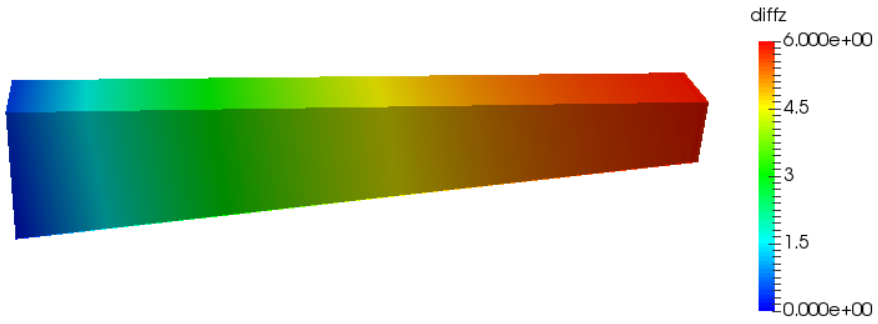

Figure 20: Difference in vertical velocity $w_{FS} - w_{SSA}$ [m yr^{-1}] the three dimensional ice shelf ramp.

5.3 Coupling FS and SSA

A coupling of FS and SSA can show differences when compared to the FS model for two different reasons, resulting from the difference of the two models or resulting from the coupling itself. Since the comparison in the previous section showed that SSA is a very accurate approximation to FS on the ice shelf ramp, the coupling will first be tested for accuracy on this ramp in Section 5.3.1.1 before applying it to more complex grounding line problems in Sections 5.3.1.2 - 5.3.2.2. Grounding line problems for which FS simulations on longer time scales have been done ([Pattyn et al., 2012] and [Gladstone et al., 2017]) are chosen to avoid similar stability problems in the FS solution as were shown in the ISCAL experiments. Since the FS solution has proved to be stable, it should be possible to apply ISCAL, but for both grounding line problems, the friction is low for the entire grounded part of the marine ice sheet, such that SIA is not relevant. The sliding law in the problems could be changed in order to allow for SIA, but this will make the discontinuity of basal drag around the grounding line (with high friction where grounded and no friction where afloat) even larger, such that it the problem will be more difficult to solve. Therefore, it is chosen here to use to the original sliding laws as in Pattyn et al. [2012], Gladstone et al. [2017] and only couple FS and SSA.

First, diagnostic experiments will be performed, only solving the model for the initial geometry. Since the geometry of the ice sheet changes after every time step induced by the velocity profile, a difference in the velocity of the coupled model compared to the FS model will lead to a different geometry. The velocity solution in prognostic experiments is therefore harder to compare, since differences can come both from the coupling or from the different geometry for which the velocity is solved. These diagnostic runs are only discussed in terms of accuracy with respect to the FS model, since the computation time for the first time step is not representative for all subsequent time steps, when the previous solution is used as an initial guess for Picard iteration. The diagnostic grounding line problems also serve to evaluate the criteria for dividing Ω_{FS} and Ω_{SSA} as suggested in Section 5.3.1.4. Afterwards, the results of prognostic runs for the grounding line problems are investigated for both accuracy and efficiency compared to the FS model. All experiments assume a convergence tolerance $\epsilon_c = 10^{-4}$ for the coupled model.

Most three dimensional experiments require solving the FS model in parallel, which introduces many new challenges that are outside of the scope of this project. However, the three dimensional ice ramp can be solved in serial and the results of the SSA-FS coupling are discussed in Section 5.3.3.

5.3.1 Two dimensional diagnostic runs

5.3.1.1 Ice shelf ramp

It has been shown in Section 5.2, that the SSA and FS solution are nearly identical for the ice shelf ramp of linearly decreasing ice thickness. Therefore, this experiment is a first test case to assess the accuracy of the SSA-FS coupling. The method for coupling has been described in Section 4.2. The method is slightly adapted here, since there is no grounding line present, the coupling location x_c is defined to be in the middle of the domain at $x = 100$ km. The resulting coupled velocity u_c is not shown here since it is impossible to see differences with u_{FS} as in Figure 14.

In the FS model, $u_{FS}(100\text{km}, z_b) = 4805$ m yr^{-1}. In the first iteration, where the cryostatic pressure is applied as an external force to the FS domain, the coupled velocity is equal to the inflow velocity $u_c(x_c, z_b) = 100$ m yr^{-1}. To understand this, one should realize that the acceleration on the ice shelf is caused by the imbalance or the hydrostatic pressure applied at the calving front, compared to the cryostatic pressure. Therefore, when applying a cryostatic pressure, there is no acceleration of the ice flow. Already in the second iteration, where the contact force f from the SSA solution is taken into the boundary condition for the FS equations at x_c, $u_c(x_c, z_b) = 4790$ m yr^{-1}, a relative difference of about 0.3%.

The comparison of FS and SSA in the previous section showed that the SSA equations are a very good approximation to FS when the same inflow velocity is specified, which implies that the error in the SSA part completely depends on the error in the inflow velocity $u_{FS}(x_c)$. As expected, the error is also about 0.3% in Ω_{SSA} but there is a slight error increase visible at the calving front where u_{FS} varies with z. The maximum relative error in the coupled simulation is still 0.3%. In the third coupled iteration, both FS and SSA are solved only once to find that the coupled system has converged up to the tolerance of 10^{-4}.

The relative difference between the coupled model and FS is of one order magnitude larger than the relative difference between FS and SSA only model as calculated in the previous section. However, SSA can only be applied when the entire shelf satisfies the floatation criterion, which is not always the case close to the grounding line. As Pattyn et al. [2012] pointed out, the FS equations need to be solved for grounding line dynamics. The successful evaluation in this test case allows for the method to be tested in such a challenging set up with a grounding line.

5.3.1.2 MISMIP

In order to be able to compare the model results, the first grounding line problem consists of the idealized two dimensional ice sheet geometry of the Marine Ice Sheet Model Intercomparison Project. The geometry is equal to the first experiment EXP1, where the

bedrock is given by

$$b(x) = 720 - \frac{778.5\ x}{750 \cdot 10^3}, \tag{73}$$

where both x and b are given in meters. Note that this is a down-sloping bedrock, not a retrograde bedrock that is point of focus for the MISI, instead the ice sheet is expected to evolve to a steady state position when accumulation is kept constant. The initial ice geometry is derived from a boundary layer theory for sheet-shelf interactions [Schoof, 2007]. This theory uses a systematic set of approximations to parameterize a simpler, shallow ice model for the sheet-shelf transition zone. It allows for semi-analytical calculation of steady states at low computational cost. However, it should be emphasized that the boundary layer theory itself is only approximate, part of the objective of MISMIP was to compare it to other models. The upstream boundary at $x = 0$ km is regarded as an ice divide and a Dirichlet boundary condition for the horizontal velocity $u = 0$ m yr^{-1} is applied to ensure symmetry. The downstream boundary at the end of te domain at $x = 1800$ km is modeled as a calving front (Eq. 40). Note that ice is allowed to flow through this boundary, such that the ice flux out of the model domain can be regarded as a calving flux. Calving events are however not modeled, the calving front is artificially fixed at the same position throughout all experiments.

A non-linear friction law is specified as the Weertman type sliding law given in Equation 35, constants and mesh characteristics are as specified in Table 2. The set up is exactly equivalent to the test case in the Elmer/Ice repository called GL_MISMIP[12]. The horizontal element length varies from 41 km to a refined resolution of 100 m around the grounding line. The vertical elements are equally divided over the thickness. The FS solution of the horizontal velocity is shown as reference in Figure 21.

[12] Available at `https://github.com/ElmerCSC/elmerfem/tree/devel/elmerice/Tests/GL_MISMIP`

Parameter	Symbol	Value	Unit
Glen's exponent	n	3	
Ice density	ρ	900	kg m^{-3}
Sea water density	ρ_w	1000	kg m^{-3}
Gravitational acceleration	g	9.8	m s^{-2}
Fluidity parameter	$\mathcal{A}$	$4.6416 \cdot 10^{-25}$	Pa^{-3} yr^{-1}
Surface accumulation	a_s	0.3	m yr^{-1}
Sliding parameter	β_m	$7.624 \cdot 10^{6}$	Pa m $^{-1/3}$ yr $^{1/3}$
Sliding exponent	m	1/3	
Number elements	N_z	20	
	N_x	200	
Max aspect ratio		4806	

Table 2: Numerical values of the constants used in MISMIP experiment.

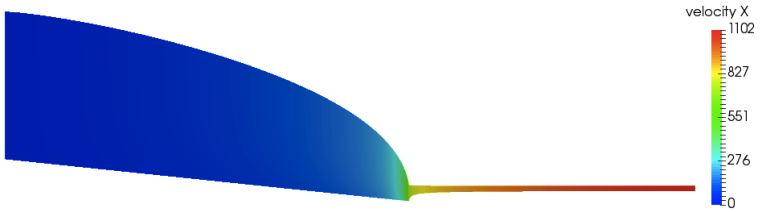

Figure 21: The horizontal velocity [m yr^{-1}] when solving FS over the entire modeling domain for MISMIP.

The location for coupling is defined prior to applying the coupling, by examining the maximum difference in the nodal values $u_{FS}(x_{GL} + d_{GL}, z_i)$ over the vertical as a function of the distance to the grounding line d_{GL}, when solving the FS equations for the entire model domain. This difference is shown in Figure 22 and lead to the choice of defining the coupling at 30 km from the grounding line, where the difference is below 0.01 m yr^{-1}. This leads to 79 % of the nodes being located in the FS domain. This may sound worrying for the potential efficiency of the coupling, however one should realize that the grounded part can be modeled by ISCAL in future experiments which will increase efficiency compared to the FS model. Again, the differences between the FS and coupled solution are very small after the second iteration. The error in the u_{SSA} is only 0.03% but the error in u_{FS} is higher, not at the coupling interface but around the grounding line, as shown in Figure 23. However, the error is still very low, approximately 0.4%.

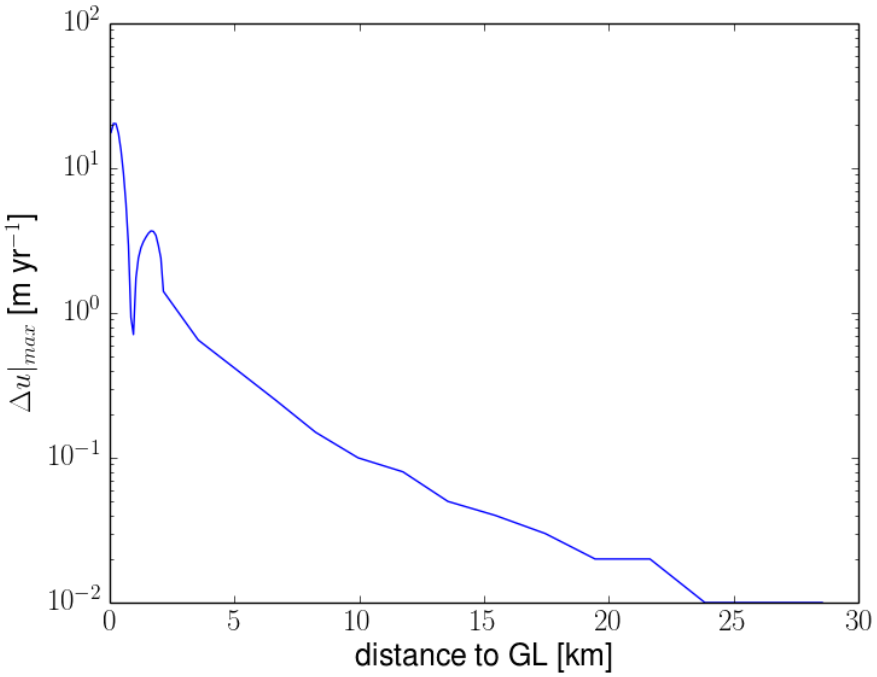

Figure 22: The maximum difference in u_{FS} over the vertical axis with respect to grounding line distance when solving the FS equations over the entire domain for MISMIP.

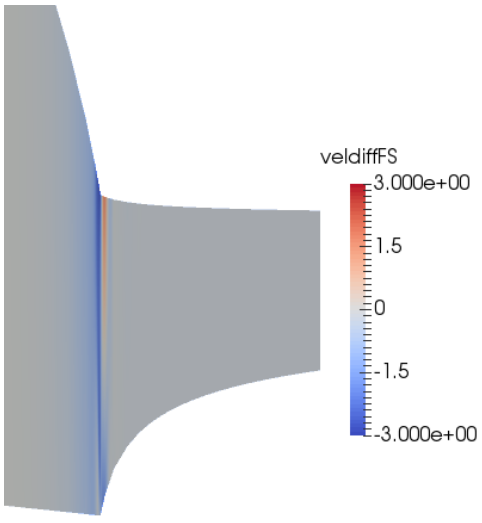

Figure 23: Difference between coupled and original FS horizontal velocity [m yr^{-1}] in Ω_{FS} for MISMIP, close up of the area around the grounding ilne.

5.3.1.3 Budd's MIS

As second grounding line problem, the coupling is applied to a similar idealised marine ice sheet, but now subject to Budd's sliding law [Gladstone et al., 2017], therefore called Budd's Marine Ice Sheet (Budd's MIS) from now on. As explained in Section 2.3.1, applying Budd's sliding law reduces sensitivity to mesh resolution such that an equidistant grid spacing of 3.6 km along the horizontal can be applied (resolution R1 in Gladstone et al. [2017]). The experiment is almost equivalent to Gladstone et al. [2017]. Again, the domain starts with an ice divide at $x = 0$ ending in a calving front at $x = L = 1800$ km. The bedrock has a lower slope now and is given in meters with respect to sea level by

$$b(x) = 200 - 900\frac{x}{L}. \tag{74}$$

Basal melt is neglected, the surface accumulation is a function of the distance from the ice divide, in m yr^{-1} as

$$a(x) = \frac{\rho_w}{\rho}\frac{x}{L}. \tag{75}$$

Other characteristics of the experiment are specified in Table 3.

Parameter	Symbol	Value	Unit
Glen's exponent	n	3	
Ice density	ρ	910	kg m^{-3}
Sea water density	ρ_w	1000	kg m^{-3}
Sliding parameter	β_m	$7 \cdot 10^{-6}$	MPa m $^{-4/3}$ yr $^{1/3}$
Sliding exponent 1	m	1/3	
Sliding exponent 2	q	1	
Temperature	T	-10	$^\circ$ C
Number elements	N_z	11	
	N_x	500	
Max aspect ratio		130	

Table 3: Numerical values of the constants used in Budd's MIS experiment.

The diagnostic experiment of the coupling is conducted on a steady state geometry. In order to reach this steady state, several simulations with the FS model were done. First, the spin up experiment is repeated (called SPIN in Gladstone et al. [2017]), starting from a uniform slab of ice (H=300 m). In Gladstone et al. [2017] there was a parametrized buttressing force applied to the entire ice sheet to mimic a three dimensional ice sheet. However, the SSA solver in Elmer/Ice does not allow for body forces other than gravity, therefore, the buttressing is neglected here. The geometry following from the spin up that includes buttressing is therefore simulated without buttressing until a new steady state is reached. When removing buttressing, the grounding line retreats from 871.2 km to a steady state grounding line position at 730.8 km. Here, a grounding line position is called steady once it did not change over a period of at least 500 years. It should be noted

that the total ice sheet volume is still changing when a steady grounding line position is reached, but the relative change is below 10^{-5}.
The horizontal FS velocity u_{FS} [m yr^{-1}] is given in Figure 24. A significant difference with this experiment compared to MISMIP is that the sliding is much higher, such that the SSA is a better approximation to the ice velocity also for the grounded part. In fact, at the grounding line $u_{FS} = 904$ [m yr^{-1}] over the entire vertical axis, showing the same independence with respect to the vertical as the SSA solution. Thus, the difference in horizontal velocity over the vertical cannot be used to determine a suitable coupling location x_c, therefore a distance of to the grounding line $d_{GL} = 30$ km is chosen again such that results can be compared to the MISMIP experiment. This results in 42 % of the nodes inside Ω_{FS}.

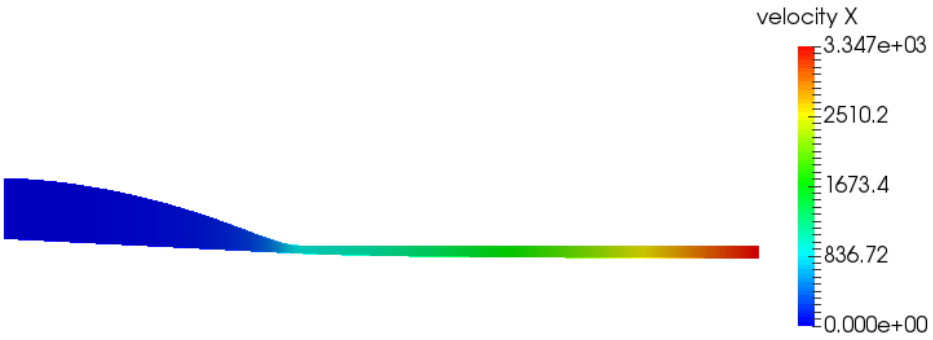

Figure 24: u_{FS} [m yr^{-1}] Budd's MIS

With a tolerance of 10^{-4} for the coupled iterations, the coupled model converged after in total 27 FS iterations, compared to 24 in the FS only model with a tolerance of 10^{-4} for the non-linear iterations. The maximum difference between u_{FS} and u_c is 13 m yr^{-1} at the calving front, the relative difference is given in Figure 25.

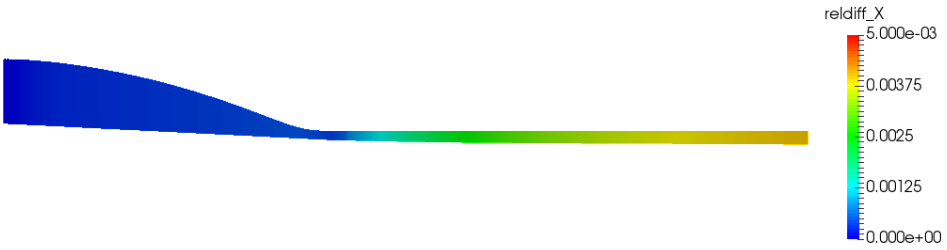

Figure 25: Relative difference $|u_{FS} - u_c|/u_{FS}$ for the diagnostic Budd's MIS experiment, reaching a maximum $< 0.5\%$ at the calving front.

5.3.1.4 Redefinition of Ω_{SSA}

The diagnostic experiments show that the differences between the FS model and coupled model are very small. Therefore, a reference solution by solving the FS equations once as suggested in Section 4.2.2 will also give very small differences between the coupled solution and the reference solution. Redefining Ω_{SSA} upon the error with respect to u_{ref} as

in Equation 69with a tolerance comparable to the convergence tolerances will not change the domain division following from the initial division by grounding line distance.

It would be an option for the MISMIP experiment to use $\frac{\partial u_{ref}}{\partial z}$ as in Equation 70 to automatically change the distance $d_{GL} = |x_c - x_{GL}|$, as $\frac{\partial u_{ref}}{\partial z}$ changes over time. On the other hand, Budd's MIS experiment shows that the magnitude of $\frac{\partial u}{\partial z}$ is problem dependent, hence relating the coupling location x_c to $\frac{\partial u}{\partial z}$ cannot be done in a systematic way for all experiments. A distance of 30 km with respect to the grounding line showed to be sufficient for both MISMIP and Budd's MIS. Decreasing this distance may still give an accurate coupled solution. However, it depends on the mesh resolution how much potential decreasing d_{GL} has for increasing efficiency. For paleo simulations, one should strive to mesh resolutions compared to the equidistant mesh of Budd's MIS. In that case, decreasing d_{GL} by say 10 km will not change the percentage of nodes in Ω_{FS} significantly (0.6%). Therefore, in all subsequent experiments, a minimum distance of 30 km between the grounding line and coupling interface will be applied. The coupling is still dynamic in the sense that the coupling location changes together with the grounding line.

5.3.2 Two dimensional prognostic runs

Now that the coupled model has shown to yield accurate results in the diagnostic experiments and the criteria for domain division have been examined, the coupling can be applied to prognostic experiments. Besides assessing the accuracy over a longer time span, the goal of these experiments is also to examine efficiency.

5.3.2.1 MISMIP

As for the test case in the Elmer/Ice repository, only 10 time steps with dt = 0.5 yr are performed since the grounding line otherwise advances outside of the refined area. This prognostic run will be used both to assess accuracy of the time evolution and efficiency. As suggested in Section 4.2, the maximum number of FS iterations per coupled iteration can be changed, aiming to minimize the total number of FS iterations. In this experiment, a maximum number of iterations from 1 to 10 will be tested, named C1 to C10, and without limitation of the maximum number, C100, always letting Picard iteration for Ω_{FS} converge to the overall tolerance 10^{-4}. The computation time of SSA iterations is much smaller, therefore they will always be solved up to the overall convergence tolerance of 10^{-4}. Regardless of the limitation of the number of FS iterations per coupled iteration, the coupled model converges to the same result, hence for accuracy with respect to the FS model, only C100 will be regarded.

MISMIP - Accuracy After 5 years, the maximum absolute velocity difference between FS and C100 is 18 m yr^{-1}, the maximum relative difference 1.9%. The maximum difference in ice thickness is 0.11 m. Since the most important quantity for SLR is the flux over the grounding line, the velocity u_b and grounding line x_{GL} are compared in Figure

26, ice thickness at the grounding line H_{GL} and grounded volume V_g are shown in Figure 27. The grounding line advances in almost every time step and the velocity u_b decreases until $t = 3$ yr when it starts to show oscillatory behavior, the same oscillatory nature is also present for H_{GL}. This could mean that the FS model is not converged with respect to mesh resolution. Differences between FS and C100 however are hardly visible.

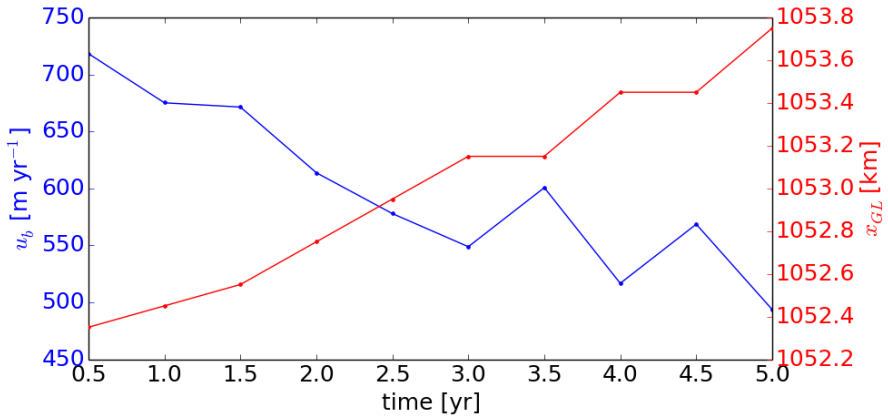

Figure 26: Evolution of the basal velocity u_b at x_{GL} and x_{GL} itself over time, the FS model shown with a continuous line and C100 with dots.

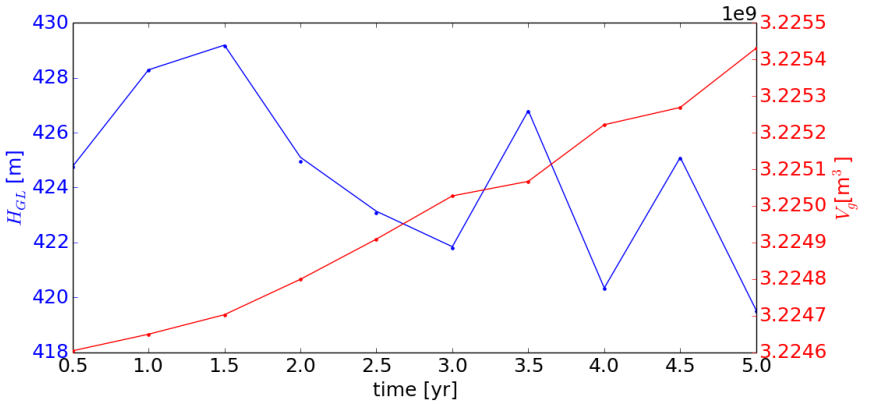

Figure 27: Evolution of the thickness H at x_{GL} and the grounded volume V_g over time, the FS model shown with a continuous line and C100 with dots.

MISMIP - Efficiency The computation time of the FS solver can be divided in three parts; matrix assembly (t_A), solving of the linear system (t_s) and all time that is left will be called overhead ($t_{FS,o}$). The overhead time amongst others consists of launching the solver, hence allocating memory space for vectors and matrices. Therefore, the overhead time is almost constant for every time the FS solver is called. For the coupled model, the total time spent by the two SSA solvers (one for the horizontal velocities and one for the vertical velocity and pressure, t_{SSA}) will also be investigated. The total overhead time t_o will be defined as

$$t_o = t_{tot} - t_A - t_s - t_{SSA}, \tag{76}$$

where t_{tot} is the total cpu time [s] of the entire experiment, such that t_o not only consists of launching the solvers but also the surface update and solvers for post processing. Computation times for C1 - C10, C100 and FS are given in Table 4, which shows that indeed as suggested in Ahlkrona et al. [2016], assembly time of A_{FS} dominates computation time. When limiting the number of FS iterations per coupled iteration, the total number of FS iterations decreases as expected. If only one FS iteration is performed per coupled iteration, the increase in FS iterations is only 6.4%. However, even though only 79% of the elements is in Ω_{FS} and the number of degrees of freedom for the FS equations is four, assembly time t_A for the coupled model is always higher than for FS. It turns out that for both models, the mean assembly time per FS iteration is equal, despite the decreased size of the matrix A_{FS} when restricted to Ω_{FS}. This can be explained by the way the coupled model is implemented. Elements in Ω_{SSA} are defined passive when executing the FlowSolver. While the user manual of Elmer/Ice states that passive elements are not included in the global matrix assembly (see Chapter 13.4 of the manual [Råback et al., 2016b]), apparently either checking whether an element is passive or not is apparently equally time consuming, or the FlowSolver does assembly A_{FS} for passive elements in contrast to the information provided in the manual. The mean solution time per iteration for the FS solver is slightly smaller for the smaller domain Ω_{FS} in the coupled models, 0.12 cpu s compared to 0.14 cpu s for FS. This decreased solution time is however not visible in the total computation time since assembly time dominates, but that may be different in larger (three dimensional) problems. Finally, since the overhead time of launching solvers increases when more coupled iterations are necessary (see Table 4), the fastest coupled model configuration in this experiment is C4 instead of C1, despite the total number of FS iterations being slightly higher.

model	t_A	t_s	# FS iterations	t_o	t_{tot}	t_{SSA}	# coupled iterations
FS	222	22	156	22	266	-	-
C100	359	30	252	85	487	14	68
C10	306	26	216	84	430	14	68
C9	294	24	207	83	416	14	67
C8	286	23	200	82	405	14	66
C7	286	24	201	84	407	14	68
C6	282	23	197	88	407	15	70
C5	277	23	192	94	409	16	74
C4	269	22	188	98	404	16	77
C3	273	22	190	114	428	19	89
C2	272	23	190	141	459	24	110
C1	238	20	166	232	530	41	176

Table 4: Computation times [cpu s] in total for ten time steps for MISMIP. Model Ci denotes the coupled model with i being the maximum number of non-linear FS iterations per coupled iteration.

The number of FS iterations per time step is shown for all experiments in Figure 28. A peak in FS iterations is visible at $t = 4$ yr for all coupled model experiments. This coincides with change in coupling location x_c. Because the mesh is refined around x_{GL}, the coupling interface changes just once despite the grounding line advancing every time step. The increase in FS iterations can be explained by the value of the contact force f_{SSA}, which is close to zero except for the boundaries $\partial\Omega_{SSA}$ (as expected since the residual should go to zero on the interior for a converged solution). Therefore, when x_c and hence $\partial\Omega_{SSA}$ changes, the coupled model starts with $f_{SSA} \approx 0$ and will need more coupled iterations to converge. The time evolution of the contact force $f_{SSA}(x_c)$ and velocity $u_{SSA}(x_c)$ is shown in Figure 29. The mean $\bar{f}_{SSA}(x_c) = -20$ m MPa with standard deviation 0.6 m MPa, hence using the contact force at the previous coupling interface in the initialize step of the coupled model (see Figure 5) instead of at the newly defined location x_c, where it is close to zero, will most likely increase convergence speed and hence decrease computation time. If this is done for C4, the number of FS iterations at t=4 yr is 21, compared to 25 originally so it does increase efficiency. However, reusing of the old contact force when the coupling interface changes is not generally implemented yet due to time constraints of this project.

5.3.2.2 Budd's MIS

Starting from the steady state investigated in the diagnostic experiments, the temperature T [°C] is lowered over a period of 500 years to -30 °C according to

$$T(t) = \begin{cases} -10(2 - \cos(2\pi t/500)) & \text{for } t \leq 500 \\ -10 & \text{for } t \geq 500, \end{cases} \tag{77}$$

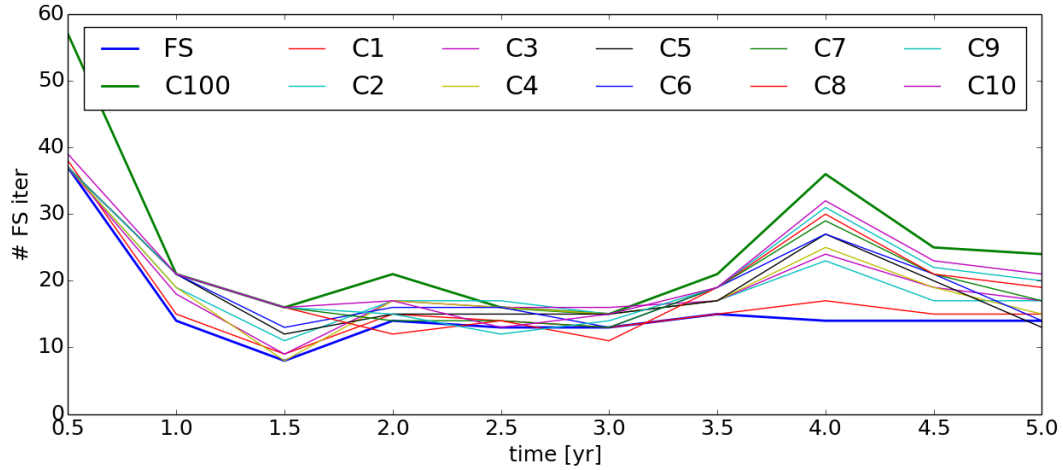

Figure 28: Number of non-linear FS iterations over time.

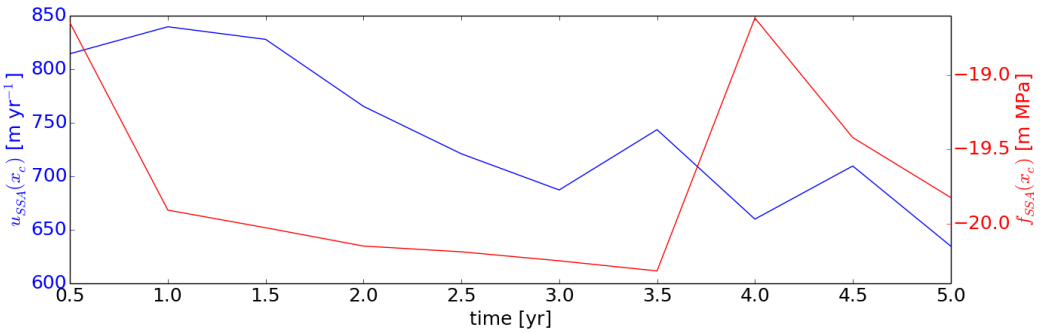

Figure 29: Evolution of $u_{SSA}(x_c)$ and $f_{SSA}(x_c)$ over time, note this is equal for all coupled models C1 - C100.

inducing a grounding line advance. Afterwards, the temperature is kept at -10 °C again for the next 2500 years. Again, first accuracy of the coupled model will be discussed before investigating the efficiency.

Budd's MIS - Accuracy The maximum velocity difference between the coupled and FS model after 3000 years is 10 m yr^{-1}, shown in Figure 30. The relative difference is below 1.6% when only regarding the absolute differences of at least 1 m yr^{-1}. Time evolution of $x_{GL}, u_b(x_{GL}), H_{GL}$ and V_g are shown in Figure 31 and 32. In general, the velocities found by the coupled model are slightly higher, with a maximum relative difference of 5.3% in the entire experiment. The grounding line advances to $x_{GL} = 1036.8$km in the FS model and $x_{GL} = 1044$km in the coupled model. The FS model goes back to the original $x_{GL} = 730.8$ km, but the coupled model still gives $x_{GL} = 734.4$, a difference of one grid point. These difference may partly originate from the low bedrock slope, which makes it harder to define the grounding line position from the geometry. The thickness at the grounding line is very similar, $H_{GL} = 350$ at the furthest advance of the FS model compared to $H_{GL} = 354$ for the coupled model. Also the difference in $u_b(x_{GL})$ is still below 5%. The output from the FS model shows that from 841 years onwards, the grounded

line computed from the geometry is actually located at $x_{GL} = 741.6$ km. However, the final grounding line is redefined by evaluating the contact problem (see Section 2.2.3) after Picard iteration for $\mathbf{u}_{FS}$ has converged up to 10^{-3}.

Then, it turns out that from 1667 years onwards, $-\sigma_{nn}|_b \leq p_w(z_b, t)$ for $x \in \{741.6, 738, 734.4\}$ km such that the new grounding line is defined at $x_{GL} = 730.8$ km. For the coupled model on the other hand, $x_{GL} = 734.4$ is already computed from the geometry from 1101 years onwards and the hydrostatic pressure by the sea water does not change x_{GL}. It should be noted that the grounded volume (Figure 32) is still slightly decreasing, so a steady state geometry is not reached yet. Integrating the accumulation over the model domain yields

$$\int_0^L \frac{\rho_w}{\rho} \frac{x}{L} dx = \frac{\rho_w L}{2\rho} = 989011 \text{m}^2 \text{yr}^{-1}. \tag{78}$$

In order to reach a steady state, this should be compensated by the calving flux $H(L) \cdot u(L)$. After 3000 years, for the coupled model, $H_c(L)u_c(L) = 296 \cdot 3358 = 992818$ m^2 yr^{-1} and $H_{FS}(L)u_{FS}(L) = 296 \cdot 3361 = 994178$ m^2 yr^{-1}, so both are indeed not in steady state yet.

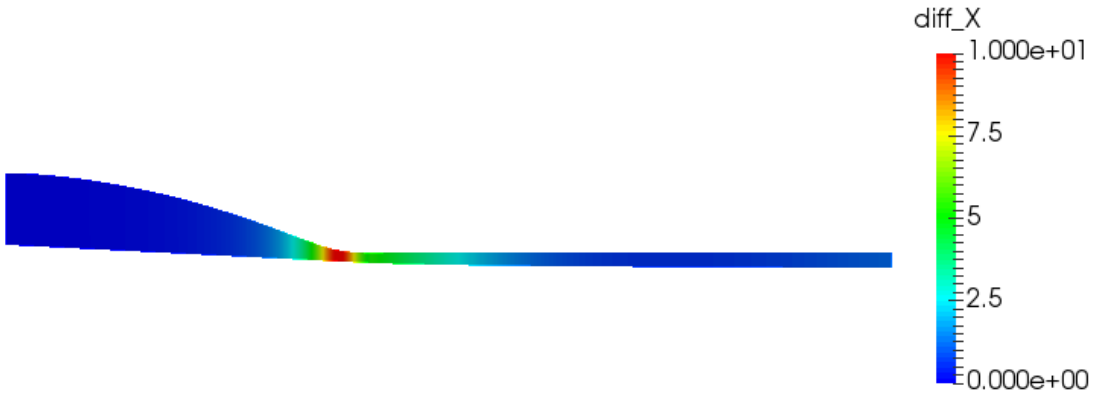

Figure 30: Absolute difference between u_{FS}, u_c [m yr^{-1}] after 3000 years.

Budd's MIS - Efficiency Again, finding the optimal coupled model is a matter of balancing the number of FS iterations and coupled iterations, since the latter involve extra overhead time of launching the solvers. As given in Table 5, the fasted coupled simulation is when limiting the number of FS iteration per coupled iteration to 3. . The coupled model now turns out to be faster that the FS model because it needs less FS iterations to converge, leading to a decrease of almost 10% of the computation time. This can be explained by the difference in grounding line position as explained in the previous section. The retreat of the grounding line in the FS model by the hydrostatic pressure leads to a change in basal boundary conditions, which makes that more non-linear FS iterations per time step are necessary to converge (5 in total for almost the entire period after 1100 years, shown in Figure 33). On the other hand, since the normal stress in the coupled model exceeds the water pressure, the grounding line is not changed during Picard iteration for the FS velocity, hence only one non-linear FS iteration is needed for convergence (the norm compared to the previous time step is already below the convergence tolerance). It

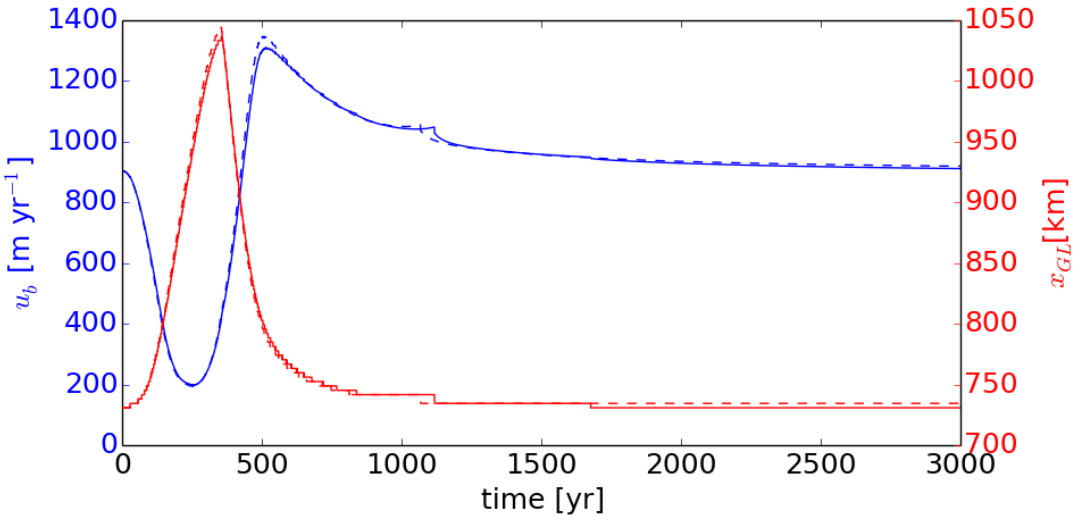

Figure 31: Time evolution of x_{GL} (red) and $u_b(x_{GL})$ (blue), continuous line for FS, dashed for coupled model.

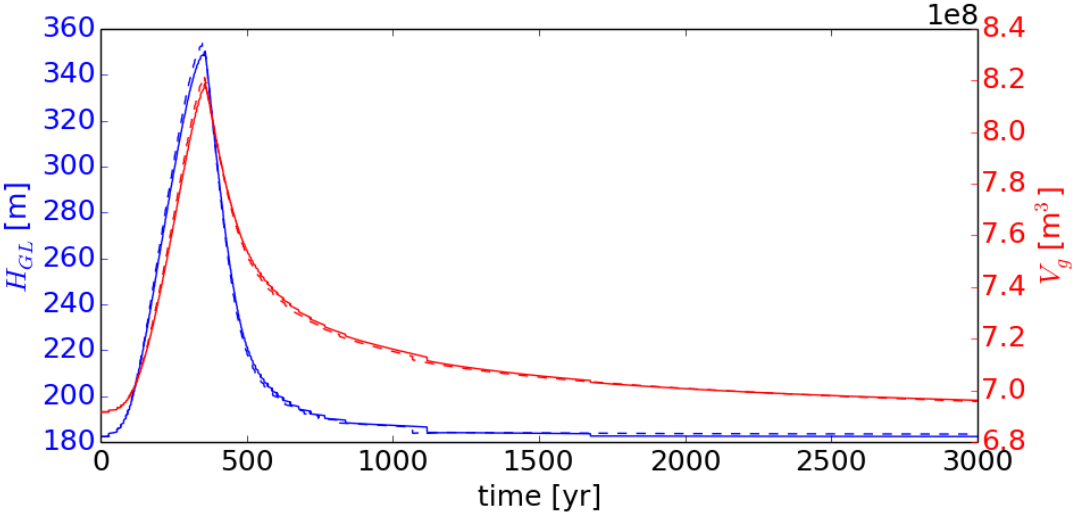

Figure 32: Time evolution of H_{GL} and V_g continuous line for FS, dashed for coupled model.

should be noted that t_{SSA} (including solver launching, assembling and solving for $\mathbf{u}_{SSA}$) is now of comparable size as t_s for FS, but this excludes assembly of A_{FS} which is still dominating the total solution time.

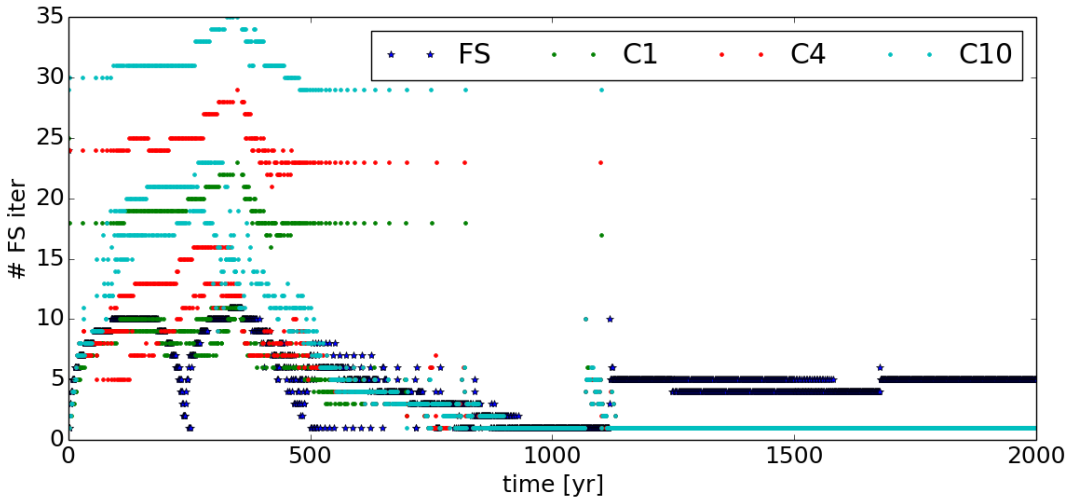

Figure 33: The number of FS iterations per time step. For clarity, only the coupled models C1, C4 and C10 are shown and all are shown until $t = 2000$ yr since nothing changed afterwards.

model	t_A	t_s	# FS iterations	t_o	t_{tot}	t_{SSA}	# coupled iterations
FS	36481	2399	14966	9760	48641	-	-
C10	33704	1854	13916	12300	49724	1866	8040
C9	32822	1842	13481	12501	49066	1901	8115
C8	31910	1807	13127	12661	48296	1918	8199
C7	30946	1719	12640	12687	47276	1924	8230
C6	29616	1671	12154	12880	46116	1950	8349
C5	28234	1594	11577	13182	44998	1987	8502
C4	26983	1500	11117	13613	44143	2047	8766
C3	26033	1455	10677	14402	44040	2150	9218
C2	24747	1368	10187	15877	44334	2342	10065
C1	22994	1271	9475	20043	47135	2826	12475

Table 5: Computation times [cpu s] in total for 3000 yr Budd's MIS. Model Ci denotes the coupled model with i being the maximum number of non-linear FS iterations per coupled iteration.

The contact force f_{SSA} after convergence of the coupled model is shown in Figure 34. Since the velocity is changing more during the experiment than for the short MISMIP experiment, also f_{SSA} shows more variation. However, when the solution is close to steady state, the contact force is around -15 m MPa and it never exceeds this value during the experiment. Therefore, convergence of the coupled system can be accelerated by initializing $f_{SSA} = -15$ m MPa instead of 0 m MPa. This was tested for the fasted configuration C3. Indeed, the number of FS iterations necessary decreased to 10677 and

the total computation time to 43776 cpu s.

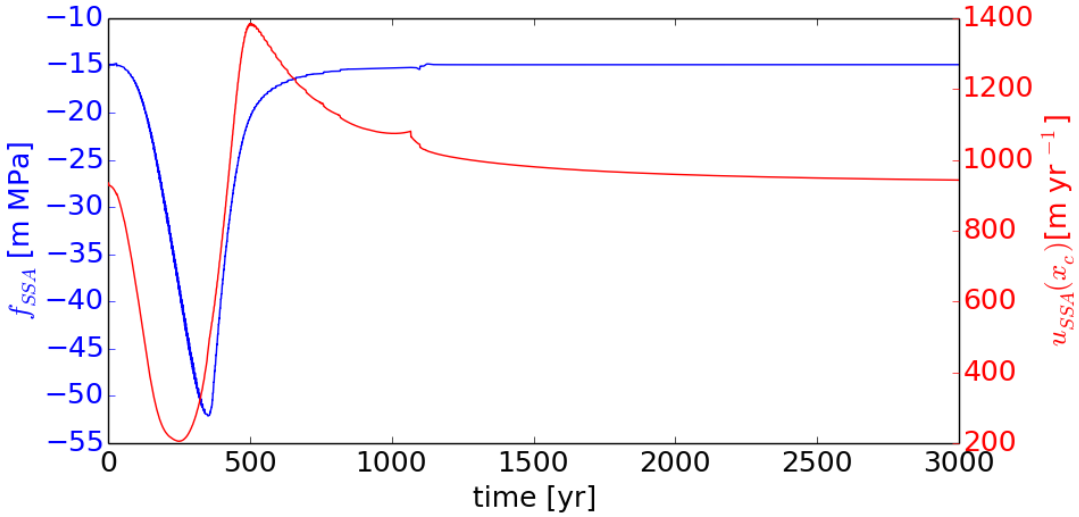

Figure 34: Time evolution of f_{SSA} and $u_{SSA}(x_c)$. The bump at t=1101 yr can be explained by a sudden grounding line retreat hence change of coupling location x_c, where the velocity u_{SSA} and thereby force f_{SSA} is different.

5.3.3 Three dimensional ice shelf ramp

The discontinuity in the grounding line only allows for direct solution of the linearized system of FS equations, which requires too much memory to solve for a three dimensional marine ice sheet problem, such that it needs to be solved in parallel. However, computation time of solving the flow equations in parallel is determined by the computation time of the slowest part of the partitioned model domain. Therefore, balancing the load would become a challenge now the domain has already been decomposed into one FS and one SSA part, which is outside of the scope of this project. Consequently, the set up for a three dimensional experiment is limited to a shelf only case. The coupling interface is defined halfway again, $\mathbf{x}_c := \{\mathbf{x} \in \Omega, x = 100 \text{ km}\}$, the resulting horizontal velocity u_c is shown in Figure 35.

3D ice shelf ramp - Accuracy In the left half, Ω_{FS}, the coupled model gives that ice flow accelerates to 4787 m yr^{-1} whereas $u_{FS} = 4735$ m yr^{-1} in the FS model. Hence the buttressing provided by the right half, Ω_{SSA}, is modeled very accurately by the coupling with a relative difference of about 1%. However, since Section 5.2.2 showed that the models give different flow solutions, this difference increases to 1.4% at the calving front (see Figure 36) which is of the same order of magnitude as the difference between SSA and FS.

3D ice shelf ramp - Efficiency The mean assembly time per execution of the FlowSolver is 33 s, slightly higher than the uncoupled model. However, opposed to the two dimensional experiments, solution time now dominates assembly time. The mean solution time per execution of the FlowSolver decreased from 117 s to 53 s. When taking a convergence tolerance of 10^{-4} for the coupled model (equal to the individual models' convergence tolerance in the comparison section) and a non-linear convergence tolerance of 10^{-3} for the FlowSolver before continuing to a next coupling iteration, a total of 30 non-linear FS iterations was necessary compared to 27 in the uncoupled FS model. The total cpu time spent on solving the horizontal SSA velocities and afterwards coupling to the FS velocities is 114 s. Hence the total solver time decreased from 4005 to 2707 s, despite the increase in assembly time and number of FS iterations. The total number of non-linear FS iterations in the coupled model could be decreased by limiting the number of non-linear FS iterations before continuing to the next coupled iteration, but since it is already close to the number of iterations in the original model this will not lead to significant increase in efficiency.

The coupled model did not converge in experiments with a coupling interface that is not aligned with the y-axis, but instead has a step of a few grid points (see Figure 37). The three dimensional coupled model is therefore currently limited to a semi two dimensional set up since the grounding line should then also (approximately) be aligned with the y-axis in order to be able to define a coupling interface aligned with the y-axis.

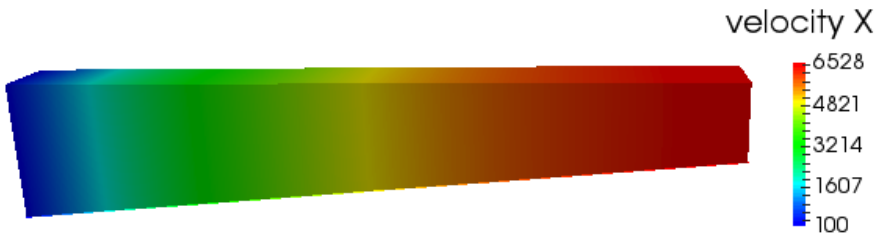

Figure 35: Horizontal velocity u [m yr^{-1}] from coupled model solved for the three dimensional ice shelf ramp.

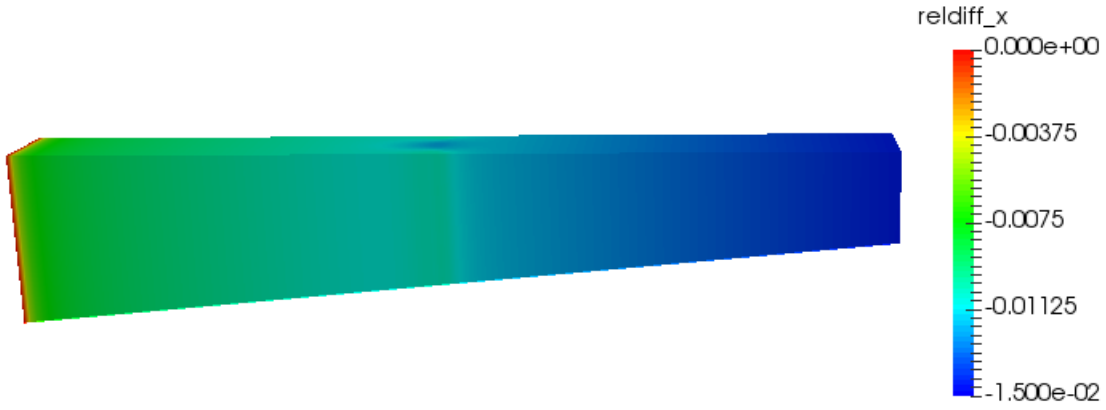

Figure 36: Relative difference $(u_{FS} - u_c)/u_{FS}$.

However, the divergent behavior of the coupled model could be caused by the normal of the coupling interface, which is not well defined at the edges of the step. For realistic data, the two dimensional foot print that yields the three dimensional mesh usually consists of triangles. This will yield a smoother coupling interface which may allow the coupled model to converge.

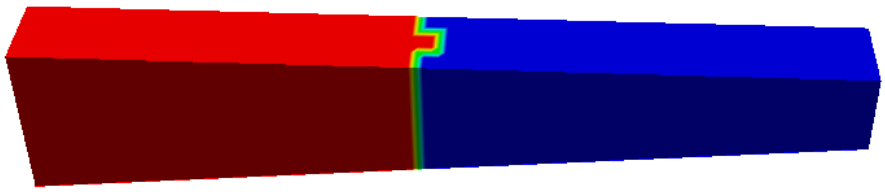

Figure 37: Domain composition with $\mathbf{x}_c$ not aligned with y-axis, Ω_{FS} shown in red, Ω_{SSA} in blue, the coupling interface $\mathbf{x}_c$ in green.

6 Conclusion and discussion

In this project, the aim was to extend the ISCAL method with the SSA. However, as shown in Section 5.1, limitations to ISCAL's robustness are caused by instabilities in the FS solution. Therefore, the grounding line experiments for the coupling with SSA were restricted to cases where the FS model in Elmer/Ice has been proven stable over a longer period of time. For these specific cases, rapid sliding on the grounded part is assumed, such that SIA is not applicable. Therefore a SSA-FS coupling was tested, but the coupling is implemented such that the FS solver could easily be exchanged with ISCAL in case SIA is applicable for (part of) the grounded part of the ice sheet. More practical details on the implementation and code availability is given in Section A. The three research questions are repeated here, together with the findings.

1. Is the ISCAL method as described in Ahlkrona et al. [2016] accurate for ice sheet modeling?

When investigating ISCAL's robustness, stabilization methods currently available in Elmer/Ice showed to be incapable of damping numerical oscillations in the FS solution for geometries similar to the ones in Ahlkrona et al. [2016]. Oscillations appear in the vertical velocity first, which could explain why such oscillations are not a well-known problem for Elmer/Ice. When only regarding the magnitude of the ice velocity $||\mathbf{u}|| = \sqrt{u^2 + v^2 + w^2}$, the oscillations go unnoticed since the magnitude of the vertical velocity is of at least one order lower than horizontal velocities. Besides that, Elmer/Ice is originally developed for modeling glacier flow (which does not require as high aspect ratio elements). For example the Gorshkov crater glacier modeled in Zwinger et al. [2007] has an aspect ratio $[H]/[L] \approx 1/3$, compared a typical value of $[H]/[L] \approx 10^{-3}$ for ice sheets. This may explain why stabilization was not as problematic for previous Elmer/Ice experiments. When applying Elmer/Ice to Greenland, Seddik et al. [2012] do state that vertical resolution could not be increased due to stability problems, showing that elongated elements indeed seem to be a challenge when modeling an ice sheet with the FS model of Elmer/Ice. Since stabilizing the FS equations is outside the scope of this project, ISCAL's robustness was not investigated further after finding that oscillations in the FS solution are limiting ISCAL's capability of modeling a conceptual three dimensional ice sheet on longer time scales.

2. In what way can the SSA and FS equations be coupled?

Before coupling FS and SSA, the two models have been compared for a floating ice shelf ramp. Resulting velocities in the two dimensional case are almost identical, in three dimensions the models differ more but still the velocity difference is below 1.5%. In both cases, the SSA model is much faster than the FS model despite the small differences in solution, which motivates coupling of the two. The vertical velocity in the SSA model

cannot be solved with the buoyancy force as a boundary condition as done for the FS model. Therefore, the surface evolution cannot be computed from the free surface equations as is done for the FS model, since the shelf would not remain afloat if buoyancy is not taken into account. In order to ensure that the shelf remains afloat, the surface evolution is instead computed by the thickness equation that only relies on the horizontal SSA velocities. The surface elevation in Ω_{SSA} is then calculated from the thickness and floatation criterion, which allows SSA and FS to be coupled in transient simulations.

A main achievement of this project is the implementation of a novel iterative SSA-FS coupling. At the coupling interface, the FS velocity is applied as inflow boundary condition for SSA. Together with the cryostatic pressure, a depth averaged contact force (resulting from the SSA velocity) is applied as a boundary condition for FS. This two-way coupling converges to a velocity that is very similar to the FS model in the first test on a conceptual ice shelf ramp. For the two dimensional ramp, the maximum relative error in the coupled velocity is 0.3%. The coupled velocity in the three dimensional case shows a difference up to 1.4% with respect to the FS solution. This higher error can be explained by the difference between SSA and FS for the three dimensional ramp, which is of the same order.

3. How accurate and efficient is the SSA-FS coupling for grounding line problems?

The SSA-FS coupling has been applied to two conceptual two dimensional marine ice sheets. The coupled model shows to be very accurate for diagnostic runs with a relative difference in velocity compared to FS below 0.5% when starting to use SSA at 30 km seaward from the grounding line. Therefore, the difference with a reference FS solution computed for the same geometry as the coupled solution, will also be very small in subsequent time steps. Using the difference with the reference solution as coupling criterion will thus not change the initial domain division upon grounding line distance, unless the tolerances would be very small. Besides that, the gradient of the horizontal velocity over the vertical depends on the chosen grounding line problem. For Budd's MIS, basal drag is so low that even at the grounding line the horizontal velocity is constant over the vertical. Using the vertical gradient of the horizontal reference velocity would then also not change the initial domain devision. Therefore, it was chosen here to only apply the distance to the grounding line as coupling criterion.

For both MIS problems, the coupled model performs very accurately during a transient simulation. Both the maximum relative difference in MISMIP after 5 years and Budd's MIS after 3000 years are below 2%. However, the velocity difference for Budd's MIS is higher (5.3%) in the more dynamic part of the simulation when the grounding line is retreating.

Also efficiency was examined for both MIS problems. The current implementation in

Elmer/Ice does not allow for as much speed up as expected when comparing computation times of the FS and SSA models when applied separately to the ice shelf ramp. This is due to the inefficient assembly, the time it takes to assembly A_{FS} for Ω_{FS} in the coupled model takes as long as the assembly for Ω in the FS only model. This is problematic since the assembly time dominates the total solution time.

The potential speed up, assuming that assembly would be implemented efficiently, depends both on the proportion of nodes in Ω_{FS} and the total number of FS iterations inside the coupled model compared to the FS only model. The latter can be minimized by setting a maximum iteration number to the non-linear FS solver within the coupled model. When performing only one FS iteration per coupled iteration, the number of FS iterations in the coupling is similar or even lower than for the FS only model. However, this comes at the cost of launching the FS solver more frequently, which takes an significant amount of time for these simplified two dimensional problems but will be relatively small in large scale three dimensional experiments.

A rough estimate of the potential speed up can be done, assuming that the assembly can be implemented efficiently such that the computation time needed to calculate $\mathbf{u}_{FS}$ in Ω_{FS} from the linearized system only depends on the number of nodes in Ω_{FS}. In Gagliardini and Zwinger [2008], cpu time of the FS model is reported to be proportional to $(3N)^{1.27}$ for two dimensional applications, where N is the number of nodes in the discretization. With respectively 79% and 42% of the nodes in Ω_{FS} for MISMIP and Budd's MIS, the computation time of the FS solver reduce to respectively 26% and 67% compared to solving FS on the entire domain. This is a very rough estimate, since Gagliardini and Zwinger [2008] state that their results indicate that cpu time consumption depends on the geometry as well, not only on the mesh density, so the power 1.27 is different for the geometries here. Besides that, solution time for Ω_{SSA} adds to the total cpu time for the coupled model, even though the FS model dominates computation time.

Convergence speed of the iteration to couple the models can be further increased by optimizing the initial guess. Therefore, it is important to re-use as much information as possible form the previous time step when initializing the coupled model. Currently, when the domain division changes, the previous solution for respectively $\mathbf{u}_{FS}(t_{i-1}), \mathbf{u}_{SSA}(t_{i-1})$ is used for initializing the Picard iteration solving the respective models. However, this implies that if for example the FS domain gets bigger, $\mathbf{u}_{FS} = 0$ is used as initial value for the nodes in $\Omega_{FS}(t_i) \backslash \Omega_{FS}(t_{i-1})$. A more efficient implementation would initialize with the coupled velocity $\mathbf{u}_c(t_{i-1})$ (hence $\mathbf{u}_{FS}(t_{i-1})$ in $\Omega_{FS}(t_{i-1})$ and $\mathbf{u}_{SSA}(t_{i-1})$ in $\Omega_{SSA}(t_{i-1})$). The same holds for initialization of the contact force f_{SSA}, as was shown in the prognostic experiments to be improve convergence speed when using a nonzero initial value. Further computational gain could be made by exchanging the FS solver by ISCAL, combining all three approximation levels SIA, SSA and FS if the experiment set up is such that regions

with higher basal drag are present in the grounded part of the MIS where SIA is applicable. Coupling approximation levels for modeling ice flow shows to be promisingly accurate, but the technical implementation of both ISCAL and the FS - SSA coupling should be reconsidered for efficiency. More efficient and stable methods than currently available in Elmer/Ice are required to model a full ice sheet - shelf system from formation to decay in order to validate the ice sheet model against geological data.

7 Outlook

The main problems encountered so far, are caused by limitations of the FS model in Elmer/Ice. Throughout the entire project, Elmer's FlowSolver is used for computing $\mathbf{u}_{FS}$. The incomplete LU preconditioning as used in the FlowSolver, is not ideal for the FS equations. This may explain why iterative solvers do not converge for the grounding line problems, employing a discontinuous sliding law at the grounding line. The need of solving the linearized system with a direct method causes serious problems when continuing to three dimensional domains. Not only because the computational cost in three dimensions grows with the square of the number of unknowns, also the memory usage becomes excessive for large three dimensional applications [Råback et al., 2016b]. Elmer does contain another solver called ParStokes, described in Section 22 of Råback et al. [2016a], that applies a preconditioning specific for the steady state Navier-Stokes equations based on the idea of block preconditioning. ParStokes solves the linearized system more efficiently and will therefore be more suitable for large scale modeling as required for complete ice sheets. Unpopularity of ParStokes in the numerical glaciology community could be explained by limited support, none of the latest Elmer/Ice courses discussed ParStokes.

Another weakness of solving the FS equations in Elmer/Ice is shown by the oscillations in the vertical velocity as shown in Section 5.1. This calls for a stabilization method designed for elements with a small aspect ratio, for example by using a different order for the velocity space than the pressure space, as suggested by Ainsworth and Coggins [2000] and Isaac et al. [2015]. Anisotropic stabilization techniques, for example as presented in Blasco [2008], may overcome stability issues due to high aspect ratios and are therefore suggested to be investigated in further research.

The original implementation of ISCAL is inside a copy of the FlowSolver, so it will need to be implemented over again to let ParStokes solve the FS velocities instead. Besides that, only linear sliding is implemented in ISCAL such that ISCAL needs to be extended before it can be applied to the grounded part of the MISMIP experiment. Therefore, the original ISCAL method described in Ahlkrona et al. [2016] was not further investigated here. The coupling of FS and SSA as implemented here does not rely on the specific solver used to compute $\mathbf{u}_{FS}$, in fact it could use any solver to calculate the velocity in Ω_{FS}. The coupling defines elements active and passive (see Råback et al. [2016b]) for the respective FS and SSA solvers. However, it was shown here that this is very inefficient since the assembly time for the FS equations hardly changes, regardless of being passive on a substantial part of the domain. This was not the case for ISCAL, where SIA is added inside the FlowSolver. Therefore, also the coupling to SSA should be implemented on a lower level, inside a FS solver instead of relying on passive elements. It is suggested for future studies to implement the coupling to both SIA and SSA as an extension to the ParStokes solver instead of the FlowSolver.

Both efficiency and accuracy of the coupled model cannot get better than efficiency and accuracy of the FS model around the grounding line. Especially when the FS model requires a high resolution near the grounding line in order to ensure convergence (as the MISMIP experiment showed), the possible speed-up of the coupled model will be limited since the most expensive FS model needs to be applied in the refined area. Therefore, future studies could include sub grid parametrization of the grounding line and investigate alternative sliding laws that may decrease mesh resolution dependence such as Budd's sliding law.

A Code availability

Elmer is available at `https://github.com/ElmerCSC/` and can be redistributed and/or modified under the terms of the GNU General Public License as published by the Free Software Foundation; either version 2 of the License, or (at your option) any later version. The same holds for the code of ISCAL and the SSA-FS coupling, which are described in more detail in the next sections.

A.1 ISCAL

The ISCAL method has its own branch on github, called elmerice-iscal, available at `https://github.com/ElmerCSC/elmerfem/tree/elmerice-iscal`, including both the code and a test case with the Vialov profile. Besides that, documentation is provided at `http://elmerice.elmerfem.org/wiki/doku.php?id=solvers:iscal`.

A.2 FS and SSA coupling

The solver for the SSAmask (setting values 1 in Ω_{FS}, 0 at the coupling interface and -1 for Ω_{SSA}) and computation of the weights for the contact force in the three dimensional case is freely available at `https://github.com/ElmerCSC/elmerfem/blob/elmerice/elmerice/Solvers/SSAmask.F90`. The solver SSAmask.F90 is inspired on GroundedSolver.F90, computing the grounded mask. The subroutine SSAWeights in SSAmask.F90 is written by Thomas Zwinger, tested and debugged by Eef van Dongen. The option of glueing the FS and SSA solution together is added as a functionality to the original SSASolver with the keyword `SSA Coupling = Logical True`, freely available at `https://github.com/ElmerCSC/elmerfem/blob/elmerice/elmerice/Solvers/SSASolver.F90`[13]. More implementation is inside the sif (solver input file), where passive and active elements, boundary conditions and surface evolution for Ω_{FS} and Ω_{SSA} are defined. More documentation on the use will be added to the Elmer/Ice wiki `http://elmerice.elmerfem.org/wiki/doku.php?id=solvers:ssa`. Besides that, model C4 from MISMIP prognostic will be added as an example to `https://github.com/ElmerCSC/elmerfem/tree/elmerice/elmerice/examples`, available under the same terms. It should be noted that the sif contains many MATC functions[14], which are in general time consuming. For optimizing computation time, it is recommended to exchange MATC functions with user functions written in F90. However, in order to limit the number of separate functions necessary to run the coupled model it was chosen to implement as much as possible within the sif. For comparison, the computation times of the FS model reported here are resulting from running the same sif as the coupled model, but defining $\Omega_{FS} := \Omega, \Omega_{SSA} := \varnothing$.

[13] For the specific commit that shows differences with the original SSASolver, see `https://github.com/ElmerCSC/elmerfem/commit/633e0bba0b003c384d5034c4af3706e757b4606f`

[14] MATC is Elmer's internal scripting language, a manual is available at `ftp://ftp.funet.fi/index/elmer/doc/MATCManual.pdf`.

References

J. Ahlkrona, N. Kirchner, and P. Lötstedt. A numerical study of scaling relations for non-newtonian thin-film flows with applications in ice sheet modelling. *The Quarterly Journal of Mechanics and Applied Mathematics*, 66(4):417–435, 2013a.

J. Ahlkrona, N. Kirchner, and P. Lötstedt. Accuracy of the zeroth-and second-order shallow-ice approximation–numerical and theoretical results. *Geoscientific Model Development*, 6(6):2135–2152, 2013b.

J. Ahlkrona, P. Lötstedt, N. Kirchner, and T. Zwinger. Dynamically coupling the non-linear Stokes equations with the shallow ice approximation in glaciology: Description and first applications of the ISCAL method. *Journal of Computational Physics*, 308: 1–19, 2016.

M. Ainsworth and P. Coggins. The stability of mixed hp-finite element methods for Stokes flow on high aspect ratio elements. *SIAM Journal on Numerical Analysis*, 38(5):1721–1761, 2000.

S. Anandakrishnan, G. A. Catania, R. B. Alley, and H. J. Horgan. Discovery of till deposition at the grounding line of whillans ice stream. *Science*, 315(5820):1835–1838, 2007.

D. N. Arnold, F. Brezzi, and M. Fortin. A stable finite element for the Stokes equations. *Calcolo*, 21(4):337–344, 1984.

M. Bercovier and O. Pironneau. Error estimates for finite element method solution of the Stokes problem in the primitive variables. *Numerische Mathematik*, 33(2):211–224, 1979.

J. Bernales, I. Rogozhina, R. Greve, and M. Thomas. Comparison of hybrid schemes for the combination of shallow approximations in numerical simulations of the Antarctic Ice Sheet. *The Cryosphere*, 11(1):247–265, 2017.

J. Blasco. An anisotropic gls-stabilized finite element method for incompressible flow problems. *Computer Methods in Applied Mechanics and Engineering*, 197(45):3712–3723, 2008.

H. Blatter, R. Greve, and A. Abe-Ouchi. Present state and prospects of ice sheet and glacier modelling. *Surveys in Geophysics*, 32(4-5):555–583, 2011.

W. Budd, P. Keage, and N. Blundy. Empirical studies of ice sliding. *Journal of Glaciology*, 23(89):157–170, 1979.

W. Budd, D. Jenssen, and I. Smith. A three-dimensional time-dependent model of the West Antarctic Ice Sheet. *Annals of Glaciology*, 5(1):29–36, 1984.

G. Cheng, P. Lötstedt, and L. von Sydow. Accurate and stable time stepping in ice sheet modeling. *Journal of Computational Physics*, 329:29–47, 2017.

C. Ó. Cofaigh, J. A. Dowdeswell, J. Evans, and R. D. Larter. Geological constraints on Antarctic palaeo-ice-stream retreat. *Earth Surface Processes and Landforms*, 33(4): 513–525, 2008.

R. Courant and D. Hilbert. Methods of mathematical physics vol. i. translated and revised from the german original. first english ed. 1953.

H. B. Dhia. Problémes mécaniques multi-échelles: la méthode arlequin. *Comptes Rendus de l'Académie des Sciences-Series IIB-Mechanics-Physics-Astronomy*, 326(12):899–904, 1998.

T. Dupont and R. Alley. Assessment of the importance of ice-shelf buttressing to ice-sheet flow. *Geophysical Research Letters*, 32(4), 2005.

G. Durand, O. Gagliardini, B. De Fleurian, T. Zwinger, and E. Le Meur. Marine ice sheet dynamics: Hysteresis and neutral equilibrium. *Journal of Geophysical Research: Earth Surface*, 114(F3), 2009a.

G. Durand, O. Gagliardini, T. Zwinger, E. Le Meur, and R. C. Hindmarsh. Full Stokes modeling of marine ice sheets: influence of the grid size. *Annals of Glaciology*, 50(52): 109–114, 2009b.

L. Favier, O. Gagliardini, G. Durand, and T. Zwinger. A three-dimensional full Stokes model of the grounding line dynamics: effect of a pinning point beneath the ice shelf. *The Cryosphere*, 6:101–112, 2012.

J. Feldmann, T. Albrecht, C. Khroulev, F. Pattyn, and A. Levermann. Resolution-dependent performance of grounding line motion in a shallow model compared with a full-Stokes model according to the MISMIP3d intercomparison. *Journal of Glaciology*, 60(220):353–360, 2014.

L. P. Franca and S. L. Frey. Stabilized finite element methods: II. the incompressible Navier-Stokes equations. *Computer Methods in Applied Mechanics and Engineering*, 99 (2-3):209–233, 1992.

O. Gagliardini and T. Zwinger. The ISMIP-HOM benchmark experiments performed using the Finite-Element code Elmer. *The Cryosphere Discussions*, 2(1):75–109, 2008.

O. Gagliardini, T. Zwinger, F. Gillet-Chaulet, G. Durand, L. Favier, B. De Fleurian, R. Greve, M. Malinen, C. Martín, P. Råback, et al. Capabilities and performance of Elmer/Ice, a new-generation ice sheet model. *Geoscientific Model Development*, 6(4): 1299–1318, 2013.

O. Gagliardini, J. Brondex, F. Gillet-Chaulet, L. Tavard, V. Peyaud, and G. Durand. Impact of mesh resolution for MISMIP and MISMIP3d experiments using Elmer/Ice. *The Cryosphere*, 10(1):307–312, 2016.

F. Gillet-Chaulet, O. Gagliardini, H. Seddik, M. Nodet, G. Durand, C. Ritz, T. Zwinger, R. Greve, and D. G. Vaughan. Greenland Ice Sheet contribution to sea-level rise from a new-generation ice-sheet model. *The Cryosphere*, 6(6):1561–1576, 2012.

R. Gladstone, A. Payne, and S. Cornford. Parameterising the grounding line in flow-line ice sheet models. *The Cryosphere*, 4(4):605, 2010.

R. M. Gladstone, A. J. Payne, and S. L. Cornford. Resolution requirements for grounding-line modelling: sensitivity to basal drag and ice-shelf buttressing. *Annals of Glaciology*, 53(60):97–105, 2012.

R. M. Gladstone, R. C. Warner, B. K. Galton-Fenzi, O. Gagliardini, T. Zwinger, and R. Greve. Marine ice sheet model performance depends on basal sliding physics and sub-shelf melting. *The Cryosphere*, 11:319–329, 2017.

R. Greve and H. Blatter. *Dynamics of ice sheets and glaciers*. Springer Science & Business Media, 2009.

G. Gudmundsson, J. Krug, G. Durand, L. Favier, and O. Gagliardini. The stability of grounding lines on retrograde slopes. *The Cryosphere*, 6:1497–1505, 2012.

C. Helanow and J. Ahlkrona. Galerkin least-squares stabilization in Ice Sheet modeling-accuracy, robustness, and comparison to other techniques. *arXiv preprint arXiv:1702.08369*, 2017.

R. C. Hindmarsh. Qualitative dynamics of marine ice sheets. In *Ice in the climate system*, pages 67–99. Springer, 1993.

R. C. Hindmarsh. Notes on basic glaciological computational methods and algorithms. In *Continuum Mechanics and Applications in Geophysics and the Environment*, pages 222–249. Springer, 2001.

T. J. Hughes and L. P. Franca. A new finite element formulation for computational fluid dynamics: VII. the Stokes problem with various well-posed boundary conditions: symmetric formulations that converge for all velocity/pressure spaces. *Computer Methods in Applied Mechanics and Engineering*, 65(1):85–96, 1987.

K. Hutter. Dynamics of glaciers and large ice masses. *Annual Review of Fluid Mechanics*, 14(1):87–130, 1982.

K. Hutter. *Theoretical glaciology: material science of ice and the mechanics of glaciers and ice sheets*, volume 1. Springer, 1983.

P. Huybrechts and T. Payne. The EISMINT benchmarks for testing ice-sheet models. *Annals of Glaciology*, 23(1):1–12, 1996.

Ó. Ingólfsson and J. Y. Landvik. The Svalbard-Barents Sea Ice-Sheet–Historical, current and future perspectives. *Quaternary Science Reviews*, 64:33–60, 2013.

T. Isaac, G. Stadler, and O. Ghattas. Solution of nonlinear Stokes equations discretized by high-order finite elements on nonconforming and anisotropic meshes, with application to ice sheet dynamics. *SIAM Journal on Scientific Computing*, 37(6):B804–B833, 2015.

I. Joughin and R. B. Alley. Stability of the West Antarctic Ice Sheet in a warming world. *Nature Geoscience*, 4(8):506–513, 2011.

G. Jouvet. Mechanical error estimators for shallow ice flow models. *Journal of Fluid Mechanics*, 807:40–61, 2016.

G. Jouvet and J. Rappaz. Analysis and finite element approximation of a nonlinear stationary Stokes problem arising in glaciology. *Advances in Numerical Analysis*, 2011, 2012.

N. Kirchner, K. Hutter, M. Jakobsson, and R. Gyllencreutz. Capabilities and limitations of numerical Ice Sheet models: a discussion for earth-scientists and modelers. *Quaternary Science Reviews*, 30(25):3691–3704, 2011.

N. Kirchner, J. Ahlkrona, E. J. Gowan, P. Lötstedt, J. M. Lea, R. Noormets, L. von Sydow, J. A. Dowdeswell, and T. Benham. Shallow ice approximation, second order shallow ice approximation, and full Stokes models: A discussion of their roles in palaeo-ice sheet modelling and development. *Quaternary Science Reviews*, 135:103–114, 2016.

O. A. Ladyzhenskaya and R. A. Silverman. *The mathematical theory of viscous incompressible flow*, volume 76. Gordon and Breach New York, 1969.

E. Le Meur, O. Gagliardini, T. Zwinger, and J. Ruokolainen. Glacier flow modelling: a comparison of the shallow ice approximation and the full-Stokes solution. *Comptes Rendus Physique*, 5(7):709–722, 2004.

L. Lliboutry. General theory of subglacial cavitation and sliding of temperate glaciers. *Journal of Glaciology*, 7(49):21–58, 1968.

M. B. Lythe and D. G. Vaughan. Bedmap: A new ice thickness and subglacial topographic model of Antarctica. *Journal of Geophysical Research: Solid Earth*, 106(B6):11335–11351, 2001.

D. R. MacAyeal. Large-scale ice flow over a viscous basal sediment: Theory and application to ice stream b, Antarctica. *Journal of Geophysical Research: Solid Earth*, 94(B4):4071–4087, 1989.

L. Morland. Unconfined ice-shelf flow. In *Dynamics of the West Antarctic Ice Sheet*, pages 99–116. Springer, 1987.

W. Paterson. The physics of glaciers, 480 pp, 1994.

F. Pattyn, A. Huyghe, S. De Brabander, and B. De Smedt. Role of transition zones in marine ice sheet dynamics. *Journal of Geophysical Research: Earth Surface*, 111(F2), 2006.

F. Pattyn, L. Perichon, A. Aschwanden, B. Breuer, B. De Smedt, O. Gagliardini, G. H. Gudmundsson, R. Hindmarsh, A. Hubbard, J. V. Johnson, et al. Benchmark experiments for higher-order and full Stokes Ice Sheet models (ISMIP-HOM). *The Cryosphere Discussions*, 2(1):111–151, 2008.

F. Pattyn, C. Schoof, L. Perichon, R. Hindmarsh, E. Bueler, B. d. Fleurian, G. Durand, O. Gagliardini, R. Gladstone, D. Goldberg, et al. Results of the marine ice sheet model intercomparison project, MISMIP. *The Cryosphere*, 6(3):573–588, 2012.

F. Pattyn, L. Perichon, G. Durand, L. Favier, O. Gagliardini, R. C. Hindmarsh, T. Zwinger, T. Albrecht, S. Cornford, D. Docquier, et al. Grounding-line migration in plan-view marine ice-sheet models: results of the ice2sea MISMIP3d intercomparison. *Journal of Glaciology*, 59(215):410–422, 2013.

D. Pollard and R. M. DeConto. Modelling West Antarctic Ice Sheet growth and collapse through the past five million years. *Nature*, 458(7236):329–332, 2009.

C. Raymond. Shear margins in glaciers and ice sheets. *Journal of Glaciology*, 42(140): 90–102, 1996.

E. Rignot, J. Mouginot, and B. Scheuchl. Ice flow of the Antarctic Ice Sheet. *Science*, 333 (6048):1427–1430, 2011.

P. Råback, M. Malinen, J. Ruokolainen, A. Pursula, and T. Zwinger. *Elmer Models Manual*, 2016a.

P. Råback, M. Malinen, J. Ruokolainen, A. Pursula, and T. Zwinger. *Elmer Solver Manual*, 2016b.

M. Schäfer, T. Zwinger, P. Christoffersen, F. Gillet-Chaulet, K. Laakso, R. Pettersson, V. A. Pohjola, T. Strozzi, and J. C. Moore. Sensitivity of basal conditions in an inverse model: Vestfonna ice cap, nordaustlandet/svalbard. *The Cryosphere*, 6:771–783, 2013.

C. Schoof. On the mechanics of ice-stream shear margins. *Journal of Glaciology*, 50(169): 208–218, 2004.

C. Schoof. Ice sheet grounding line dynamics: Steady states, stability, and hysteresis. *Journal of Geophysical Research: Earth Surface*, 112(F3), 2007.

C. Schoof and I. Hewitt. Ice-sheet dynamics. *Annual Review of Fluid Mechanics*, 45: 217–239, 2013.

C. Schoof and R. C. Hindmarsh. Thin-film flows with wall slip: an asymptotic analysis of higher order glacier flow models. *The Quarterly Journal of Mechanics and Applied Mathematics*, page hbp025, 2010.

H. Seddik, R. Greve, T. Zwinger, F. Gillet-Chaulet, and O. Gagliardini. Simulations of the Greenland Ice Sheet 100 years into the future with the full Stokes model Elmer/Ice. *Journal of Glaciology*, 58(209):427–440, 2012.

H. Seroussi, H. Ben Dhia, M. Morlighem, E. Larour, E. Rignot, and D. Aubry. Coupling ice flow models of varying orders of complexity with the tiling method. *Journal of Glaciology*, 58(210):776–786, 2012.

T. Stocker, D. Qin, G. Plattner, M. Tignor, S. Allen, J. Boschung, A. Nauels, Y. Xia, V. Bex, and P. Midgley. Ipcc, 2013: summary for policymakers in climate change, 2013.

R. H. Thomas and C. R. Bentley. A model for holocene retreat of the West Antarctic Ice Sheet. *Quaternary Research*, 10(2):150–170, 1978.

A. Vieli and A. Payne. Assessing the ability of numerical ice sheet models to simulate grounding line migration. *Journal of Geophysical Research: Earth Surface*, 110(F1), 2005.

J. Weertman. On the sliding of glaciers. *Journal of Glaciology*, 3(21):33–38, 1957.

J. Weertman. Stability of the junction of an ice sheet and an ice shelf. *Journal of Glaciology*, 13(67):3–11, 1974.

M. Weis. *Theory and finite element analysis of shallow ice shelves.* PhD thesis, TU Darmstadt, 2001.

A. Wilchinsky and V. Chugunov. Modelling ice flow in various glacier zones. *Journal of Applied Mathematics and Mechanics*, 65(3):479–493, 2001.

T. Zwinger, R. Greve, O. Gagliardini, T. Shiraiwa, and M. Lyly. A full Stokes-flow thermo-mechanical model for firn and ice applied to the gorshkov crater glacier, kamchatka. *Annals of Glaciology*, 45(1):29–37, 2007.